Si based nanostructures for solar cells

Si based nanostructures for solar cells

PhD THESIS

Dottorato di Ricerca in Scienza dei Materiali - XXIII Ciclo
UNIVERSITA' DEGLI STUDI DI CATANIA

Cristina Annamaria Garozzo

University of Catania

Consiglio Nazionale delle Ricerche

Tutor: Prof. Emanuele Rimini

Supervisor: Dr.ssa Rosaria Puglisi

Supervisor: Dott. Salvatore Lombardo

PhD Coordinator: Prof. A Licciardello

Keywords: nanodot, nanowire, self-assembling,solar cell.

Copyright© 2010 by Cristina Garozzo

All rights reserved. No part of the material protected by this copyright notice may be reproduced or utilized in any form or by any means, electronic or mechanical, including photocopying, recording or by any information storage and retrieval system, without permission from the author.

Contents

Introduction **1**
0.1 General overview 1
0.2 Thesis outline 5

References **6**

1 aSi:H Thin Film solar cells **9**
1.1 Introduction 9
1.2 Semiconductor Solar cells. 10
  1.2.1 Solar Cell I –V Characteristics 11
  1.2.2 Air Mass 13
1.3 Hydrogenated amorphous silicon 14
  1.3.1 PECVD 14
  1.3.2 Characteristics of a-Si:H 16
  1.3.3 Staebler–Wronski 19
  1.3.4 Electronic Density-of-states 20
  1.3.5 Absorption coefficient 22
1.4 Pin structure 23
  1.4.1 Substrate and superstrate 24
  1.4.2 Multiple-Junction solar cells 25
1.5 Results and discussion 25
  1.5.1 Absorption coefficient 28
  1.5.2 Cell design 29
  1.5.3 Pin diode measures 33
    1.5.3.1 IV characteristic 33
  1.5.4 Nc-Si:H solar cell: electrical characterization 35
1.6 Conclusions 37

References **39**

2 Hydrogen role in the phase transition from amorphous to nanocrystalline silicon films 41
- 2.1 Introduction 41
- 2.2 Deposition characteristics (Experimental) 42
- 2.3 Results and discussion 43
  - 2.3.1 Variation in deposition rate 43
  - 2.3.2 Tem Analysis 45
  - 2.3.3 Pair distribution function 45
    - 2.3.3.1 Data collection and Results. 47
  - 2.3.4 Hydrogen content: Elastic Recoil Detection Analysis 50
  - 2.3.5 H role in the transition 51
  - 2.3.6 The Hydrogen bonding structure: FTIR Analysis 53
  - 2.3.7 Dot Size correlation with hydrogen dilution 59
- 2.4 Conclusion 61

References 62

3 3rd generation solar cells: Ordered templates for nanowire synthesis 67
- 3.1 Introduction 67
- 3.2 Experimental 69
- 3.3 Results and discussion 70
- 3.4 Conclusions 86

References 87

Summary 91

Curriculum Vitae 93

List of publications 95

Acknowledgements 97

List of Figures

1.1 A schematic of a simple conventional solar cell. Creation of electron–hole pairs, blue circle and red circle, respectively, is depicted . 11

1.2 Simple solar cell circuit model. Diode 1 represents the recombination current in the quasi-neutral regions ($\propto e^{qV/kT}$), while diode 2 represents recombination in the depletion region ($\propto e^{qV/2kT}$)(b)[7] 12

1.3 Schematic of a typical RF glow discharge deposition chamber[15] . 15

1.4 Computer model of the chemical bonding of hydrogenated amorphous silicon. The larger, gray spheres indicate Si atoms; the smaller, white spheres indicate hydrogen atoms, which are found in clustered and relatively isolated, dilute-phase configurations as indicated[7]. 17

1.5 Correlation of the defect (dangling bond) density in a-Si:H with the density of hydrogen removed from the material by heating (the hydrogen deficit). The data points are derived from deuterium and defect profiles by Jackson et al.[16] (350○C deuteration). The curve is a fit to a model proposed by Zafar and Schiff[17] 18

1.6 Configuration-coordinate diagram of the Staebler- Wronski DB creation reaction. Leftmost and rightmost wells are the stable and metastable states, respectively. Only two of many degenerate intermediate states with mobile H are represented by the central wells. Hydrogen diffusion (E_H) and metastability annealing (Ea) energies are indicated. [19] 19

1.7 Density of electronic states g(E) in hydrogenated amorphous silicon. The shaded areas indicate delocalized states in the bands; these bands themselves have tails of localized states with an exponential distribution. Midway between the bands are levels belonging to gross defects such as dangling Si bonds indicated by the two peaked bands aroundE_F[7] 21

1.8 Curves for the optical absorption coefficient α and the penetration depth dλ of monochromatic light with photon energy hν and wavelength λ, for wafer-type crystalline silicon (c-Si) and typical device-quality a-Si:H and mc-Si:H layers on glass.15,16 The curve for mc-Si:H has been corrected for light scattering due to surface roughness(16)[15] 23
1.9 pin photodiode, in which excess electrons are donated from the n-type p-type layers, leaving the charges and electric field illustrated.Each photon absorbed in the undoped, intrinsic layer generates an electron and a hole photocarrier. The electric field causes these carriers to drift in the directions shown 24
1.10 IV characteristic of n doped (a) p doped (b) and intrinsic (c) layer, at 300K (red line),470K(Magenta line),570K (green line), for the intrinsic layer it was not possible measure the IV characteristic at Temperature lower than 500 K(blue line). 26
1.11 Sheet resistance of n-doped (a), p-doped (b), and intrinsic amorphous layer as a function of temperature, measured with a constant heating rates (dT/dt) of 15 K/min. The inset shows the thickness of each layer. 27
1.12 Sheet resistance of n-doped (a-b-c) and p-doped (d-e-f) amorphous layer, measured with constant temperature reported of 300K (a, d), 470K (b, e) and 600K (c, f). The inset shows the thickness of each layer. 28
1.13 Curves for the optical absorption coefficient as a function of Energy, for p-doped (blue line), intrinsic (black line), and n-doped (green line) amorphous silicon layer. (courtesy of dott. Salvo Mirabella) 29
1.14 Simulations of the absorbed power of a PIN diode (a)with 1 um of absorber (intrinsic layer) and by varying the top contact thickness from 10 to 40 nm and (b) using a 20 nm of window layer thickness and by varying the absorber layer thickness The black curve shows the AM 1.5 G incident spectrum. 30
1.15 Simularion of the impact of D-centers on the PV cell performance. (Courtesy of Dott. Cannella). 32
1.16 The table reported the thickness of the analyzed diode. Schematic sketch of the realized p-i-n thin film solar cell. 34
1.17 Current voltage (a) and current density voltage (b-d) characteristics of several Pin diodes, analyzed in dark condition. The sample was made by varying the thickness of the absorber layer from 1 μm to 125 nm. The diameters of the analyzing diode are showed in the inset. 35
1.18 Courtesy Dott.ssa M. Foti (ST) 37

2.1 Figure 1. Variation of deposition rate as a function of hydrogen dilution of silane for a-Si:H and nc-Si:H films deposited by PE-CVD withF_{SiH4}=100 sccm (red) and F_{SiH4}==12 sccm(blue). 44

2.2 Plan view dark field TEM micrographs obtained by selecting the s[26]pot <111> for the hydrogenated Si layers deposited using F_{SiH4}=12 sccm and R=10(a) R=20(b) R30(c) R40(d). The films present a high density of nanocrystalline dots. 46

2.3 a) The scattered intensity I(q) (red line), for the sample deposited using FSiH4=12 sccm and R=10, the dashed line represent the background , calculated by fitting with a polynomial curve of II degree. The inset shows the diffraction pattern from which we collected I(q), (b) Calculated φ(q).The vertical lines indicate the range chosen for the calculation of G(r). 48

2.4 Pair distribution function, G(r), of the a-Si:H film for the several flow values R. The samples were made by using 100 sccm of silane flow (dashed line) with R=2 (black curve), R=10(red curve), and 12 sccm SiH_4 flow (continuous line) with R=10 (green curve), R=20 (magenta curve), R=30 (cyan curve) and R=40 (blue curve). The G(r) of a-Si:H evolves towards that of c-Si and begins to exhibit peaks that correspond to the higher crystalline coordination shells. The vertical lines indicate the peak positions in the g(r) of c-Si. . . 49

2.5 Hydrogen concentration for sample made by PECVD using different silane flow 100 sccm (black circle), and 12 sccm (black square) and different Hydrogen dilution(R). 51

2.6 Figure 6. Schematic representing the local structural rearrangements of Si atoms (blue spheres) before (a) and after(b) interaction with hydrogen atom (red spheres . The Si-Si bonds are indicated for the equilibrium bond lenght 2.35 Å by the blue line, and for the ones under tensile or compressive strain by red lines or green line respectively. The superposition of the black dots that indicate the c-Si lattice positions onto the Si cluster structure, obtained after many H interaction events, shows that the rearranged atomic positions in the Si cluster correspond well with the equilibrium c-Si lattice sites. 52

2.7 .(a) FTIR transmission spectra for silicon hydrogenated layer deposited with the different R=H_2/SiH_4 ratios, as listed in the legend on the right of the Figure, and (b) FTIR experimental data for the same sample as in a) for the 1850-2250 cm-1 range, after the background subtraction. 54

2.8 Integral of the FTIR signal for the several samples plotted as a function hydrogen dilution, and normalised respect to the signal for the sample R=10 F_{SiH4}=12 sccm,(a) and Hydrogen content of the films obtained by ERDA (b) as a function hydrogen dilution, and normalised respect to the same sample. 55

2.9 FTIR experimental data for the several samples (graph (a) to (f)), and results of the gaussian deconvolution, by using the frequencies listed in table 1 relative to SiH, SiH_2 and SiH_3. The vertical thin lines represent the position of these literature values for the stretch vibrational modes of SiH(2000 cm^{-1}), SiH_2(2090 cm^{-1}), SiH_3(2140cm^{-1}). The blue curves represent the raw data, while red curves represent the convolution of the three components. . . 57

2.10 Si-H3 bonded species correlated with the SiH bonding, for several sample. The triangles represent the layer deposited with F_{SiH_4}=100 sccm, while the square represent the layer sequence deposited with F_{SiH_4}=12 sccm. 58

2.11 TEM Micrograph in bright field condition of R=20 sample, showing the Silicon substrate (dark grey region), the SiO_2 substrate (light grey region=) and the deposited Si:H layer, which shows a polycolumnar morphology in the upper part of the layer. (b) Mean size of nanostructure at various R for samples deposited withF_{SiH4} =12 sccm, obtained through plan view TEM analysis in Dark field condition. The data represent the mean radius of the dots present in the surfacial region of the Si:H layer. 59

2.12 TEM Micrograph in bright field condition of R=40 sample, showing white regions, evidenced by the arrows, that represent the nanovoids created by hydrogen, and appear in correspondence of the grain boundaries. 60

3.1 (a) SEM Micrograph in tilted view (30° along the y axis) of the nanoporous SiO_2 template realised by nanopatterning based on diblock copolymer self-assembly. The analysis was performed on the cleaved edge of the sample. It is possible to identify the Si substrate in the bottom and the etched oxide layer on top. (b) Cross-section TEM image of a sample: it is visible the 15 nm oxide layer etched down to the Si substrate for about 8 nm. The black line shows the typical etch profile in the oxide layer of the samples. The total pore depth is about 23 nm and the curvature radius at the bottom of the nanopores is about 6 nm.[26] 71

3.2 Bright field TEM micrograph of a templated oxide substrate after sputtering of gold nanodots. The white regions represents the nanopores in the SiO_2 substrate and the black dots represent the gold nanodots deposited randomically on the substrate.[26] 72

3.3 TEM micrographs in plan view of the nanopatterned oxide substrates of, after deposition of Au dots and annealing for 1 hour at 600 °C (a) and 800 °C (b). In a) it is possible to see the nanopores in the SiO2 substrate and the randomic Au nanodots (dark spots), while in b) the ordered Au dots saturating the nanopores together with few dots outside the nanopores.[26] 74

3.4 Gold dot radius distributions in the as deposited samples (circles) and for the samples annealed for 1 hour at 600 °C (squares), 800 °C (diamonds) and 1000 °C (triangles).[26] 75

3.5 Au dot density (a), diameter (b) and coverage (c) for the as deposited samples (circles) and for the samples annealed for 1 hour at 600 °C (squares), 800 °C (diamonds) and 1000 °C (triangles).[26] . 77

3.6 (a) SEM images in plan view of the nanopatterned oxide substrates after the deposition of Au dots and annealing at 1000 °C for 1h. It is possible to see the nanopores in the SiO_2 substrate (black circles) and the gold nanodots diffused in the nanopores (white spots).(b) Cross-section TEM micrograph of the sample show one nanopore completely filled with the gold and some empty pores close to it.[26] 78

3.7 (a) The Gibbs free energy differential as a function of volume and surface term for a cluster on a surface, and (b) schematic illustrating the Young-Duprè equation for the surface and Interface tension terms for a cluster in its equilibrium shape with a contact angle[33] 80

3.8 a) Sketch of the cluster's evolution, the red arrow indicate the adatoms that leave the cluster with size R<R* and adatoms that diffuse toward the cluster with R>R*due to the adatoms concentration gradient. b) Superposition of concentration distance and energy distance diagram for two dimensional cluster on a surface, showing the different energy levels involved in cluster growth[33] . 82

3.9 Experimental value of Ds for the SiO_2 substrate(triangles) as a function of $T^{-1}$with the relative Arrhenius fit (continuius line) [42]. The inset is a scale picture which rapresents our pattern where the blue circle are the pores and the gold sphere are the cluster, the pink shape represents the aspected diffusion area after 1 hour of annealing 83

3.10 Bright field TEM micrographs acquired during the *in situ* thermal annealing at 700 °C for (a) 2s, (b) 58s, (c) 116 s, (d) 169 s. The pores are evidenced by the white dashed circles, and identified as P_1, P_2 and P_3. The black shapes highlight several groups of dots which diffuse on the substrate and/or toward the pore. A group of Au dots which diffuse toward one of the nanopores of the substrate are identified by number 1 to 7 . The ripening of some groups of Au dots identified by α, β and γ is evidenced by the black arrows (a), (b) and (c). 85

3.11 TEM micrograph in plan view of the nanopatterned oxide substrate after deposition of Au dots and annealing for 1 hour at and 800 °C. It is possible to see the Au NDs in correspondence of the nanopores underneath, arranged in the hexagonal configuration, as evidenced by the red hexagons. 86

List of Tables

1.1 list of parameters and respective values used in our simulations. . . 31

2.1 Si-H vibrational modes [31] 53

Introduction

0.1 General overview

Photovoltaic technology has received increased attention as one of the most promising approach to carbon-free energy production. Bulk silicon cells, which convert between 14 and 17% of incident light into electricity, make up 90% of the solar cell market. Silicon is widely used because it is the second most abundant element in the earth's crust, and because the electronics industry has already developed infrastructure to process it. Yet the pricey and complicated manufacturing makes these photovoltaic (PV) systems more expensive per kW/h than conventional energy sources. These limitations have driven efforts to develop inexpensive solar modules with efficiencies equivalent to, or better than, existing devices. Thin films solar cells are widely recognized as a key solution to reducing the manufacturing cost of PV cells in the near to medium term. Thin film solar cells are able to be produced at low cost by removing the bulk active substrate and using an additive deposition process on top of a low cost substrate such as glass, metal foil, plastic, etc. Compared with other thin-film solar cell technologies, thin-film silicon has the advantage of constituting an industrially mature technology and of being based on raw materials which are present in abundance in the earth's crust.[1] During the last three decades, hydrogenated amorphous silicon has been studied extensively as basic material for thin film solar cells due to the natural abundance of source material, environmental safety, potential high performance and the capability of low cost production. However, the defect density of hydrogenated amorphous silicon (a-Si:H) increases with light exposure, to cause an increase in the recombination current and leads to the reduction in the sunlight to electricity conversion efficiency. This phenomenon is known as Staebler-Wronski effect [2] For this reason, the solar cells based on a-Si:H have always been associated with efficiency losses due to the light-induced degradation over the time. For amorphous silicon the photoinduced degradation due to the creation of dandling bond defect has been the most important issue for improving the efficiency [3] Extensive research has been carried out by many laboratories to improve the conversion efficiency of a-

Si:H solar cells [4]. In this thesis an intensive study on thin film a-Si:H solar cells will be shown.The fundamental photodiode inside an amorphous silicon–based solar cell has three layers deposited in either the p-i-n or the n-i-p sequence. The realization of a pin solar cell will be shown, including the investigation of the key physical properties necessary to design the solar cell (sheet resistance, activation energies for conductivity, light absorption). The electrical characteristics of the solar cells in dark condition and under standard illumination will be presented and compared to the theoretical models.

In order to make photovoltaic technology cost effective we need to improve the efficiency and minimize the light induced degradation of photoconductivity caused by Staebler–Wronski effect [2]. A material that presents very promising features is hydrogenated nanocrystalline silicon (nc-Si:H)[15]. The nc-Si:H is made using PECVD,

In order to make photovoltaic technology cost effective we need to improve the efficiency and minimize the light induced degradation of photoconductivity caused by Staebler–Wronski effect. A material that presents very promising features is hydrogenated nanocrystalline silicon (nc-Si:H). The nc_Si:H is made using PECVD, using a gas mixutre of SiH_4 and H_2, the cristalline dimension can be tailored by variyng the hydrogen dilution of Silane in PECVD camera. The transition from amorphous to nanocrystalline silicon is induced by Hydrogen. Vettel et al [5]demonstrated an important result, the deposition condition near the transition between amorphous an cristalline growth have been found to be the most beneficial to the solar cells properties. Nc-Si:H films show stability under light soaking, suggesting that the disorder in the amorphous Si network plays a major role, and thus Nc-Si:H have high potential as stable solar cell material. The parameter that could play a role in the stability under light soaking and also in the crystalline fraction is believed to be the hydrogen concentration and its complex bonding mechanism. The major technical challenge with such nanocrystalline solar cells is the fact that the surface area of grain boundaries is very high, significantly increasing the density of recombination centers as well as the probability of recombination due to charge carriers having to pass through so many boundaries, indicating that the crystalline fraction and the grain size of these materials determine also the electrical properties of the final device. It is believed that the hydrogen content and its complex bonding behavior is the responsible for the structural characteristics and as a consequence for the stability under illumination. In order to control the optical and electrical properties and then the stability under light soaking effect, the hydrogen contribution must be deeply understood. In this thesis a study of the morphological behaviors of nc-Si:H films as a function of the hydrogen content will be showed. Nc-Si:H thin films were deposited by ST microelectronics under different conditions by PECVD deposition by varying the ratio H_2/SiH_4 flow. The variation of morphology and hydrogen content was studied in detail, using

TEM analysis, ERDA and FT-IR measurements. The study of this material was also made using the radial distribution function (RDF), which starting from the diffraction pattern of TEM analysis, gives the number of atoms at a given distance from a central atom. The contribution of the hydrogen in the transition from an a-Si:H layer, with low R, to a nc-Si:H layer, with high R, will be demonstrated.

As previously described, in contrast to amorphous silicon (a-Si), nc-Si exhibits high stability against photo-induced degradation. However, nc-Si thin-film solar cells require an intrinsic layer of 2–3 μm in thickness to absorb sufficient amount of sunlight due to its indirect optical transition. For this reason in literature another type of nanostructure, has been recently proposed, the Si nanowires. Silicon nanowires offer several performance and manufacturing benefits that may impact future PV applications. Their main advantage is based on the fact that they orthogonalize the pathways for light absorption and carrier collection. Recently Atwater et al. reported the potential of radial p-n junction wire array solar cells, which consist of a dense array of semiconducting wires, each having a p-n junction in the radial direction, and oriented with the nanowires axis parallel to the incident light direction. By fabricating p-n junctions conformally around the wires structure, in a radial configuration, the absorption of light can be decoupled from minority carrier diffusion. This approach is useful to the creation of efficient solar cells using low lifetime materials. [7, 1]. Although fabrication of wires in micrometer sized dimension have been proposed in many works to prevent the surface recombinarion, the approach proposed in this thesis is the use of nanometer sized dimention to the nanowires syntesis. The choice of using these nano-structures is driven by numerous factors. The possibility of a switch to an almost direct gap with the ability to vary the energy gap by varying the diameter of the wires is one of the main factors. Zhao et [10]found that for a nanowires oriented in [100] direction with diameter of about 6-8 nm the resulting energy gap is about 1.4 eV. This result is very close to the Shockley–Queisser limit[**?**]. The theoretical maximum almost corresponds to the GaAs band gap. (1.42 eV), However, due to high production costs GaAs is reserved for solar applications, for this reason in very interesting the use of a technique that is able to achieve an Eg of 1.4 with low cost production. There are two basic approaches of synthesizing nanowires: top-down and bottom-up approach. A top-down approach combines lithographic steps or etching process to produces nanowires from a flat surface. The major drawback of the top-down method is that the surfaces of the structure are damaged during the process resulting in nanowires with a poor crystal quality. In addition the lithographic techniques may not be able to produce sufficiently small structures for further downscaling of devices. In order to produce small enough nanowires of high enough crystal quality, the bottom-up approach is thought to be a potential alternative. The idea is to build-up nanosized structures and devices by using nanoscale building blocks to initiate growth directly at desired positions and with designed dimensions and properties. In contrast to the lithographic and etching techniques used in the top-down methodology, the bottom-up approach involves the direct growth of one-dimensional nanostructures onto a substrate. The typical method to fabricate NWs by bottom-up approach is the catalytic growth with random metallic nanoparticles. A better understanding of the catalytic nanowire growth process is necessary to pin down the growth mechanism and to be able to rationally control their compositions, sizes, crystal structures, and growth directions. Gold was used as a catalyst for the nucleation of the Si nanophase. The choice to use gold relies on the advantages of this metal respect to others, like Ni, Sn, Al and Cu, such as its low eutectic temperature with Si, the opportunity to easily form alloys with the growth precursor and the fast inter-diffusion of Si through gold nanodot. Gold, however, presents some drawbacks, because it creates deep band gap defects and for this reason the data shown represent a proof of concept, and alternative metals must be investigated for device integration. The catalytic growth of silicon nanowires is commonly described either by the vapor-liquid-solid (VLS) or solid-liquid-solid (SLS) process. The VLS process was first suggested by Wagner and Ellis [11]who showed that micrometer-scale silicon whiskers could be grown from metal droplet catalysts under Chemical Vapor Deposition conditions at about 1000 °C. A typical VLS mechanism starts with the dissolution of gaseous precursors (SiH_4 or SiH_2Cl_2) into nanosized liquid alloy (metal Au-Si) droplet considered as a catalytic site. Once the liquid droplet is supersaturated with silicon, then the precipitation of solid nanowire occurs. The process was named the VLS beacuse of the three phases involved. In this method, metallic nanoparticles are deposited randomically on a Si substrate and work as catalysist seeds for the nucleation of the Si phase from the vapor source, in the first case, and from the substrate source, in the second case. During the growth, in both cases however, some lateral diffusion of the metallic dots on the substrate can produce a coalescence of the metal nano-seeds, thus increasing the disorder level in the template substrate, and producing a final "forest-like" material. Therefore, when position control of spatially separated NWs is desired, nanopatterning techniques become essential. Some approaches have been demonstrated, or are potentially applicable, for position and size control of semiconductor NWs. [11] A number of patterning and templating methods can be applied for the controlled preparation of metal dots or metal-dot arrays on a substrate surface, including photo- or e-beam lithography, manipulation of single gold nanodots, arrangement of Au nanocrystals from suspensions, nanosphere lithography, gold deposition masks based on porous alumina templates, nanoimprint lithography, as well as other catalyst-positioning approaches. Since the final structural and geometrical characterisitcs of the NWs are strictly correlated to the catalyst dot properties, we want to control the catalytic seed characteristics, such as shape, position, dimension and we create a SiO_2 barrier to the lateral diffusion during the annealing to control the final nanowires template. In this thesis we propose an approach to obtain these characteristics based on a two steps process. i) First of all the formation of a polymeric nanomask by diblock copolymer self-assembling [13, 14, 15] and successive dry etch to transfer the polymeric pattern on the oxide substrate [16, 17, 18, 19, 20]. This creates an ordered array of nanopores of controlled size and density and position. The obtained substrate is made of a silicon dioxide layer with nanopores 20 nm wide and separated by a 40 nm distance, etched down to the Si substrate. ii) Afterwards, catalyst nanodots was deposited and diffused over the template. A single layer of gold NDs, with coverage 20%, is deposited by sputtering all over the template, and subjected to thermal annealing at temperatures ranging between 600 and 1000 °C, to diffuse the metallic NDs on the surface. In this thesis it is shown that the NDs deposited randomically over the template either inside and outside the pores, during the annealing diffuse and coalesce randomly over the substrate, but in correspondence of the nanopores they stop the diffusion, probably due to the presence of some surfacial defects. The final result of this process is that most of the nanopores are saturated with the gold NDs. The density of saturated nanopores can be tuned by changing the annealing temperature. The preferential diffusion of the gold NDs toward the nanopores is followed *in situ* by annealing the samples during TEM imaging, and *ex-situ* by annealing in furnace the samples and observing them by TEM and high-statistics SEM analysis.

0.2 Thesis outline

The first chapter describes the pin cells realization. To explain the characteristic of hydrogenated amorphous silicon in the first section, we introduce some of the fundamental physical concepts required to interpret the scientific literature about amorphous silicon.The second section describes the electrical and optical characterization of the layer that compose the solar cells, and an accurate electrical characterization of the pin structure realized by ST.

The second chapter shows the characterization of nc-Si:H thin films made by PECVD for solar cells. In particular a structural characterization performed by TEM analysis will be showed, and the role of hydrogen in the transition from a-Si:H to nc-Si:H will be deeply analyzed and discussed.

The third chapter shows results on the fabrication of ordered nanowires. It uses an alternative lithography based on diblock copolymer self-assembling which generates ordered arrays of nanopores of controlled size, density and position. This can be used as a template for the catalytic mediated growth of controlled nanowires.

References

[1] L. Tsakalakos. Materials Science and Engineering R 62 (2008) 175–189

[2] Staebler, D. L.; Wronski, C. R. Applied Physics Letters , vol.31, no.4, pp.292-294, Aug 1977 doi: 10.1063/1.89674

[3] Kondo et. al. Thin solid films 501 (2006) 243-264.

[4] [4] Funde et al. Solar Energy Materials & Solar Cells 92 (2008) 1217– 1223.

[5] O. Vetterl, F. Finger, R. Carius, P. Hapke, L. Houben, O. Kluth, A. Lambertz, A. MuKck, B. Rech, H. Wagner. Solar Energy Materials & Solar Cells 62 (2000) 97}108

[6] A. V. Shah, H. Schade, M. Vanecek, J. Meier, E. Vallat-Sauvain, N. Wyrsch, U. Kroll, C. Droz and J. Bailat. Prog. Photovolt: Res. Appl. (2004); 12:113–142

[7] B.M.Kayes, H.A. Atwater N.S. Lewis. J. Appl. Phys. 97, 114302 (2005)..

[8] Tsakalakos Appl. Phys. Lett. 91 233117(2007).

[9] W. Shockley, H.J. Queisser, J. Appl. Phys. 32 (1961) 510.

[10] Xinyuan Zhao, C. M. Wei, L. Yang, and M. Y. Chou. PHYSICAL REVIEW LETTERS 92(23),236805 (2004)

[11] R.S. Wagner, W.C.Ellis: Vapor- Liquid-Solid Mechanism of single crystal growth. Appl Phys Lett . 4, 89-90 (1964).

[12] H.J. Fan, P. Werner, M. Zacharias: Semiconductor Nanowires: From Self-Organization to Patterned Growth. Small. 2:700-17 (2006).

[13] K.W. Guarini, C.T. Black, S.H.I. Yeung: Optimization of Diblock Copolymer Thin Film Self Assembly. Adv. Mater. 14 (18), 1290 (2002).

[14] T. Thurn-Albrecht, J. Schotter, G.A. Kastle, N. Emley, T. Shibauchi, L. Krusin-Elbaum, K. Guarini, C.T. Black, M. T. Tuominen, T. P. Russell: Ultrahigh-Density Nanowire Arrays Grown in Self-Assembled Diblock Copolymer. Templates.Science. 290, 2126 (2000)

[15] I.A.Zucchi, E.Poliani and M.Perego: Microdomain orientation dependence on thickness in thin films of cylinder-forming PS-b-PMMA. Nanotechnology 21 (2010) 185304

[16] S.J. Kim, W.J. Maeng, S.K. Lee, D.H. Park, S.H. Bang, H.Kima, B.H. Sohn: Hybrid nanofabrication processes utilizing diblock copolymer nanotemplate prepared by self-assembled monolayer based surface neutralization. J. Vac. Sci. Technol. B 26(1), 189-194 (Jan/Feb 2008).

[17] K.W. Guarini, C.T. Black, Y. Zhang, H. Kim, E.M. Sikorski, I.V. Babich: Process integration of self-assembled polymer templates into silicon nanofabrication. J. Vac. Sci. Technol. B, 20(6), 2788-2792 (2002).

[18] K.W. Guarini, C.T. Black, K.R. Milkove, R.L. Sandstrom: Nanoscale patterning using self-assembled polymers for semiconductor applications. J. Vac. Sci. Technol. B.19(6), 2784-2788 (2001).

[19] P. La Fata, R. Puglisi, S. Lombardo, C. Bongiorno: Nano-patterning with Block Copolymers. Superlattices and Microstructures. 44 693–698 (2008).

[20] R.A. Puglisi, A. Scandurra, C. Bongiorno, P. La Fata and S. Lombardo: Pattern transfer of nanomasks based on diblock copolymers through Reactive Ion Etching (to be submitted).

Chapter 1

aSi:H Thin Film solar cells

1.1 Introduction

Silicon is the semiconductor of choice in Photovoltaic Industry. In fact, silicon is abundant, environmentally inert and is one of the technically and scientifically most advanced materials. However, standard silicon photovoltaic technology suffers from several drawbacks: the processes are energy consumptive, too much material is wasted during processing, the cells are -for technical limitations- much thicker than what would be needed, and large area and module fabrication is awkward[2, 1]. On the other hand, conversion efficiencies are high and as mentioned above, the technology is well advanced. Therefore, it has ever been the challenge to improve on those drawbacks while keeping the silicon advantages. One way is the so-called thin film silicon solar cell. There are two forms of thin-film silicon material that can be used for constituting such a solar cell: hydrogenated amorphous silicon (a-Si:H) and hydrogenated microcrystalline silicon (μc-Si:H) or hydrogenated nano-crystalline silicon (nc-Si:H). With this device one wants to reduce film thickness to what is a minimum needed for complete solar light absorption, reduce process temperatures in order to use low-cost substrate materials and use processes which allow large area fabrication and integration into modules. Such thin-film silicon solar cells require a far lower amount of silicon material than the 'classical' wafer- based crystalline silicon solar cells; this means that they have, on a medium-term time scale, a more pronounced cost reduction potential than the latter. Furthermore, the *'energy payback time'*, i.e., the time required for the photovoltaic solar module to 'pay back', to the user, the quantity of energy invested during its fabrication, is at least a factor of two lower in the case of thin-film silicon solar cells than for wafer-based crystalline silicon solar cells: this may, in the long run, turn out to be a decisive factor. Compared with other thin-film solar cell technologies, thin-film silicon has the advantage of constituting an industrially mature technology and of being based on raw materials which are present in abundance in the earth's crust. Their stabilized efficiency is, however, at this moment still rather limited, for reasons which we will see later in this chapter in section 1.3.3. This is where hydrogenated nanocrystalline silicon (nc-Si :H) prepared by plasma-enhanced chemical vapour deposition (PECVD) enters [2, 1]. Being in the field for long in amorphous silicon-based devices as highly conductive contact layer, recently much progress has been made to control the process of fabrication in order to achieve improved deposition rates and high electronic quality such that now nc-Si :H can be used as active layer in solar cells [3, 4, 5, 6]. This chapter is organized as follows. The first section describes how the simplest, single-junction solar cell "works," by which we mean how the photoelectric behavior of the cell is related to the fundamental concepts. After this we introduce the hydrogenated amorphous silicon the deposition technique and some of the fundamental physical concepts required to interpret the main characteristics of the hydrogenated amorphous silicon materials. The drawbacks related to the Staebler-Wronsky effect are shown in the section1.3.3, and some solutions such as the nanocrystalline silicon are presented later in the chapter. The results and discussion section reports the activity performed by us of thin films deposition and characterization, pin PV cell design and pin PV cell realization and characterization

1.2 Semiconductor Solar cells.

Semiconductor solar cells are quite simple devices. Semiconductors have the capacity to absorb light and to deliver a portion of the energy of the absorbed photons to carriers of electrical current –electrons and holes. A semiconductor diode separates and collects the carriers and conducts the generated electrical current preferentially in a specific direction.[7] Thus, a solar cell is simply a semiconductor diode that has been carefully designed and constructed to efficiently absorb and convert light energy from the sun into electrical energy. A simple conventional solar cell structure is depicted in Figure 1.2 Sunlight is incident from the top on the front of the solar cell. A metallic grid (indicates by the arrow in fig 1.1) forms one of the electrical contacts of the diode and allows light (orange arrows) to fall on the semiconductor between the grid lines and thus be absorbed and converted into electrical energy. An antireflective layer (Anti Reflection Coating, ARC) (indicates by the arrow in fig. 1.1 a) between the grid lines increases the amount of light transmitted to the semiconductor. The semiconductor diode is fashioned when an n-type semiconductor and a p-type semiconductor are brought together to form a metallurgical junction. This is typically achieved through diffusion or implantation of specific impurities (dopants) or via a deposition process. The diode's other electrical contact is formed by a metallic layer (purple zone)on

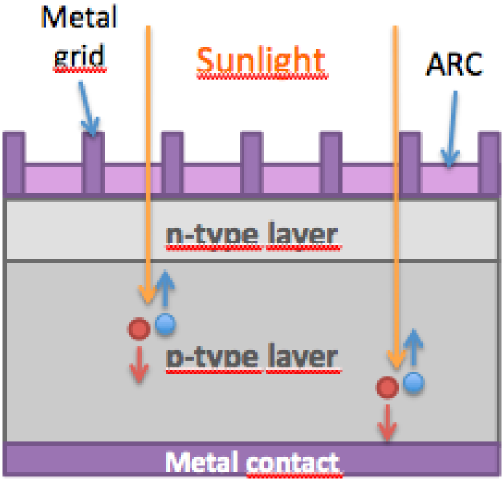

Figure 1.1: A schematic of a simple conventional solar cell. Creation of electron–hole pairs, blue circle and red circle, respectively, is depicted

the back of the solar cell.

In the following section a discussion on the key electrical parameter to characterize solar cells is reported.

1.2.1 Solar Cell I –V Characteristics

Equation (1) is a general expression for the current produced by a solar cell.

$$I = I_{SC} - I_{o1}(e^{qV/kT} - 1) - I_{o2}(e^{qV/2kT} - 1) \tag{1}$$

The short-circuit current and dark saturation currents are given by rather complex expressions [7] that depend on the solar cell structure, material properties, and the operating conditions. A full understanding of solar cell operation requires detailed examination of these terms. However, much can be learned about solar cell operation by examining the basic form of equation (1). From a circuit perspective, it is apparent that a solar cell can be modeled by an ideal current source (I_{SC}) in parallel with two diodes, the first with an ideality factor and the the other with an ideality factor of “2”, as shown in Figure1.2 a) .

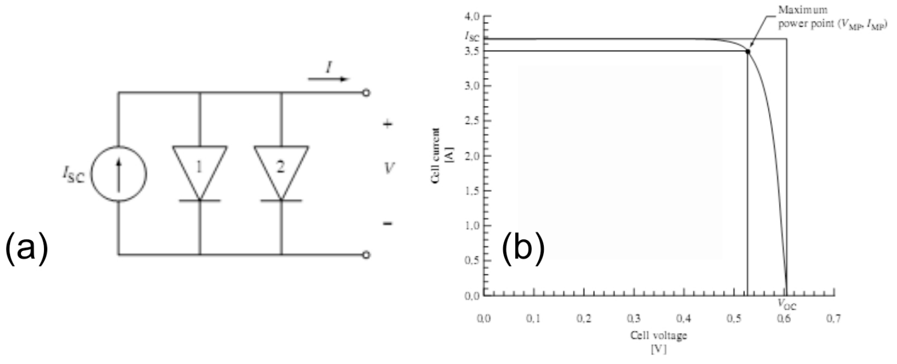

Figure 1.2: Simple solar cell circuit model. Diode 1 represents the recombination current in the quasi-neutral regions ($\propto e^{qV/kT}$), while diode 2 represents recombination in the depletion region ($\propto e^{qV/2kT}$)(b)[7]

Figure 1.2 b) shows the current – voltage (I – V) characteristic of a typical silicon solar cell. For simplicity, the dark current due to the depletion region (diode 2) has been ignored (a reasonable and common assumption for a good silicon solar cell, especially at larger forward biases). From The figure 1.2 b illustrates key parameter of solar cells – the short-circuit current I_{sc}, the open-circuit voltage V_{OC}, and the fill factor FF. At small applied voltages, the diode current is negligible and the current is just I_{sc}, as can be seen when V is set to zero in equation (1). When the applied voltage is high enough so that the diode current (recombination current) becomes significant, the solar cell current drops quickly. At open circuit (I = 0), all the light-generated current, I_{sc}, is flowing through diode 1, so the open-circuit voltage can be written as

$$V_{OC} = \frac{kT}{q} \ln \frac{I_{SC} + I_{o1}}{I_{o1}} \approx \frac{kT}{q} \ln \frac{I_{SC}}{I_{o1}}, \tag{2}$$

where $I_{SC} \gg I_{o1}$.

the maximum power point $P_{MP} \equiv (V_{MP}, I_{MP})$,i.e. is the point on the I–V curve where the power produced is at a maximum. As seen in Figure 1.2b this point defines a rectangle whose area, given by $P_{Max} = V_{MP} I_{MP}$, is the largest rectangle for any point on the I –V curve. The maximum power point is found by solving

$$\left.\frac{\partial P}{\partial V}\right|_{V=V_{MP}} = \left.\frac{\partial (IV)}{\partial V}\right|_{V=V_{MP}} = \left.\left[I + V\frac{\partial I}{\partial V}\right]\right|_{V=V_{MP}} = 0 \qquad (3)$$

for V = VMP. The current at the maximum power point, IMP, is then found by evaluating equation (1) at V = V_{MP}.

Another important characteristic is the fill factor, FF, which is a measure of the squareness of the I–V characteristic and is always less than one. It is the ratio of the areas of the two rectangles shown in Figure 1.2 b) or

$$FF = \frac{P_{MP}}{V_{OC} I_{SC}} = \frac{V_{MP} I_{MP}}{V_{OC} I_{SC}} \qquad (4)$$

Obviously for a solar cell the power conversion efficiency, η, is the most important parameter to analyze; η is defined as

$$\eta = \frac{P_{MP}}{P_{in}} = \frac{FF\, V_{OC} I_{SC}}{P_{in}} \qquad (5)$$

The incident power, Pin, is determined by the properties of the light spectrum incident upon the solar cell. In the following section the light spectrum property will be discussed.

1.2.2 Air Mass

The sun has a surface temperature of 5762 K and its radiation spectrum can be approximated by a black-body radiator at that temperature. Emission of radiation from the sun, as with all black-body radiators, is isotropic. However, the Earth's great distance from the sun means that only those photons emitted directly in the direction of the Earth contribute to the solar spectrum as observed from Earth. Therefore, for practical purposes, the light falling on the Earth can be thought of as parallel streams of photons. Just above the Earth's atmosphere, the radiation intensity, or Solar Constant, is about 1.353 kW/m^2 [8] and the spectral distribution is referred to as n air mass zero (AM0) radiation spectrum. The Air Mass is a measure of how absorption in the atmosphere affects the spectral content and intensity of the solar radiation reaching the Earth's surface. The Air Mass number is given by $AirMass = 1/cos\theta$ where θ is the angle of incidence ($\theta = 0$ when the sun is directly overhead). A widely used standard for comparing solar cell performance is the AM1.5 spectrum normalized to a total power density of 1 kW/m^2 . The spectral content of sunlight at the Earth's surface also has a diffuse (indirect) component owing to scattering and reflection in the atmosphere and surrounding landscape and can account for up to 20% of the light incident on a solar cell. The Air Mass number is therefore further defined by whether or not the measured spectrum includes the diffuse component. An AM1.5g (global) spectrum includes the diffuse component, while an AM1.5d (direct) does not . [7]

1.3 Hydrogenated amorphous silicon

Hydrogenated amorphous Si is deposited from hydride gases such as SiH_4 using plasma to decompose the gas. This is called plasma-enhanced CVD (PECVD) and allows for large areas to be coated rather uniformly and with excellent control. However, the utilization of gases is only around 10 to 30%, meaning much of the source material is wasted. The material has 1 to 10% hydrogen bonded to the Si, and is often designated as a-Si:H. The H atoms passivate a large number of the defects resulting from the incomplete bonding of the Si atoms. The atomic structure has no long-range order like all other crystalline or polycrystalline materials. This will be deeply analyzed in chapter 2. This can be an advantage. Films are typically deposited between 150 to 300°C, this temperature conditions allowing the use of lower-cost, low-temperature substrates like glass, stainless steel foil, or plastic. The pn junction is formed by doping the thin contact layers as they grow with dopant gases containing the boron or phosphorous atoms. In the following section will be discussed how the PECVD works. And after, to explain the characteristic of hydrogenated amorphous silicon in the following section we briefly introduce some of the fundamental physical concepts required to interpret the scientific literature about amorphous silicon.

1.3.1 PECVD

As as above-mentioned a-Si:H is deposited from hydride gases such as SiH_4 using plasma to decompose the gas. Figure**??** shows a schematic of a typical RF PECVD chamber and related parts. A silicon-containing gas such as a mixture of SiH_4 and H_2 flows into a vacuum chamber that is evacuated by a pump. Two electrode plates are installed inside, and an RF power is applied between them; one option is to ground one of these electrodes. At a given RF voltage across the plates, there is usually a range of gas pressures for which a plasma will occur. The plasma excites and decomposes the gas and generates radicals and ions in the chamber. Various substrates may be mounted on one or both of the electrodes, and thin hydrogenated silicon films grow on the substrates as these radicals diffuse into them. The substrates are heated to achieve optimum film quality; this effect is attributed to thermally activated surface diffusion of adatoms on the growing film.

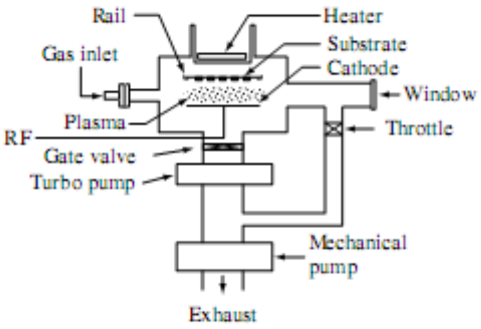

Figure 1.3: Schematic of a typical RF glow discharge deposition chamber[15]

A PECVD system usually consists of several major parts (shah):

1)a gas delivery system (gas cylinders, pressure regulators, mass flow controllers, and various gas valves to direct gas flows);

2) a deposition chamber that has electrodes, substrate mounts, substrate heaters, and the RF power feed through;

3)a pumping system that usually has a turbomolecular pump backed with a mechanical pump;

4) a pressure control system that has a capacitance manometer, ionization gauges, thermocouple gauges, and/or throttle valve to monitor and control the chamber pressure;

5)an exhaust system for the process gases (typically either with a chemical scrubber to neutralize the gases or with a “burn box” to pyrolyze them).

The film growth in a PECVD process consists of several steps: source gas diffusion, electron impact dissociation, gas-phase chemical reaction, radical diffusion, and deposition [11, 9, 10]. To deposit good-quality a-Si films, the deposition conditions need to be controlled within certain ranges desirable for high-quality a-Si growth.

The pressure range is usually between 0.05 and 2 Torr. Lower pressure is desirable for making uniform deposition, and higher pressure is more desirable for preparing microcrystalline silicon films. Most researchers use a pressure between 0.5 and 1 Torr for a-Si deposition. The RF power should be set at around 10 to 100 mW/cm^2 for a capacitively coupled reactor. Below 10 mW/cm^2, it is difficult to maintain a plasma. Higher power is desirable for higher deposition rate. However, above 100 mW/cm^2, the rapid reactions in the gas can create a silicon polyhydride powder that contaminates the growing Si film. This problem can be mitigated by using very low pressure or strong hydrogen dilution. The substrate temperature is usually set between 150 and 350°C. At lower substrate temperature, more H is incorporated in the film.

1.3.2 Characteristics of a-Si:H

Silicon atoms in amorphous silicon largely retain the same basic structure as that of crystal silicon: each silicon atom is connected by covalent bonds to four other silicon atoms arranged as a tetrahedron. Moreover, not all the atoms within amorphous silicon are fourfold coordinated. Due to the disordered nature of the material some atoms have a dandling bond. Physically, these dandling bonds represent defects in the continuous random network and may cause anomalous electrical behavior. For hydrogenated amorphous silicon (a-Si:H), silicon–hydrogen bonds resolve this structural problem. Several percent of the silicon atoms make covalent bonds with only three silicon neighbors; the fourth valence electron of the silicon bonds to a hydrogen atom. There are quite a few distinct atomic configurations for the hydrogen in a-Si:H. The two principal “phases” of hydrogen evidenced by proton magnetic resonance are termed the dilute and clustered phases [12]. In the dilute phase a particular hydrogen atom is about 1 nm away from any other hydrogen atom; in the clustered phase there are two or more hydrogen atoms in close proximity. A computer calculation of a particular instance of this structure [13] is presented in Figure 1.4. The densities of hydrogen in each of the individual phases, as well as the total density of hydrogen, depend upon the conditions under which the material is made.

While the underlying structure illustrated in Figure1.4 is noncrystalline, it is a chemically ideal structure: each atom forms the normal number of chemical bonds (four for silicon, one for hydrogen). This noncrystalline atomic structure largely determines the overall electronic and optical properties of the material, as we will discuss shortly. Many electronic properties in a-Si:H are also strongly affected by the gross defects of chemical bonding. The atomic structure of the bonding defects in a-Si:H has been extensively studied using electron spin resonance. A single type of defect, the D-center, dominates most measurements in undoped a-Si:H [15]. The D-center is generally identified as a silicon dangling bond [14].

A dangling bond may be envisioned using Figure 1.4: just imagine that the hydrogen atom is removed from the dilute-phase site in the lower right-hand corner of the figure, leaving behind a single unbonded electron (the “dangling bond”). This simple picture is consistent with the observation of fig 1.5: the density of dangling bonds increases when hydrogen is removed from a-Si:H by heating. We present a comparison of a model for this relationship together with measurements illustrating the effect in Figure 1.5. Note that the density of dangling bonds is generally much lower than the density of hydrogen lost from the structure; this effect has been attributed to the evolution of hydrogen from clustered-phase sites, which presumably does not create dangling bonds.

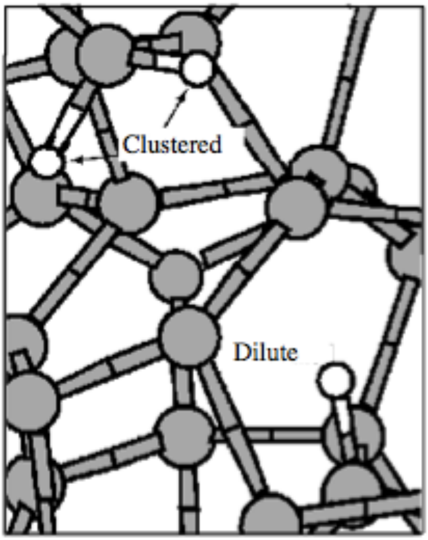

Figure 1.4: Computer model of the chemical bonding of hydrogenated amorphous silicon. The larger, gray spheres indicate Si atoms; the smaller, white spheres indicate hydrogen atoms, which are found in clustered and relatively isolated, dilute-phase configurations as indicated[7].

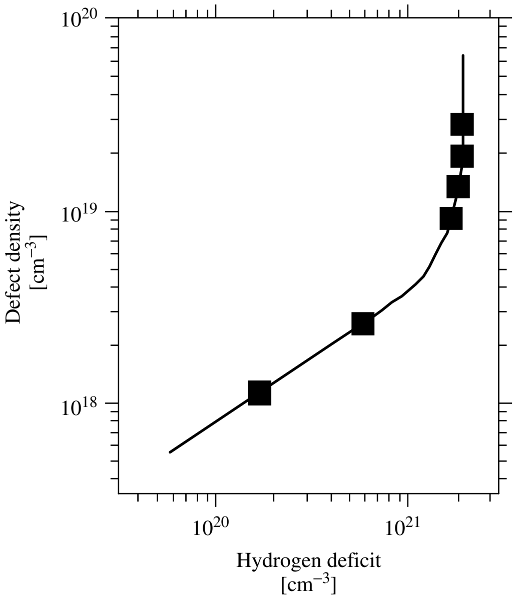

Figure 1.5: Correlation of the defect (dangling bond) density in a-Si:H with the density of hydrogen removed from the material by heating (the hydrogen deficit). The data points are derived from deuterium and defect profiles by Jackson et al.[16] (350○C deuteration). The curve is a fit to a model proposed by Zafar and Schiff[17]

1.3.3 Staebler–Wronski

One of the crucial issue of the a-Si:H thin film solar cells is the significant decline in their efficiency during their first few hundred hours of illumination. A-Si:H cells exhibit this type of initial behavior under illumination; the behavior is mostly due to the "Staebler–Wronski" effect (SW)[1], which is the light-induced change in hydrogenated amorphous silicon (a-Si:H) and related materials used in the cell.

Semiconducting hydrogenated amorphous silicon (a - Si:H) thin films can be grown with fewer than $10^{15} cm^{-3}$ neutral threefold-coordinated Si dangling-bond (DB) defects. However, the introduction of excess carriers through moderate illumination or electronic injection increases the density of DB's to nearly $10^{17} cm^{-3}$, even in the most degradation- resistant materials.[1–5] For purposes of engineering and commercial applications, it is very important that a-Si:H reaches such a "stabilized" condition after extended light soaking.

Although the defect density is not the only property of a-Si:H modified following light soaking [18], most workers believe that the principal cause of the Staebler–Wronski effect is this increase in dangling bond density after light soaking. The close connection between hydrogen and defects in a-Si:H has led to several efforts to understand the defect creation in terms of metastable configurations of hydrogen atoms [18, 19]. The idea is that illumination provides the energy required to shift hydrogen atoms away from their dilute-phase sites, thus creating dangling bonds. The technological importance of establishing the atomic mechanism underlying the Staebler–Wronski effect lies in the possibility that this effect can be mitigated in a-Si:H by changing its preparation conditions.

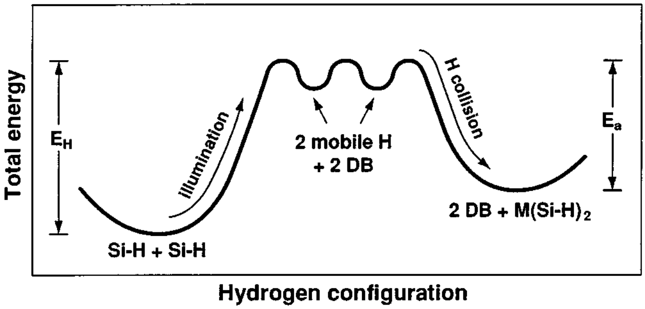

Figure 1.6: Configuration-coordinate diagram of the Staebler- Wronski DB creation reaction. Leftmost and rightmost wells are the stable and metastable states, respectively. Only two of many degenerate intermediate states with mobile H are represented by the central wells. Hydrogen diffusion (E_H) and metastability annealing (Ea) energies are indicated. [19]

An essential feature of the light-soaking effects on a-Si:H cells and films is that most of the effects are "metastable" and can be removed nearly completely by annealing of a light-soaked sample at a temperature above 150°C. It is important to note that S-W is not an impurity effect: the SW effect is intrinsic to the network of Si and H atoms. Branz proposed an 'hydrogen collision'' model [19]. In this model recombination-induced emission of H from Si-H bonds creates both mobile H in transport and DB's. The newly created DB's become metastable when the mobile H collide to form metastable complexes containing two Si-H bonds (see Fig 1.6)

1.3.4 Electronic Density-of-states

The most important concept used in understanding the optical and electronic properties of semiconductors is the electronic density-of-states, g(E). The idea is a simple approximation: if a single electron is added to a solid, it may be viewed as occupying a well-defined state (or molecular "orbital") at a particular energy level E. In a range of energies ΔE, the number of such states per unit volume of the solid is g(E)ΔE. In Figure1.7 we have illustrated the density-of-states for hydrogenated amorphous silicon as it has emerged primarily from measurements of electron photoemission [20, 21], optical absorption [22], and electron and hole drift mobilities [23]. In the dark at low temperatures, the states with energies below the Fermi energy E_F are filled by electrons; above the Fermi energy the states are empty. There are two strong bands of states illustrated: an occupied valence band (E $< E_V$), originating with the Si–Si and Si–H bonding orbitals and an unoccupied conduction band (E $> E_C$), originating with "antibonding" orbitals.

Between the conduction and valence bands lies an "energy gap" where the density-of- states is very low. Any functional semiconductor, crystalline or non-crystalline, must have such an energy gap. For perfect crystals, the valence and conduction bandedge energies E_V and E_C are well defined, as is the band gap $E_G = E_C{-}E_V$. Interestingly, in disordered semiconductors there are exponential distributions of bandtail states near these bandedges. For the valence bandtail, we write $g(E) = g_V exp[-(E{-}E_V)/\Delta E_V]$. The width ΔE_V of this exponential distribution is important in interpreting optical absorption experiments, in which it is usually identified with the exponential "Urbach" tail of the spectrum. For a-Si:H, a typical value Δ_{EV} =50 $\times$ 10^{-3} eV. Δ_{EV} is also used to account for the very slow drift of holes in an electric field (i.e. the hole drift mobility) [23, 24]. The conduction bandtail width ΔE_C is much narrower; for the best a-Si:H materials, it is about 22×10^{-3} eV, but increases markedly for amorphous silicon-germanium alloys [25]. Given the presence of exponential bandtails, the very existence of bandedge energy can reasonably be questioned. Remarkably, detailed analysis of drift-mobility measurements supports the concept of a well-defined bandedge [23, 26]. Most workers consider the bandedge to be the energy that separates

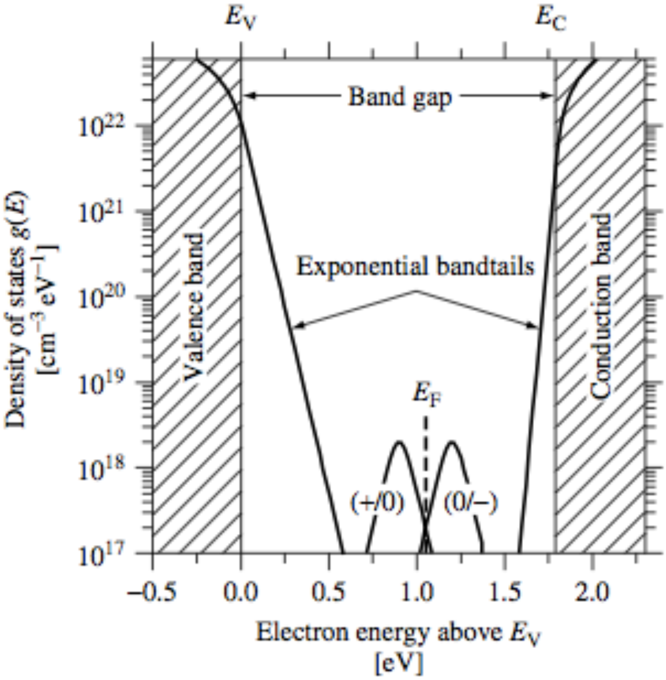

Figure 1.7: Density of electronic states g(E) in hydrogenated amorphous silicon. The shaded areas indicate delocalized states in the bands; these bands themselves have tails of localized states with an exponential distribution. Midway between the bands are levels belonging to gross defects such as dangling Si bonds indicated by the two peaked bands aroundE_F[7]

electron orbitals that are localized (i.e. have well-defined locations in space) from orbitals that are delocalized. The bandedges are correspondingly termed the conduction and valence band mobility edges [27]. Unfortunately, for noncrystalline semiconductors there is no single, conclusively established procedure for locating the bandedges within the density-of-states. The band gap is thus difficult to determine without some ambiguity. Since amorphous silicon–based materials with varying band gaps are used in solar cells, it is nonetheless very important to establish conventional procedures for comparing band gap.[7]

1.3.5 Absorption coefficient

Another importan feature of a-Si:H materials is the absorption coefficient. Figure 1.8 shows the optical absorption coefficient α as a function of the photon energy $h\nu$, as obtained for three different materials: (1) monocrystalline silicon wafers (c-Si); (2) typical a-Si:H layers deposited by PECVD; (3) typical high-quality mc-Si:H layers deposited by PECVD. The vertical axis of Figure 1.8 is also calibrated in penetration depth $d\lambda$, i.e., layer thickness within which (1-1/e)=63% of the corresponding photons are absorbed. Note here that the visible range of the light spectrum extends from about 1.7 to 3.2 eV and that the 'useful' range of the AM 1.5 solar spectrum containing some 85% of the total incident energy extends from about 1.0 to 4.0eV.[1] Silicon being a material with an indirect band gap, the absorption process can take place only if a phonon intervenes, and, therefore, the absorption coefficient in all forms of crystalline silicon (c-Si and mc-Si:H) is relatively low. In a-Si:H it is, at least for photon energies >2 eV, somewhat higher, because the structural disorder present in an amorphous material 'relaxes' the quantum mechanical selection rules; even so it remains considerably lower than in thin-film semiconductors with a direct bandgap, such as CdTe. Because of this fact, penetration depths $d\lambda$, in both forms of thin-film silicon are relatively large, especially for the infrared and red part of the solar spectrum. This, essentially means that it is not very reasonable to design thin-film silicon solar cells without efficient light trapping, which is usually obtained with rough contact layers.

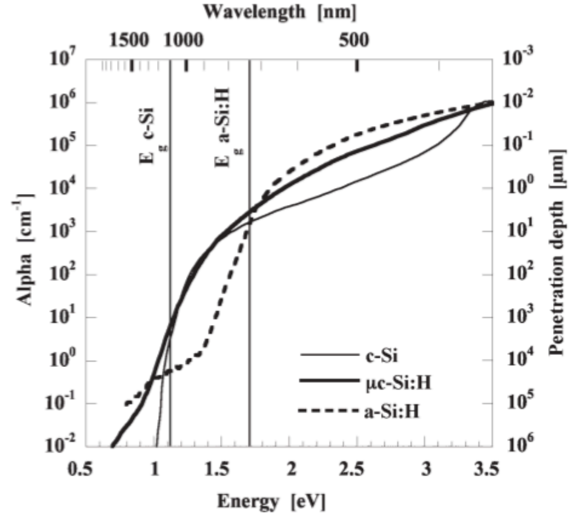

Figure 1.8: Curves for the optical absorption coefficient α and the penetration depth dλ of monochromatic light with photon energy hν and wavelength λ, for wafer-type crystalline silicon (c-Si) and typical device-quality a-Si:H and mc-Si:H layers on glass.15,16 The curve for mc-Si:H has been corrected for light scattering due to surface roughness(16)[15]

1.4 Pin structure

The fundamental photodiode inside an amorphous silicon–based solar cell has three layers deposited in either the p-i-n or the n-i-p sequence. It is, however, not advisable to use p–n-type diodes as solar cell structure, in the case of amorphous silicon, drift assisted collection is necessary for three reasons: the doping capability of a-Si:H is rather poor, the Fermi-level can be pushed only half way towards the conduction and valence band edges, even with heavy doping. Doping has a detrimental effect on a-Si:H layer quality, because it leads to the creation of many additional silicon dangling bonds, which are the main recombination centres in this material. In a classical p–n-type solar cell, carrier collection is obtained by minority carrier diffusion within the p- and n-layers. Luckily, diffusion lengths in crystalline silicon wafers are sufficiently high (over 200 μm), to ensure a near-perfect carrier collection over the whole useful range of the solar cell thickness where significant optical absorption takes place. In a-Si:H layers, on the other hand, minority carrier diffusion lengths are extremely small (around 0.1 um), and it becomes impossible to base the collection of photogenerated carriers on diffusion

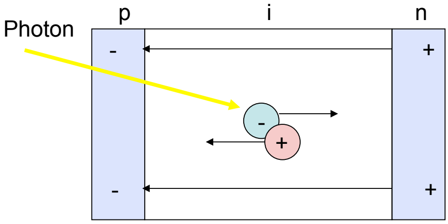

Figure 1.9: pin photodiode, in which excess electrons are donated from the n-type p-type layers, leaving the charges and electric field illustrated.Each photon absorbed in the undoped, intrinsic layer generates an electron and a hole photocarrier. The electric field causes these carriers to drift in the directions shown

alone.

Because of these three reasons p–i–n diodes are always used for a-Si:H solar cells. For doped a-Si:H, it turns out that minority photocarriers (holes in n-type a-Si:H, electrons in p-type a-Si:H) do not move very far, and so a p-n structure would only collect photocarriers from photons generated in an extremely thin layer of doped a-Si:H. Indeed, in analyzing the performance of a-Si:H-based solar cells, one normally considers any photons absorbed by the doped layers to be "wasted." The trick of keeping the doping atoms out of the absorber layer enables this layer to be thick enough to capture most of the sunlight. [7]

The three layers are a very thin (typically 20 nm) p-type layer, a much thicker (typically a few hundred nanometer), undoped intrinsic (i) layer, and a very thin n-type layer. As illustrated in Figure,1.9 in this structure excess electrons are actually donated from the n-type layer to the p-type layer, leaving the layers positively and negatively charged (respectively), and creating a sizable "built-in" electric field. Sunlight enters the photodiode as a stream of photons that pass through the p-type layer, which is a nearly transparent "window" layer. The solar photons are mostly absorbed in the much thicker intrinsic layer; each photon that is absorbed will generate one electron and one hole photocarrier [28] The photocarriers are swept away by the built-in electric field to the n-type and p-type layers, respectively – thus generating solar electricity. The p–i–n-type a-Si:H solar cell was introduced by D. Carlson et al. at RCA Laboratories, Princeton, New Jersey, USA.

1.4.1 Substrate and superstrate

One of the advantages of amorphous silicon–based solar cells is that they absorb sunlight very efficiently: the total thickness of the absorbing layers in amorphous silicon solar cells is less than 1 μm. Consequently, these layers need to be supported on a much thicker substrate. Two totally different designs for amorphous silicon solar cells have evolved corresponding to transparent and opaque substrates respectively superstrate and substrate design. In the "superstrate" design, sunlight enters through the transparent substrate, which is usually glass or a transparent plastic. The insulating substrate needs a conducting layer, which is typically a "transparent conductive oxide" (TCO). The amorphous silicon photodiode layers are then deposited onto the TCO, starting with a p-type window layer. In the "substrate" design, sunlight enters the photodiode before it reaches the substrate. Starting with the substrate, the cell is fabricated in the reverse order compared to the superstrate design: first a back reflector, then the photodiode layers (starting with an n-type layer), and finally a TCO layer to act as an electrode to the topmost, window layer of the photodiode. These two designs permit a very wide range of applications for amorphous silicon solar cells. The superstrate design (light enters through the substrate) is particularly suited to building-integrated solar cells in which a glass substrate can be used as an architectural element. The substrate design has generally been applied to solar cells using flexible, stainless steel substrates. [7]

1.4.2 Multiple-Junction solar cells

Amorphous silicon solar cells can be fabricated in a stacked structure to form multijunction solar cells, with two or three junctions grown one upon the other and current matched. This strategy is particularly successful for amorphous materials, both because there is no need for lattice matching, as is required for crystalline heterojunctions, and also because the band gap is readily adjusted by alloying.

Multijunction, a-Si-based solar cells can be fabricated with higher solar conversion efficiency than single-junction cells and are presently used in most commercial cells. the highest reported triple juction a-Si/a-Si/a-SiGe cell is 12.1% in standard contitions .[29]

1.5 Results and discussion

To optimize the electrical characteristics of the solar cells and to avoid as much as possible energy losses due to insufficient light absorption and excessive photocarrier recombination for absorption and for recombination, the realization of a standard solar cell with single junction configuration has started with a systematic electrical and optical study of the materials that compose the pin diode. The electrical properties of the layer have been primarily controlled through by sheet resistance measurements, that in turn are related to the specific resistivity and the film thickness d i.e. $R_{Sh} = \rho/d$. We extracted the resistivity activation energy of

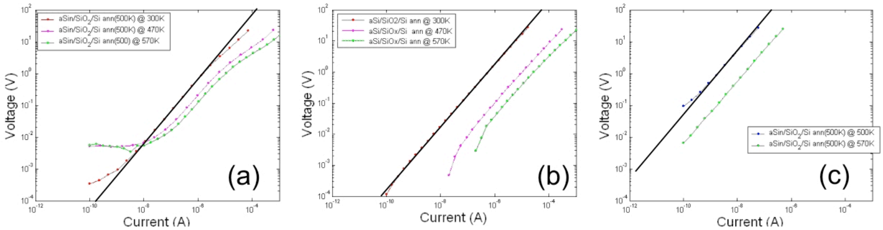

Figure 1.10: IV characteristic of n doped (a) p doped (b) and intrinsic (c) layer, at 300K (red line),470K(Magenta line),570K (green line), for the intrinsic layer it was not possible measure the IV characteristic at Temperature lower than 500 K(blue line).

the p-type, n-type, and undoped a-Si:H material, using the four probe in line methodology. The sheet resistance Rsh of the samples evolves as a function of the temperature T according to

$$R_{Sh} = R_0 exp(E_A/kT)$$

Where R_0 is the extrapolated value of resistance at infinite temperature, k is the Boltzmann constant, and T the absolute temperature. To extract the sheet resistance and for the IV characteristics of the a-Si:H material ad hoc samples were realized. In particular, 1000, 30, 20, 10 and 5 nm thick p- type a-Si:H films were deposited on three types of substrates: CVD SiO_2 covered Corning glass, CVD SiO_2 covered Si substrates, and Si substrates thermally oxidized with 900 nm SiO_2 grown in wet ambient. Among the three types of substrates the final choice was the Si substrate with thermal oxide. This had the advantages of providing no additional conductive path except for the a-Si film under test, and of providing a very high quality thermal contact to the underlying thermostatic stage used as sample holder during the resistance vs. temperature measurements.

In Fig 1.10 it is shown the 4-point probe IV characteristicsof n doped (a) p doped (b) and intrinsic (c) layers, at room temperature (red lines), 470 K (magenta lines) and 570 K (green lines). The thickness of the layers was 1μm. As we can see the sheet resistance decreases as the Temperature increases. It was not possible to measure the IV at room temperature for the i layer because the sheet resistance is too high to be measured using our equipment. The black line highlights the linear trend of the IV curve, and indicates the ideal linear trend behavior of the sample at every temperature. This analysis has allowed us to define the forced current conditions in which the IV characteristics are closer to linearity, and such levels have been used to measure the sheet resistance as a function of temperature.

We extracted the $R_{sh}$of the p-type, n-type and undoped a-Si:H materials, the results are shown in Figure1.11 . We have analyzed several samples with thickness

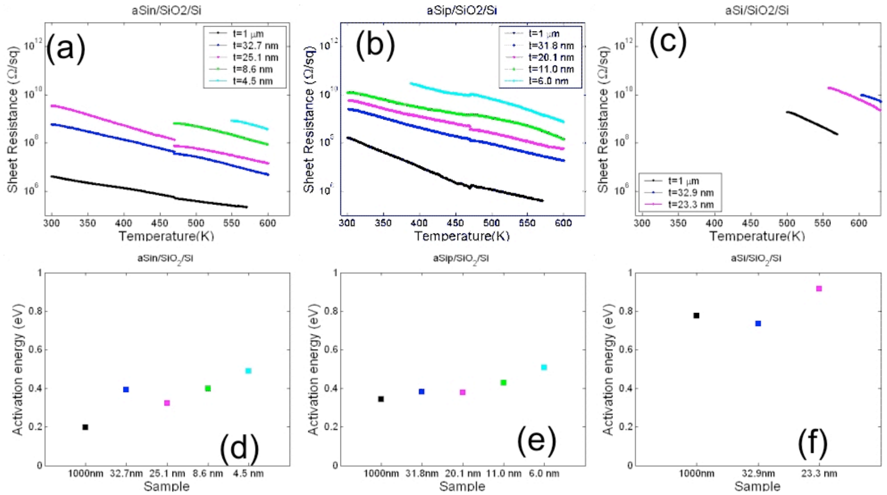

Figure 1.11: Sheet resistance of n-doped (a), p-doped (b), and intrinsic amorphous layer as a function of temperature, measured with a constant heating rates (dT/dt) of 15 K/min. The inset shows the thickness of each layer.

varying from 5 nm to 1000 nm. Fig.s 1.11 (a-b-c) show the sheet resistance of several amorphous layer as a function of temperature, measured with a constant heating rates (dT/dt) of 15 K/min; the inset shows the thickness of each layer. As we can see in these figures the resistance decreases with the temperature increases. The activation energies (E_a) of the same samples are reported in the figs 1.11 (d-e-f). As it is possible to see, E_a increases as the layer thickness decreases.

The same type of behaviour is also seen as the sheet resistance is rescaled as resistivity, i.e., by dividing the sheet resistance for the sample thickness (Fig. 1.12). In such case, as the sample thickness decreases, the apparent sample resistivity increases, though the materials are all prepared under the same ratios of$SiH_4$to H_2 and TMB of PH_3. That is, as thickness decreases a dopant de-activation effect is observed. This may be due to surface states trapping the free carriers or some chemical and / or structural change. We have not further analyzed this effect, but based on this experience we have decided to reduce as much as possible the thickness of the p and n type layer for the pin PV cell fabrication, but without going below 10 nm thickness, to avoid excessive doping de-activation effects.

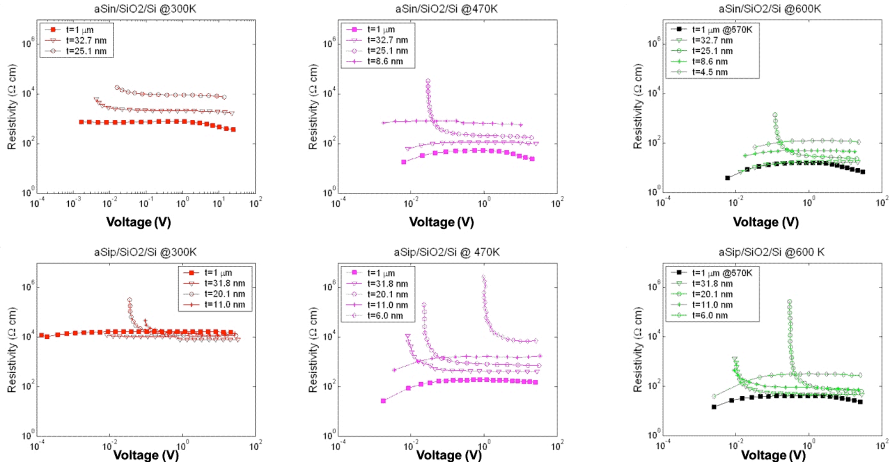

Figure 1.12: Sheet resistance of n-doped (a-b-c) and p-doped (d-e-f) amorphous layer, measured with constant temperature reported of 300K (a, d), 470K (b, e) and 600K (c, f). The inset shows the thickness of each layer.

1.5.1 Absorption coefficient

Another crucial feature, for the realization of a PV cell, is the absorption coefficient of the aSi:H layers. To extract the absorption coefficient of the a-Si:H material ad hoc samples were realized. In particular,films of 1000 nm thickness of p- type, n type and undoped a-Si:H were deposited on quartz substrates covered with a deposited 900 nm SiO_2 layer. The choice of quartz was made because for this kind of analysis there is the necessity to use a transparent substrate. In Fig 1.13 it is shown the result of Absorption coefficient for the analyzed samples.

Experimental data are in good agreement with literature results (Refs). We also note a slight dependence of the absorption coefficient on the doping. The p-type materials show a larger absorption compared to intrinsic a-Si:H, which in turn, is more absorbing than the n-type material.

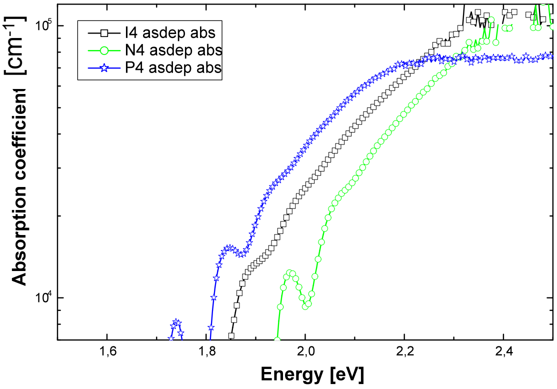

Figure 1.13: Curves for the optical absorption coefficient as a function of Energy, for p-doped (blue line), intrinsic (black line), and n-doped (green line) amorphous silicon layer. (courtesy of dott. Salvo Mirabella)

On the basis of the above described electrical and optical data, we had sufficient information to design the pin a-Si:H structures, in order to optimize light absorption.

1.5.2 Cell design

The first issue we have investigated is the impact of the top window layer. In fig 1.14(a) it is shown the simulation of the absorbed power of a PIN diode with 1 um of absorber (intrinsic layer) and by varying the top contact thickness from 10 to 40 nm. The black curve shows the AM 1.5 G incident spectrum. The p-layer plays an important role, as shown in fig 1.14 a. Indeed, as the p-type contact thickness increases, a non negligible part of the incident radiation is lost in absorption of the top layer. The simulation highlights that if the thickness decreases from 40 nm to 10 nm , a gain of 100 W/m^2 over an average value of about 300 W/m^2 is obtained. Hence the overall gain of energy is 1/3 more passing from 40 nm to 10 nm.

The other crucial parameter for the absorption of the incident radiation is obviously the thickness of the absorber layer.

Another important contribute in the absorbed power is surely the active layer thickness. Figure 1.14(b) shows the simulation of the absorbed power using a 20 nm of window layer thickness and by varying the absorber layer thickness. The figure shows shows that if the thickness decreases from 1000 nm to 250 nm in the pin diode under AM 1.5 G illumination (black curve) 80 W/m^2 are lost on an

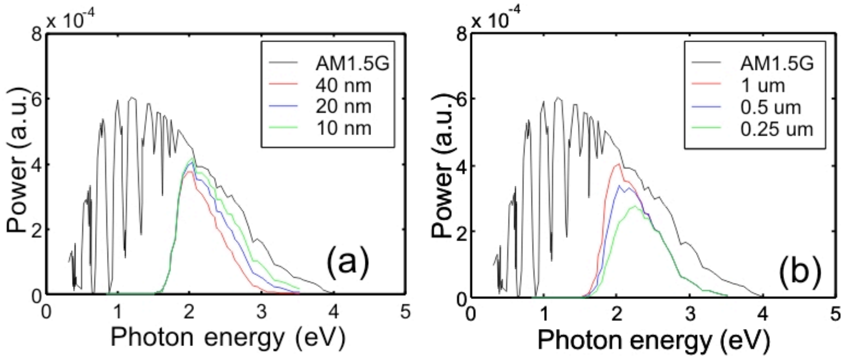

Figure 1.14: Simulations of the absorbed power of a PIN diode (a)with 1 um of absorber (intrinsic layer) and by varying the top contact thickness from 10 to 40 nm and (b) using a 20 nm of window layer thickness and by varying the absorber layer thickness The black curve shows the AM 1.5 G incident spectrum.

average power density of about 260 W/m^2. Hence the overall loss of energy is 1/3 more passing from 1um to 250 nm

We have also analyzed the impact of common defects on the overall performance of the pin PV cell. For this purpose we have used the simulation software package ATLAS of SILVACO. In particular ATLAS allows to solve the coupled drift-diffusion and Poisson equations in the pin device. The a-Si:H layer is assumed to be a low mobility semiconductor with a large density of defects at the band edges and at mid-gap, the latter in particular attributed to dangling bonds, the D-centers. Table 1 shows the list of parameters and respective values used in our simulations.

Fig. 1.15 shows the impact of D-centers on the PV cell performances. The pin stack is assumed to be of 20 nm / 250 nm / 20 nm thicknesses of the p, intrinsic, and n layer, respectively. When the density of mid-gap D-centers is low (10^{15} $/cm^3$), the cell short circuit current reaches its maximum (about 7 mA/cm^2), corresponding to negligible photocarrier recombination, with a concomitant value of power conversion efficiency of about 4.5 %. Note that this value is in the case of a structure with no anti-reflection coating and negligible light trapping (no texturization), but with the assumption of perfect ohmic contact. A more realistic evaluation of the maximum achievable power conversion efficiency should take into accout light trapping, ARC layers, and real (non ohmic) contacts. But we can consider these values realistic upper boundaries for our devices, given that we did not use ARC layers and we did not optimize TCO texturization. The simulation shows that as the D-center concentration increases above about $10^{17}/cm^3$ the carrier recombination becomes important, so that JSC decreases and the overall cell efficiency declines. In other words, the recombination becomes an important effect as the defect concentration exceeds the few part per million (ppms).

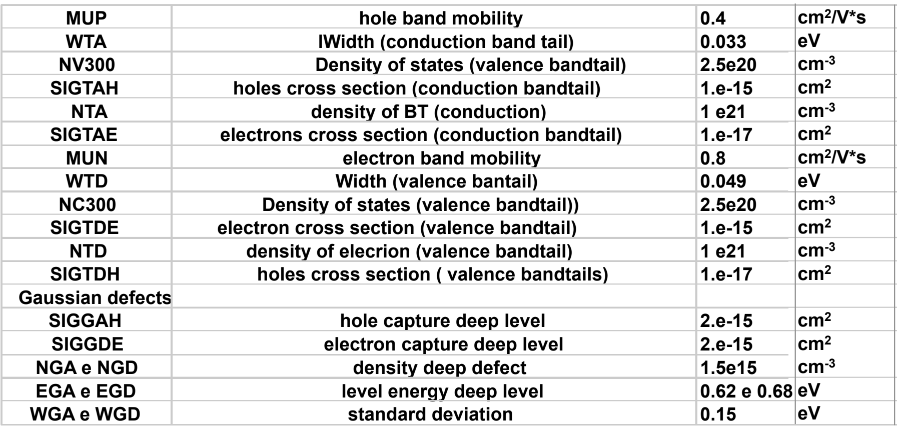

MUP	hole band mobility	0.4	$cm^2/V*s$
WTA	lWidth (conduction band tail)	0.033	eV
NV300	Density of states (valence bandtail)	2.5e20	cm^{-3}
SIGTAH	holes cross section (conduction bandtail)	1.e-15	cm^2
NTA	density of BT (conduction)	1 e21	cm^{-3}
SIGTAE	electrons cross section (conduction bandtail)	1.e-17	cm^2
MUN	electron band mobility	0.8	$cm^2/V*s$
WTD	Width (valence bantail)	0.049	eV
NC300	Density of states (valence bandtail))	2.5e20	cm^{-3}
SIGTDE	electron cross section (valence bandtail)	1.e-15	cm^2
NTD	density of elecrion (valence bandtail)	1 e21	cm^{-3}
SIGTDH	holes cross section (valence bandtails)	1.e-17	cm^2
Gaussian defects			
SIGGAH	hole capture deep level	2.e-15	cm^2
SIGGDE	electron capture deep level	2.e-15	cm^2
NGA e NGD	density deep defect	1.5e15	cm^{-3}
EGA e EGD	level energy deep level	0.62 e 0.68	eV
WGA e WGD	standard deviation	0.15	eV

Table 1.1: list of parameters and respective values used in our simulations.

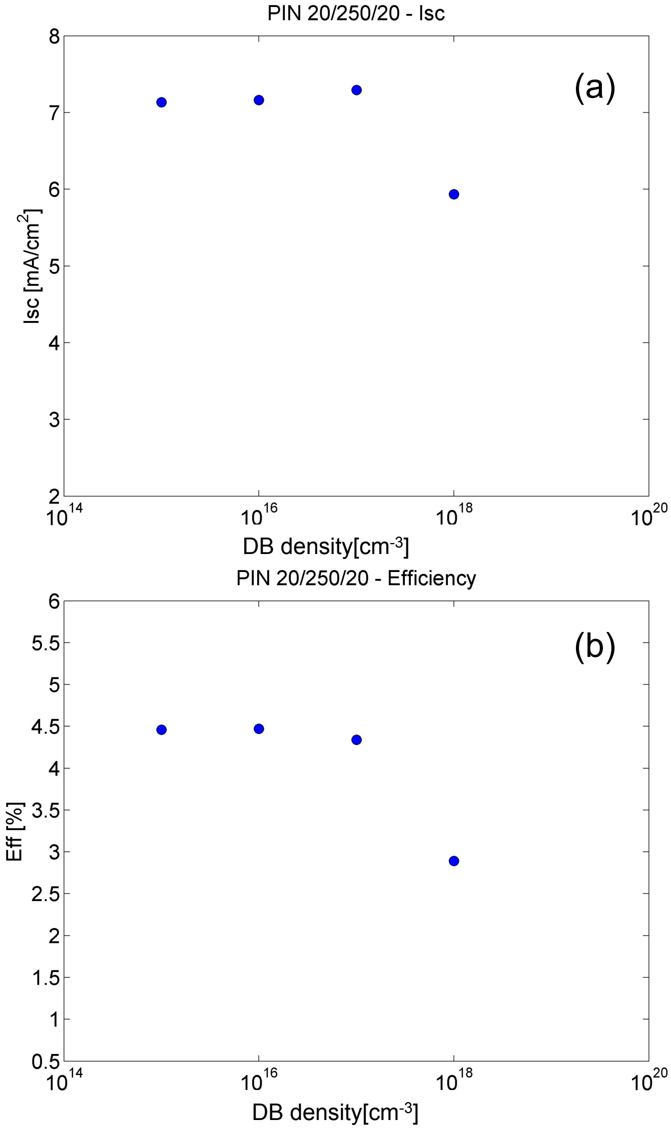

Figure 1.15: Simularion of the impact of D-centers on the PV cell performance. (Courtesy of Dott. Cannella).

1.5.3 Pin diode measures

After an intensive and accurate study of the main property of amorphous layer, the pin diodes were realized with different stack sequences, as reported in the table of figure 1.16.

P-doped, n-doped and undoped films that compose the pin diodes, were prepared by PECVD of a gas mixture of silane (SiH_4) and hydrogen (H_2), these layers are deposited at 280 °C, with pressure of about 2.4mbar on the ASAHI glass substrate covered with transparent conductive oxide, which is used as conducting layer. To determine the role of the hydrogen in the electical characteristics of the deposited films undoped layers are deposited by using an hydrogen diluition ratio, defined as R= F_{H2}/ F_{SiH4}, where$F_{SiH4} = 100sccm$ is silane flow rate and F_{H2} is Hydrogen flow rate was varied between 1-10.

The pin diode were realized using the superstrate configuration (See section 1.4.1) , the corresponding structure is shown schematically in figure 1.16.From bottom to top it is possible see the layer sequence, the ASAHI glass, the transparent conductive oxide, which is used as conducting layer, and the pin diode sequence, the window layer(p), the active layer (i) and the n-doped layer. After that there is another layer of TCO, and in particular of Al doped ZnO, refererred to in the following as AZO, which acts as a top electrode.

In summary, the analysis of the I-V characteristics leads us to conclude that the best intrinsic layer thickness for our deposition conditions is equal to 250 nm.

Certainly, starting from basic physical characteristics of the layers we were able to realize sufficiently good PV cells of amorphous Si, though further optimization is certainly possible, by introducing ARC layers, optimizing light trapping, etc.In the next paragraph, by using as test vehicle our best structure, that is, the 20 nm / 250 nm / 20 nm pin stack, we study the effect of the transition from amorphous to nanocrystalline Si.

To realize the test PV cells, standard lithography has been then used to define on the wafers circular areas with diameters ranging from 100 to 6400 um.

1.5.3.1 IV characteristic

The dark current density/voltage characteristics of several pin diodes in dark conditionare shown in Fig. 1.17. The samples were made by using the same thickness for the p and n contacts (20 nm), while the absorber thickness was varied from 125 nm to 1 μm, these are deposited with hydrogen diluition R=2. We observe that the current scales perfectly with the device area, as demonstrated by the almost perfect coincidence of the J-V characteristics as the device diameter is changed from 200 μm up to 6400 μm. This indicates that our devices have negligible shunts and perimeter leakages.The results demonstrate that the current density depends strongly on the thickness of the intrinsic layer. As it is possible to see in

Thickness (nm)			
	p	i	n
a-Si:H pin	20	1000	20
	20	500	20
	20	250	20
	20	125	20

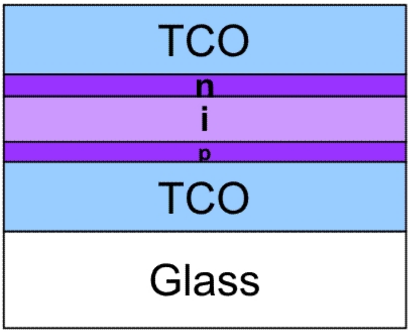

Figure 1.16: The table reported the thickness of the analyzed diode. Schematic sketch of the realized p-i-n thin film solar cell.

fig 1.17a it is not possible to realize a pin cell using 1 µm of intrinsic layer, because it is present a strong contribution of recombination. We essentially have almost an open circuit: conductivity is so low that almost no current is detected at low voltage. By decreasing the active layer thickness, the diode starts to work. The best condition is represented by the sample with the active layer thickness of 250 nm (fig 1.17 c), since if we still decrease the intrinsic layer thickness down to 125 nm, the diode electrical behavior deteriorates again.The reasons for this behavior are unclear: we speculate that at large intrinsic layer thickness the electric field produced by the carrier depletion at the p/i and n/i boundaries is insufficient to get a reasonable carrier mobility, so that almost no current is transported. As the intrinsic layer thickness decreases, the electric field increases in proportion, and carrier mobility becomes large enough. As the intrinsic layer thickness becomes very low, the weight of the carrier recombination at the p/i and n/i interfaces becomes important, so that the I-V curves degrade again.

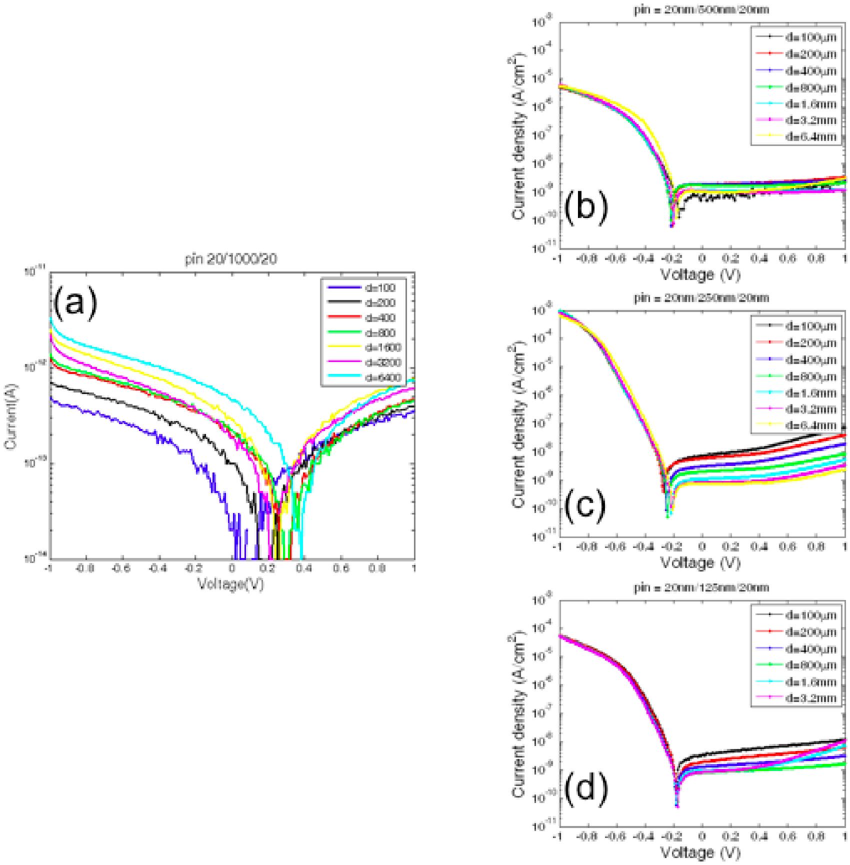

Figure 1.17: Current voltage (a) and current density voltage (b-d) characteristics of several Pin diodes, analyzed in dark condition. The sample was made by varying the thickness of the absorber layer from 1 μm to 125 nm. The diameters of the analyzing diode are showed in the inset.

1.5.4 Nc-Si:H solar cell: electrical characterization

To examine the effect of intrinsic nc-Si absorber layers prepared with different silane concentration on the solar cells performance a series pin devices has been prepared, the p/i/n thickness are respectively 20/250/20 nm. Fig 1.18 shows the comparison of the characteristics as the R parameter increases from 1 to 10. The open circuit voltage (Voc) shows a decrease as R increases(Fig 1.18Va-Vd).

This can be understood when considering that the increase of R implies some crystallization of the a-Si material. This implies a lower gap material, and therefore a decrease of Voc. As far as the short circuit current (Jsc) is concerned, we observe a trend with an initial increase followed by a decrease (fig1.18Ja-Jd). This type of behavior has already been observed in literature (Refs Vettel) and it can be understood by considering the above mentioned crystallization effect. In particular, as R increases, starting from a purely a-Si film the increase in the H content probably improves the D center passivation, reducing recombination and improving the Jsc. This improvement takes place up to a critical R, over which crystallization takes place. Crystallization implies a reduction of the absorption coefficient in the visible region, well known in literature, and therefore a decrease in Jsc. Overall this behaviour implies a maximum power conversion efficiency, which for our preparation conditions takes place for an R value of about 2.

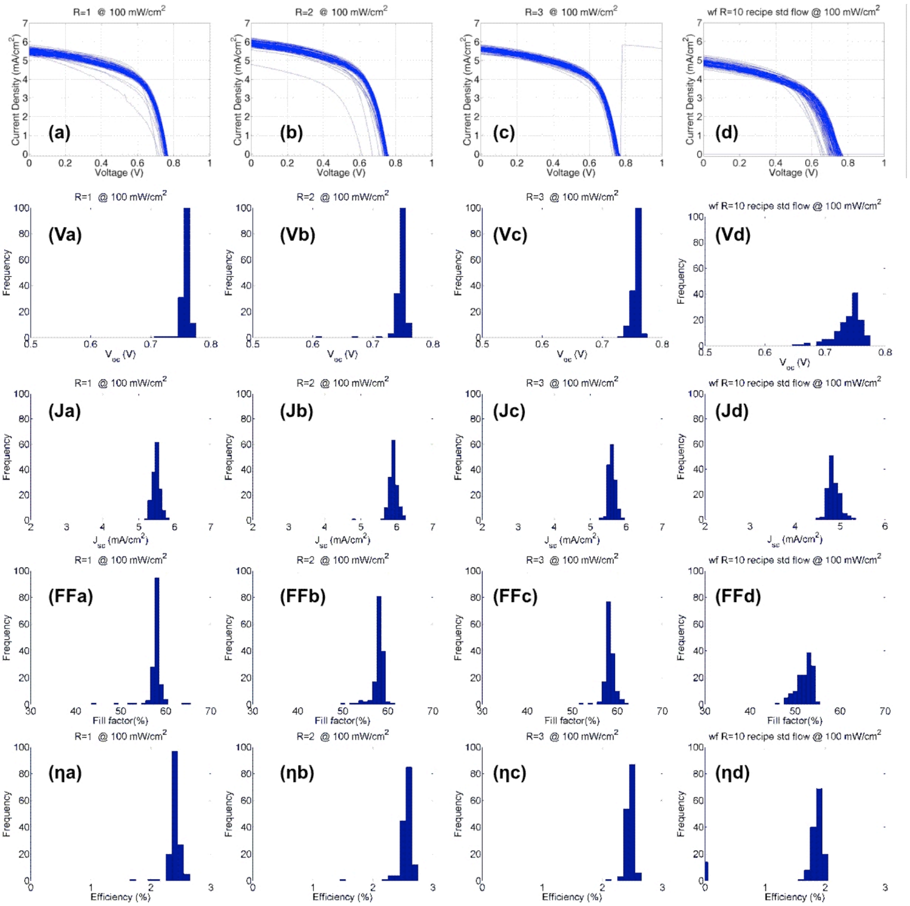

Figure 1.18: Courtesy Dott.ssa M. Foti (ST)

1.6 Conclusions

Amorphous and nanocrystalline silicon prepared by PECVD have been investigated as active materials for thin film solar cells. The realization of a pin solar cell was shown, including the investigation of the key physical properties necessary to design the solar cell (sheet resistance, activation energies for conductivity, light absorption). The electrical characterizations of the solar cells in dark condition and under standard illumination were shown. Results in terms of electical performance are close to the modeling estimates. As important result the deposition conditions near the transition from amorphous to nanocrystalline Si growth have been found to be most beneficial to the solar cell properties. A further decrease of Hydrogen dilution, R, results in some decrease of short-circuit current I_{SC} and Fill factor FF, probably caused by amorphous growth and D-center de-passivation. On the other hand, an increase of R also reduces FF and J_{SC} and results in lower V_{OC} values likely attributed to the transition to nanocrystalline Si, which decreases band-gap and light absorption. There is, therefore, a maximum of J_{SC} ad FF which results in the best performances. These, however are roughly about 20% and 45% lower compared to the model estimates for J_{SC} and power conversion efficiency respectively. We attribute this to a too high concentration of D centers, estimated to be of the order of $1 \times 10^{18}/cm^3$and also to the presence of non perfectly ohmic contacts, contrarily to the assumption of the simulation.In the next chapter the structural composition of the hydrogenated amorphous silicon layers and hydrogenated nanocrystalline layers will be discussed.

References

[1] A. V. Shah, H. Schade, M. Vanecek, J. Meier, E. Vallat-Sauvain, N. Wyrsch, U. Kroll, C. Droz and J. Bailat. Prog. Photovolt: Res. Appl. (2004); 12:113–142

[2] O. Vetterl, F. Finger, R. Carius, P. Hapke, L. Houben, O. Kluth, A. Lambertz, A. MuK ck, B. Rech, H. Wagner.Solar Energy Materials & Solar Cells 62 (2000) 97-108

[3] J. Meier, H. Keppner, S. Dubail, Y. Ziegler, L. Feitknecht, P Torres, Ch. Hof, U. Kroll, D. Fischer, J. Cuperus, J.A. Anna Selvan, A. Shah, in: J. Schmid, H.A. Ossenbrink, P. Helm, H. Ehmann, E.D. Dunlop (Eds.), Proceedings of the 2nd World Conference on Photovoltaic and Solar Energy Conversion, European Comission, Ispra, Italy, 1998, p. 375.

[4] K.Yamamoto,M.Yoshimi,T.Suzuki,Y.Tawada,T.Okamoto,A.Nakajima,Mater.Res.Soc.Sy
Proc. 507 (1998) 131.

[5] K. Saito, M. Sano, K. Matuda, T. Kondo, T. Nishimoto, K. Ogawa, I Kajita, in: J. Schmid, H.A. Ossenbrink, P. Helm, H. Ehmann, E.D. Dunlop (Eds.), Proceedings of the Second World Conference on Photovoltaic and Solar Energy Conversion, European Comission, Ispra, Italy, 1998, p. 351.

[6] O. Vetterl, P. Hapke, O. Kluth, A. Lambertz, S. Wieder, B. Rech, F. Finger, H. Wagner, Solid State Phen. 67}68 (1999) 101.

[7] Handbook of Photovoltaic Science and Engineering. Ed Wiley

[8] Lofersky J, Postepy-Fizkyi 26, 535–560 (1975).

[9] Meier J, Spitznagel J, Kroll U, Bucher C, Fay¨ S, Moriarty T, Shah Proceedings of the 3rd World Conference on PVSEC, Osaka, 2003;

[10] Meier J, Keppner H, Dubail S, Kroll U, Torres P, Pernet P, Ziegler Y, Anna Selvan JA, Cuperus J, Fischer D, Shah Proceedings of the Materials Research Society Symposium 1998; 507: 139–144.

[11] Meier J, Spitznagel J, Fay¨ S, Bucher C, Graf U, Kroll U, Dubail S, Shah A. Enhanced light-trapping for micromorph tandem solar cells by LP-CVD ZnO. Proceedings of the 29th IEEE Photovoltaic Specialists Conference, New Orleans, 2002; 1118–1121.

[12] Reimer J, Petrich M, in Fritzsche H, Ed, Amorphous Silicon and Related Materials, Vol. A, 3–27, World Scientific, Singapore (1989).

[13] Figure courtesy of R. Biswas; for information on the calculations, see Biswas R, Li Y, Phys. Rev. Lett. 82, 2512 (1999).

[14] The assignment of the D-center observed in electron paramagnetic resonance measurements with a dangling bond has been challenged in favor of "floating bonds" (Stathis J, Pantelides S, Phys. Rev. B 37, 6579–6582 (1988)).

[15] Street R, Hydrogenated Amorphous Silicon, Cambridge University Press, Cambridge (1991).

[16] Jackson W, Tsai C, Thompson R, Phys. Rev. Lett. 64, 56 (1990).

[17] Zafar S, Schiff E, Phys. Rev. Lett. 66, 1493 (1991).

[18] Fritzsche H, Annu. Rev. Mater. Res. 31, 47 (2001).

[19] Branz H, Phys. Rev. B 59, 5498 (1999).

[20] Ley L, J. Non-Cryst. Solids 114, 238 (1989).

[21] Jackson W, Kelso S, Tsai C, Allen J, Oh S, Phys. Rev. B 31, 5187 (1985).

[22] Cody G, Tiedje T, Abeles B, Brooks B, Goldstein Y, Phys. Rev. Lett. 47, 1480 (1981).

[23] Tiedje T, in Joannopoulos J, Lucovsky G, Eds, Hydrogenated Amorphous Silicon II , 261–300, Springer-Verlag, New York (1984).

[24] Gu Q, Wang Q, Schiff E, Li Y, Malone C, J. Appl. Phys. 76, 2310 (1994).

[25] Wang Q, Antoniadis H, Schiff E, Guha S, Phys. Rev. B 47, 9435 (1993).

[26] Gu Q, Schiff E, Chevrier J, Equer B, Phys. Rev. B 52, 5695 (1995)

[27] Mott N, Conduction in Non-Crystalline Solids, Oxford University Press, Oxford (1987)

[28] Schiff E, J. Non-Cryst. Solids 190, 1 (1995).

[29] J. Yong, A. bonerjee, S. suguyama, S. guha, IEEE PV Spc conf 1998 p.563

Chapter 2

Hydrogen role in the phase transition from amorphous to nanocrystalline silicon films

2.1 Introduction

During the last three decades, hydrogenated amorphous silicon has been studied extensively as base material for thin film solar cells due to the natural abundance of source material, environmental safety, potential high performance and the capability of the cost production. However, the defect density of hydrogenated amorphous silicon (a-Si:H) increase with light exposure, causing an increase in the recombination current and leading to reduction in the device conversion efficiency. This phenomenon is known as Staebler-Wronski effect [1]. For this reason, the solar cells based on a-Si:H have always been associated with efficiency losses [2]. Extensive research has been carried out by many laboratories to improve the stability in conversion efficiency of a-Si:H solar cells [3]. The attempts to overcome the Staebler-Wronski effect have focused primarily on either the solar cell device architecture [4, 5, 6], or modifications to the deposition process, so as to "harden" the material against metastable defect formation[5, 6, 7, 15, 9, 10]. A material that presents promising features is hydrogenated nanocrystalline silicon (nc-Si:H). Nc-Si:H films show better stability under light soaking, and thus have high potential as stable material for solar cells[15]. The parameter that could play a role in the stability under light soaking and also in the crystalline fraction is believed to be the hydrogen concentration and its complex bonding mechanism. The major technical challenge with such nanocrystalline solar cells is the fact that the surface area of grain boundaries is very high, and this significantly increases the density of recombination centers as well as the probability of recombination due to charge carriers. This indicates that the crystalline fraction and the grain size of these materials determine also the electrical properties of the final device. It is believed that the hydrogen content and its bonding behavior is the responsible for the structural characteristics and as a consequence for the stability under illumination. In general there are two methods used for the synthesis of nc-Si:H thin films, one is the re-crystallization of a-Si:H films and the other is direct deposition. The recrystallization technique includes rapid thermal annealing (RTA) [11], laser-melt re-crystallization (LMR) [12] and aluminum-induced crystallization [13]. However, these methods have difficulties in accurate control of crystallite size and crystalline fraction. In addition to these techniques, also post annealing at temperatures over 1000°C is used for the crystallization of Si nanoparticles. Such high annealing temperature inevitably limits its further applications in solar cells devices. On the other hand, a variety of direct chemical vapour deposition (CVD) techniques have been used to yield material with good opto-electronic properties. These include plasma enhanced CVD (PE-CVD) [14] and its variant, the very high frequency glow discharge (VHF-GD)[15]. Other CVD methods employed in the deposition of nc-Si:H are electron cyclotron resonance-CVD (ECR-CVD) [16], homo-CVD [17] and hot-wire CVD (HW-CVD) [18]. Among these, only PE-CVD has been established for industrial applications for its unique direct deposition mechanism and for its feasibility of improvement of film quality. In preparation of nc-Si:H films by PE-CVD method, various process parameters and dilution of the source gas silane (SiH_4) with other gases (Ar, H_2 or He) have a strong influence on the structure and morphology of the films. Some of the reports indicated that the nc-Si:H films deposited by PE-CVD do not show any systematic correlation between the process parameters and the resulting film properties [19] due to the heterogeneity of grown films. On the other hand, some reports [20] have shown that the crystallite size and height, as well as their density can be controlled by deposition time, process pressure, rf power and substrate temperature. After an accurate analysis of the main PV cells electrical characteristic that highlight the strong influence of hydrogen dilution of silane, as shown in the previous chapter, the work here is focused on the structural characterization, to better understand the role of hydrogen in the transition from hydrogenated amorphous silicon to hydrogenated nanocrystalline silicon layer.

2.2 Deposition characteristics (Experimental)

Undoped a-Si:H and nc-Si:H films were prepared by PECVD of a gas mixture of silane (SiH_4) and hydrogen (H_2). These films were deposited on Silicon substrates and after the deposition of a thin silicon dioxide layer (50 nm). Undoped layers are deposited at 280 °C, with pressure of about 2.4mbar, by using different silane flow rates, equal to 100 sccm in the first case and 12 sccm in the second case. The hydrogen diluition ratio, defined as R= F_{H2} / F_{SiH4}, where F_{SiH4} is silane flow rate and F_{H2} is Hydrogen flow rate was varied between 2-10 in the layers made with F_{SiH4}=100 sccm and it was varied between 10,40 in the other group of layers. To determine the role of the hydrogen in the structural characteristics of the deposited films we investigated them by using a transmission electron microscope (JEOL JEM 2010) in particular by using dark-field TEM imaging. Regions that satisfy the Bragg diffraction condition will appear bright in the dark-field images. Electron-transparent samples for TEM characterization are usually prepared by using procedures that require temperatures of about 150 °C. This thermal budget could crystallize the samples. To avoid this, a procedure at temperatures lower than 120 °C has been developed, and it has demonstrated not to induce the crystallization in these samples. The final step of the TEM specimen preparation require the ion-milling thinning. This method is known to amorphize thin surfacial portions of crystalline silicon. To avoid also this effect, the specimens have been finished by using low energy ion-milling (i.e. 3 keV) using Argon. The total H amount contained within the samples has been measured by means of Elastic Recoil Detection Analysis (ERDA) in glancing angle geometry. A 2.4 MeV He^+ beam hits the sample surface at an angle of 75° from the normal, while recoiled atoms (forward scattered at an angle of 30° from the beam axis) were detected. A proper Mylar foil placed in front of the detector stops all the scattered He ions, allowing to acquire the energy distribution of the H recoiled atoms. The quantification of H fluences and depth distribution has been carried out by using two reference samples, with an independently measured H profile.[21] The qualitative analysis of bonded hydrogen of the samples has been determined by Fourier Transform Infrared (FTIR) spectroscopy in the range of frequencies from 400 to 7000 cm-1. FTIR spectra of the films were recorded by using FTIR spectrophotometer

2.3 Results and discussion

2.3.1 Variation in deposition rate

To optimize the fabrication and properties of nc-Si:H, it is also important to control the growth mechanism. We investigated the variation of deposition rate as a function of hydrogen dilution of silane, R, defined above. In the measurement of the deposition rate, the thickness was taken by TEM analysis in cross section. Fig. 2.1shows the deposition rate as a function of R for the different samples.

As seen from the figure2.1, the deposition rate decreases as R increases, for either the layers made using F_{SiH4}=12 sccm and the layers deposited with F_{SiH4}=100

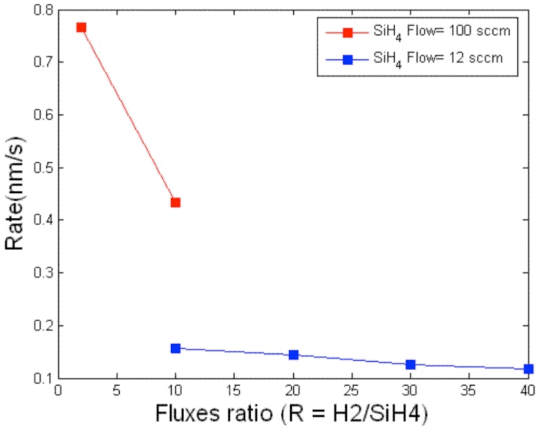

Figure 2.1: Figure 1. Variation of deposition rate as a function of hydrogen dilution of silane for a-Si:H and nc-Si:H films deposited by PE-CVD withF_{SiH4}=100 sccm (red) and F_{SiH4}==12 sccm(blue).

sccm. This result can be explained as in the following. The deposition of a film involves two simultaneous processes, and can be considered as a balance between deposition and etching of the growing surface. The net reaction can be expressed by the following equations:

$$SiH_4 \underset{R_{etch}}{\overset{R_{dep}}{\rightleftarrows}} Si(solid) + H_2$$

where R_{dep} Eq1 correspond to the deposition rate and etching rates, respectively. [3, 23]. Deposition rate is, thus, determined from the competition between deposition and etching process. The decrease in deposition rate with the increase in hydrogen dilution of SiH_4 (R) can be attributed to several factors. The first factor is that theSiH_4 density in the gas mixture decreases with the raise of R [22]. As a result, the concentration of precursors that produces silicon decreases producing a decrease of deposition rate. Another important contribution is the increase of atomic H in plasma, which leads to excessive etching and breaking of weak Si–Si bonds[23]. This leads to increase of the etching rate of silicon. As a result the deposition rate decreases. The hydrogen partial pressure in the deposition chamber increases with R. This leads to an increase in the gas phase polymerization, with the formation of higher silicon hydride species [24] with lower sticking coefficients, which further increases the etching probability. Therefore, the overall deposition rate decreases with the increase in R. In figure 2.1 it is also visible a difference about the slope of the deposition rate which is higher for the samples with F_{SiH4} =100 sccm. This is probably due to a difference about the morphological structure of the layer, as it will be detailed in the next section.

2.3.2 Tem Analysis

Figure 2 shows the plan view TEM in dark Field condition of the four samples, deposited with e F_{SiH4} = 12 sccm and with R varying from 10 to 40 (a-d). In the R=10 case, it is possible to identify nanocrystals approximately of 1.7 nm in diameter. In Fig.s 2.2 (c-d) the TEM micrographs show that the increasing of R leads to the increase in the mean dimension of nanocrystalline structure, and this result will be deeply discussed later. It is also evident the NDs present a defect density at high values of R.

The samples deposited by usinge F_{SiH4} =100 sccm were analyzed too and, after accurate analyses, the sample with R=2 was found to be completely amorphous and the sample with R=10 was nanocrystalline, presenting NDs of about 1.7 nm of diameter, i.e. with characteristics quite similar to the sample deposited with R=10 and e F_{SiH4} =12 sccm, shown in Fig. 2.2 (a). The observed variation in the morphological structure of the layers can explain the variation in the deposition rate slope shown above (see section 3.1): indeed, Van Oort et al [23] found that H2 plasma etches a-Si:H about 5-10 times faster than µc-Si:H. We may conclude that the presence of the crystalline phase affects the deposition rate, although the layers are nanocrystalline, i.e. have features much smaller than that observed by the authors.

2.3.3 Pair distribution function

To achieve a better understanding of the atomic structure of these nanovolumes, an appropriate methodology has to be chosen. With this regard, one of the most detailed methodologies for such materials is based on the calculation of the pair distribution function, G(r), which describes how on average the atomic density varies as a function of the distance from one atom. Distribution of atoms can be investigated experimentally by scattering experiment resulting in either images (e.g. with electrons) or diffraction pattern (e.g. for X rays, neutrons and electrons). However, because of the low scattering cross section for both neutrons and X rays, the scattered signal is too small for these techniques to be used for the study of nanovolumes. In contrast, the scattering cross section for electrons is relatively large and this allows smaller volume of material to be investigated. Moreover, electrons can be focused with lenses to illuminate chosen nanovolumes [25]. The calculation of Radial distribution function starts by acquiring the scattered intensity from a diffraction pattern. The scattered intensity is given by the Debye formula ,

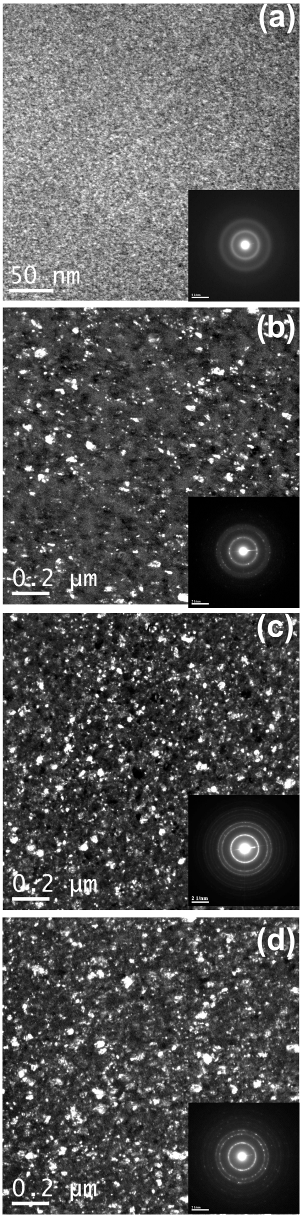
(a)
50 nm
(b)
0.2 µm
(c)
0.2 µm
2 1/nm
(d)
0.2 µm

Figure 2.2: Plan view dark field TEM micrographs obtained by selecting the s[26]pot <111> for the hydrogenated Si layers deposited using F_{SiH4}=12 sccm and R=10(a) R=20(b) R30(c) R40(d). The films present a high density of nanocrystalline dots.

$$I(q) = Nf^2(q) + \sum_{i\neq j}\sum_j f^2(q)\sin(qr_{ij})/qr_{ij}dV$$

Where $r_{ij} = |r_i - r_j|$, r_i being the distance of an atom i from the central atom and q the scattering direction from an atom i at r_i, and where we have averaged over all directions (assuming an isotropic distribution). G(r) is directly related to the local average density (ρ), so we can integrate over the sample volume assuming that the contribute at small angle is negligible and considering $r_{ij} = r$, we obtain:

$$I(q) = Nf^2(q) + 4\pi Nf^2(q)\int_0^\infty \left[g(r) - \rho_0\right]\frac{r}{q}\sin(qr)dr$$

This equation shows that there is a mean intensity term $Nf^2(q)$, which arises from the atomic scattering independently, and a second term that causes a deviation from this mean intensity if the local density at r deviates from the mean density ρ_0.

To extract G(r) from the diffraction pattern, we define the reduced intensity function φ(q) as :

$$\varphi(q) = \left[\frac{I(q) - Nf^2(q)}{Nf^2(q)}\right]q$$

The pair distribution function G(r) can be obtained by Fourier Transform of φ(q).

2.3.3.1 Data collection and Results.

Accurate calibration of the diffraction pattern is necessary because an inaccuracy in the q scale results directly in an equivalent inaccuracy in the spatial scale of G(r). After the data collection, the center of the collected diffraction pattern must be identified, and after this initial operation we can collect I(q) directly from the diffraction pattern. The conversion of I(q) to φ(q) it is not easy to calculate, because it requires a knowledge of the electron atomic scattering factors. However many researchers [25] have noted that useful G(r) can be obtained by fitting I(q) with a polynomial of second degree, as it is frequently done in neutron and X-ray diffraction studies. Peak position in G(r) are not strongly influenced by the fit, although this leaves N not univocally determined. In fig. 2.3 a) the red curve shows the behavior of the I(r) for the nc-Si:H sample obtained at R=10, F_{SiH4} =100 sccm as an explanatory example. In the same graph it is also reported the fit with a polynomial curve of second degree (black dashed line), and this represents

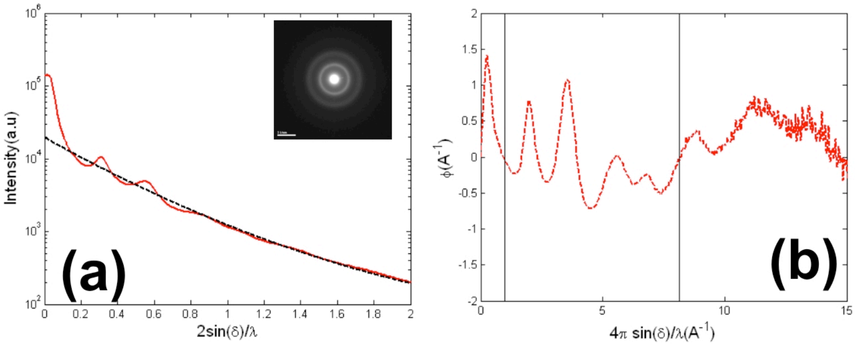

Figure 2.3: a) The scattered intensity I(q) (red line), for the sample deposited using FSiH4=12 sccm and R=10, the dashed line represent the background , calculated by fitting with a polynomial curve of II degree. The inset shows the diffraction pattern from which we collected I(q), (b) Calculated φ(q).The vertical lines indicate the range chosen for the calculation of G(r).

the background (BG) of the I(q). This allows us to consider only the scattering's contribute which depends on the mean interaction between the central atom and the atom matrix in which it is embedded.

Fig 2.3 b) show the calculated φ(q) using the relation :

$$\varphi(q) = \left[\frac{I(q) - BG(q)}{BG(q)}\right] q$$

we need to eliminate some contributions of the φ, at lower frequencies to eliminate artifacts due to transmitted beam and to camera acquisition, and at high frequency in the noisy zone, because the noise can generate the presence of spurious peaks in the G(r). The vertical thin lines in the graph represent the range that we choose for the integration, and this has been kept the same for every sample. Fig. 2.4 shows the results for the calculation of G(r) for the several samples. The vertical thin lines at the bottom of the graph indicate the peaks position in the G(r) of c-Si relative to the position of coordination shells. The dashed curves represent the samples deposited with F_{SiH4} = 100 sccm, while the continuous line represent the sample made with F_{SiH4}=12 sccm.

As evident in fig. 2.4 for the a-Si:H film (with R=2 and SiH_4flow of 100 sccm, dashed black line) only the first three peaks exhibit a sharp structure, and at larger interatomic distance the peaks become less defined. Moreover the first peak is evident and sharp only in the first sample, while in the other samples is less defined and shifted towards lower r. It should correspond to the Si-H bonding length

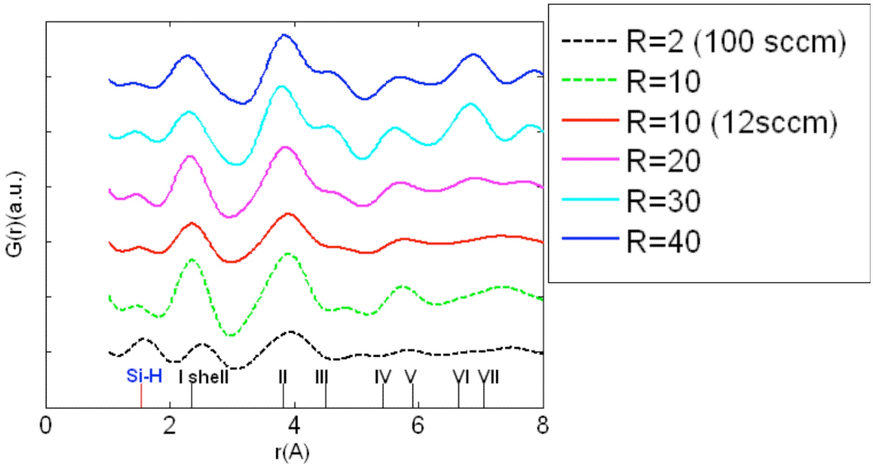

Figure 2.4: Pair distribution function, G(r), of the a-Si:H film for the several flow values R. The samples were made by using 100 sccm of silane flow (dashed line) with R=2 (black curve), R=10(red curve), and 12 sccm SiH_4 flow (continuous line) with R=10 (green curve), R=20 (magenta curve), R=30 (cyan curve) and R=40 (blue curve). The G(r) of a-Si:H evolves towards that of c-Si and begins to exhibit peaks that correspond to the higher crystalline coordination shells. The vertical lines indicate the peak positions in the g(r) of c-Si.

reported in literature at 1.5 Å. The second and third peaks correspond respectively to the first and second coordination shell of crystalline Si. By increasing R, the g(r) evolves towards that of c-Si, exhibiting peaks that correspond to the third, fourth and higher crystalline coordination shells. The appearance of these structural features indicates unequivocally that the a-Si:H film becomes progressively more crystalline when R increases. Fortner at al.[27] studied the amorphous silicon Radial distribution function. Comparing our results with the literature data, we are able to spot some differences. The a-Si:H, showed in figure 2.4, presents the second peak at r=2.54 Å, and this corresponds to the first coordination shell for Si-Si bonding. In literature the first peak is at about 2.35 Å the typical lenght for the first-nearest neighbour distance.

In the case of amorphous alloys, partial distribution functions can be deconvoluted. For a binary system, there are three of such functions ($g_{AB} = g_{BA}, g_{BB}, g_{AA}$), and each of these contribute to the total distribution function. The standard way to extract G(r) and the partial g_{ij}(r) consists in obtaining three different sets of data [three different experimental I(q)], each of which has a different dependence of the scattering factor f (q) upon q. If we are limited to electron diffraction experiments (as we are in this chapter), then there is no possibility to obtain different I(q) with the required different f(q) dependencies, because we can not vary the electron energy during the analysis. Due to this indetermination of f, we made a fit with a polynomial background, as we discussed earlier, and, as a consequence we obtain an uncertainty in coordination numbers, but not in the spatial resolution of r. For this reason we can say that the effect of the H insertion in an amorphous silicon leads to a change in the mean Si-Si bonding length and it is visible in the PDF as a peak typical of the Si-H bond and in the shift of the first two peaks toward a larger distance.

2.3.4 Hydrogen content: Elastic Recoil Detection Analysis

To understand the correlation between the above results and the effective content of hydrogen in the films, we performed Elastic Recoil Detection Analysis (ERDA) which determines the total hydrogen content, either bonded or not. The ERDA result are showed in figure 2.5.

As it is possible to see in figure 2.5 the hydrogen content decreases by increasing the hydrogen flow for the sequence SiH4 = 12 sccm (square symbols). This can be correlated to literature results [3, 28, 29] which present PECVD materials deposited by varying the Hydrogen dilution (which correspond to our definition of R), which report that for intrinsic Si:H films in the crystalline phase the hydrogen content decreases with the increment of hydrogen dilution (R)[28, 29] . In the figure2.5 the data relative to the 100 sccm flow samples are reported (circles symbols). At the moment no detailed understanding of this last result is available. Further investigation on the H content evolution should be performed at higher H

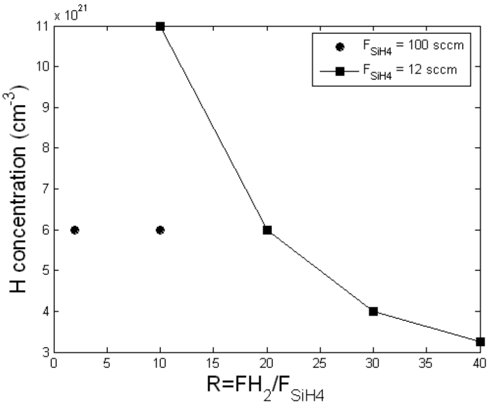

Figure 2.5: Hydrogen concentration for sample made by PECVD using different silane flow 100 sccm (black circle), and 12 sccm (black square) and different Hydrogen dilution(R).

dilutions.

2.3.5 H role in the transition

In literature it is shown, through Pair distribution function (PDA) and ERDA analyses, that the hydrogen has a role in the transition from a-Si:H to nc-Si:H, inducing a gradual crystallization of the sample. Moreover during the phase transition, a part of the hydrogen leaves the layer during this transition. In particular, Sriraman et al. [30] explained well the mechanism of hydrogen-induced crystallization of amorphous silicon using a post-deposition treatment. They investigated the structural evolution of a-Si:H films upon exposure to H (and/or D) atoms through a combination of molecular-dynamics (MD) simulations and *i*n situ attenuated total-reflection Fourier-transform infrared spectroscopy (ATR–FTIR). They discovered that H-induced crystallization is mediated by insertion of H atoms into strained Si–Si bonds, through the formation of intermediate bond-centred Si–H–Si configurations, as the H atoms diffuse through the a-Si:H film. After the H moves away from the bond-centred location, the strained Si–Si bonds either break or relax, then undergo local structural rearrangements that result in bond lengths and angles closer to those of c-Si. To explain this, in figure 2.6 a schematic showing a seven membered ring defect relaxation is reported. During the H-insertion (red dots) reactions in the proximity of a representative Si cluster, the H atoms break Si-Si bonds that present a tensile (red lines) or compressive strain (green lines) and this leads to a Si–Si bond relaxation, leading eventually to atomic displacements

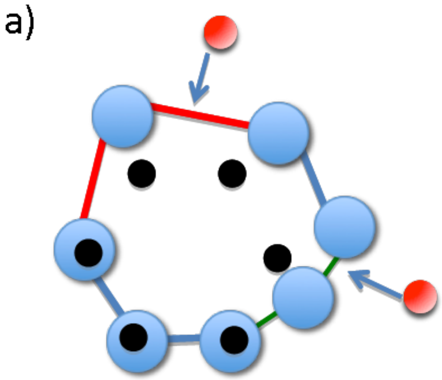

Figure 2.6: Figure 6. Schematic representing the local structural rearrangements of Si atoms (blue spheres) before (a) and after(b) interaction with hydrogen atom (red spheres . The Si-Si bonds are indicated for the equilibrium bond lenght 2.35 Å by the blue line, and for the ones under tensile or compressive strain by red lines or green line respectively. The superposition of the black dots that indicate the c-Si lattice positions onto the Si cluster structure, obtained after many H interaction events, shows that the rearranged atomic positions in the Si cluster correspond well with the equilibrium c-Si lattice sites.

toward the equilibrium c-Si lattice positions (black dots) fig b. In the figure the breaking event is indicated by the arrows.

Structural disorder arising from coordination defects is commonly found in a-Si:H (fig 2.6a). Energetically more stable and ordered structures resembling c-Si are formed when such defects, like compressive o tensile strained bonds are annealed, as a result of H interaction, through a combination of insertion by bond breaking(fig 2.6a), bond reformation and network rearrangement processes (Fig. 2.6b) towards the equilibrium c-Si lattice positions. As a result of the atomic displacements, a coordination defect present in the form of a seven-membered ring is eliminated, resulting in a structure which resembles that of c-Si (Fig. 2.6b). The superposition of the black dots that indicate the c-Si lattice positions onto the Si cluster structure, obtained after many H interaction events, shows that the rearranged atomic positions in the Si cluster correspond well with the equilibrium c-Si lattice sites. The H-insertion reactions into the bond-centred location facilitate rearrangement of the amorphous Si network to crystallize even at very low temperatures where thermal annealing is expected to be too slow to lead to nucleation and growth of nanocrystalline silicon. This chemically induced ordering mechanism is in contrast to thermal annealing, which leads to crystallization as a result of thermal fluctuations at high annealing temperatures.

2.3.6 The Hydrogen bonding structure: FTIR Analysis

ERDA analysis is useful to determine the absolute total hydrogen content, but to investigate the Si-H bonding configuration in the samples FTIR spectroscopy was used.

There are several way in which Hydrogen can be incorporated into the amorphous silicon (a-Si) network structure with the configurations shown in fig. [31] At isolated bonding sites a silicon atom may have either one, two or three hydrogen atoms bonded to it as in the monohydride (SiH), dihydride (SiH_2) or trihydride (SiH_3) groups. In table 2.1 it is reported the assignment for the principal vibrational modes of $Si - H$, $Si - H_2$ and $Si - H_3$ groups.

This vibrational modes for the Si-H bond occur in three energy bands, a broad peak at 630 cm^{-1}, which is always present; a group of sharp lines at 800-900 cm^{-1} whose shape and intensity depend on deposition conditions; and modes in the range 2000-2200 cm^{-1}which also depends on the synthesis conditions.

Group	*Frequency(cm^{-1})*	*Assignment*
SiH	*2000*	*Stretch*
	630	*Bend*
SiH$_2$	*2090*	*Stretch*
	890	*Scissors*
	845	*Wag*
	630	*Rock*
SiH$_3$	*2140*	*Stretch*
	907	*Degenerate deformation*
	862	*Symmetric deformation*
	630	*Rock*

Table 2.1: Si-H vibrational modes [31]

The FTIR spectra of the samples are shown in fig. 2.7(a) For clarity the spectra have been offset vertically. The vertical dashed lines reports the vibrational frequencies of table 2.1.

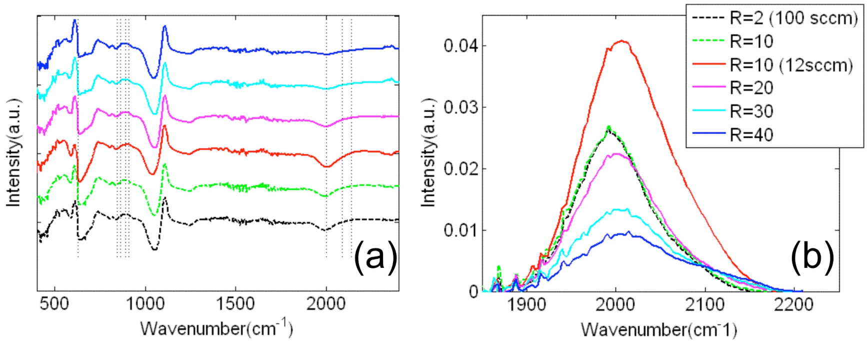

Figure 2.7: .(a) FTIR transmission spectra for silicon hydrogenated layer deposited with the different R=H_2/SiH_4 ratios, as listed in the legend on the right of the Figure, and (b) FTIR experimental data for the same sample as in a) for the 1850-2250 cm-1 range, after the background subtraction.

As it is possible to see in the spectrum, in correspondence of the frequencies at 630 and 900 cm^{-1}, it is present the signal of the Si-O, due to the SiO_2 substrate. For this reason, we decide to analyze the spectrum in the region at about 2000 cm-1.

To obtain the Hydrogen bonding concentration (C_H) it is necessary to study the variation in the absorption coefficient (α).

Infrared absorption of the vibrational mode is related to the hydrogen content through the oscillator strenght. The proportionality constant K varies as the inverse of the oscillator strenght and relates the $C_H$to the integrated absorbance.[28, 32]. Indeed, the hydrogen content C_H can be obtained by numerical integration of vibrational stretch mode at around 2000 cm^{-1}.[Langford]. The complete procedure[28, 33, 34, 32]] can be expressed by the following equations:

$$C_H(at.\%) = \frac{K_s}{N_{Si}}\int_{\nu_s}\frac{\alpha(\nu)}{\nu}d\nu$$

where $\alpha(\nu)$ is the absorption coefficient of the film at the wave number ν, ν_S stands for the stretch bands around 2000 cm^{-1}, A_s is the proportionality constant, and $N_{Si} = 5x10^{22}cm^{-3}$ is the atomic density of pure silicon. The absorption coefficient can be calculated from the transmittance data using the relation:

$$T = ce^{-\alpha t}$$

Where T represents the transmissivity, c is a pre-exponential factor and t the thickness of the layer. Figure 2.7b shows the calculation of A=-ln(T) relative to all the samples in the region at about 2000 cm^{-1}. The first operation to calculate

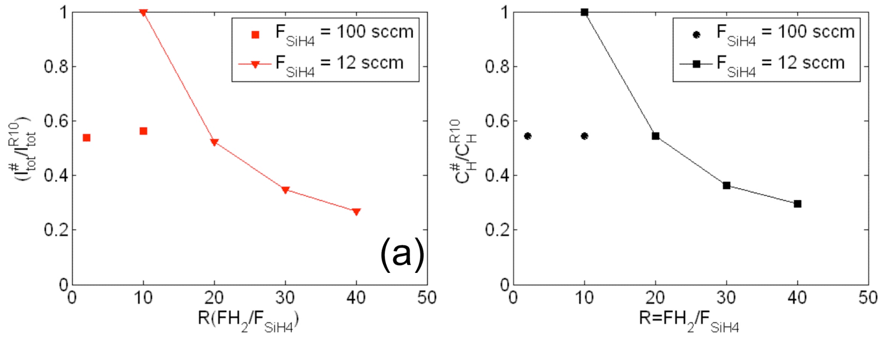

Figure 2.8: Integral of the FTIR signal for the several samples plotted as a function hydrogen dilution, and normalised respect to the signal for the sample R=10 F_{SiH4}=12 sccm,(a) and Hydrogen content of the films obtained by ERDA (b) as a function hydrogen dilution, and normalised respect to the same sample.

T is the individuation of a Background term (BG1), and then the subtraction of BG1 from the raw data. Then we can calculate A using the previous relation. As seen from figure 2.7 b), with increase in R the absorption band for the samples deposited F_{SiH4} = 12 sccm, decreases. The behaviour of the data in fig 2.7 b) is the same also if we normalize the data to the thickness of the layer, as measured by TEM analysis this means that this effect is not the effect of the variation in the thickness. Figure2.8 a) shows the behaviour of $I = I_{tot}/I_{tot}^{R10}$, where$I_{tot}$ is the integral of the curves in Fig. 2.7 b), for each sample, and I_{tot}^{R10} the integral obtained for the R=10 sample. The graph indicates that I decreases with R, and this behaviour is very similar to that obtained through the ERDA analyses, reported in Figure 2.8 (b), normalised also in this case respect to the R = 10 sample.

In Fig 2.8 (b) it is reported the hydrogen concentration, measured by ERDA, CH normalised to content obtained for the R=10 sample. By comparing FTIR (Fig 2.8 a) and ERDA (Fig 2.8 b) results it is evident that, in nanocrystalline Si layers as R increases, Hydrogen concentration decreases', both for hydrogen bonded and not-bonded. In order to understand the several contributions in terms of mono-, di- and tri-hydrides, in the FTIR signal the FTIR spectra were deconvoluted with three Gaussian peaks. The detailed analysis of such signal, revealed that each sample presents a broad peak near 2000 cm^{-1}, associated with the stretch vibrational mode of Si-H, a second peak near 2090 cm^{-1}, associated with the stretch vibrational mode of $Si - H_2$, and in most of the cases also a peak at about 2140 cm^{-1}, associated with the stretch vibrational mode of $Si - H_3$ Fig. 2.9 presents the results of such a fitting procedure. In this fit the centroids of the three Gaussian were imposed to be equal to that of literature, i.e. equal to that reported in table 1. The vertical thin lines represent the position of these literature values for the stretch vibrational modes of SiH (2000 cm^{-1}), SiH_2(2090 cm^{-1}), SiH_2(2140 cm^{-1}). The blue curves represent the raw data, while red curves represent the convolution of the three components. As it is possible to see in all the deposited layers the hydrogen predominantly incorporated is in the mono-hydrogen bonding configuration. By the analysis of the sample deposited using F_{SiH_4}=12 sccm it is possible to see that the contribution due to the mono hydrogen bonding (magenta curve) gradually decreases as R increases, while the contribution due to the SiH3 bonding (cyan curve) increases as R increases.

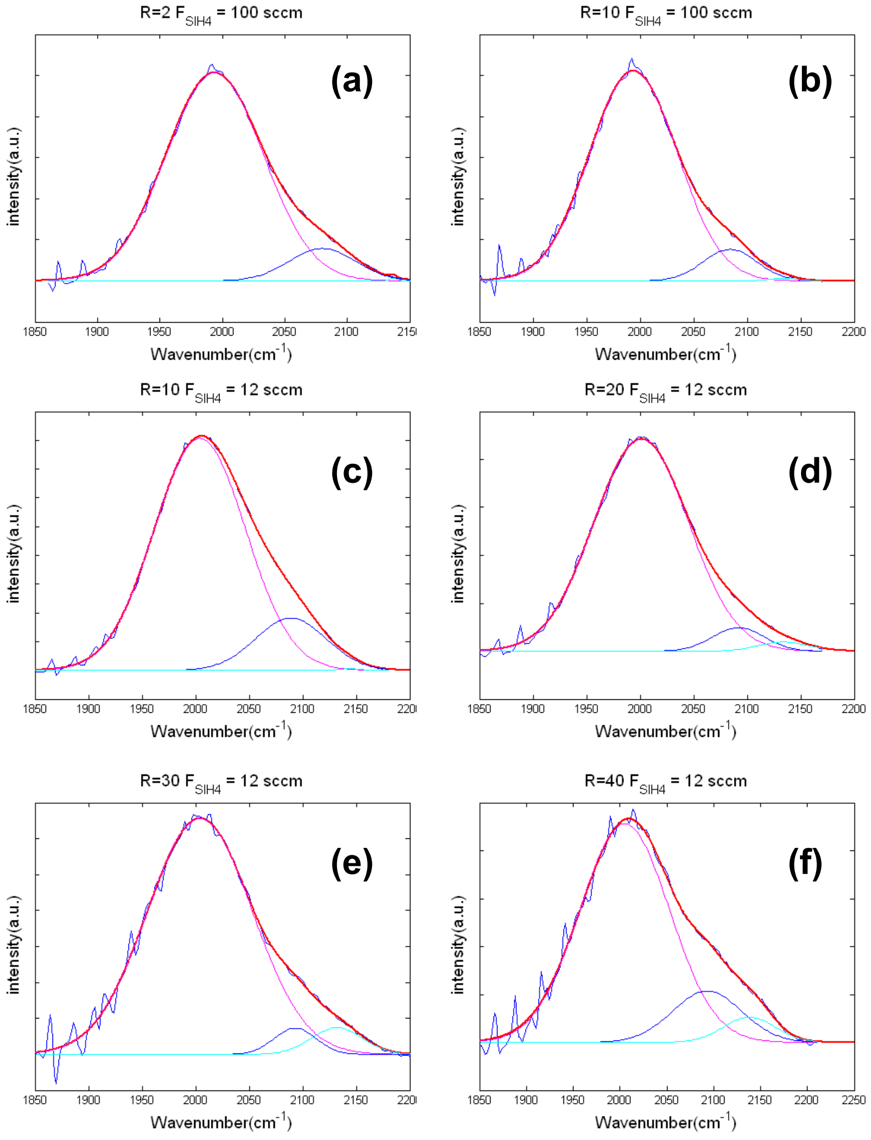

Figure 2.9: FTIR experimental data for the several samples (graph (a) to (f)), and results of the gaussian deconvolution, by using the frequencies listed in table 1 relative to SiH, SiH_2 and SiH_3. The vertical thin lines represent the position of these literature values for the stretch vibrational modes of SiH(2000 cm^{-1}), SiH_2(2090 cm^{-1}), SiH_3(2140cm^{-1}). The blue curves represent the raw data, while red curves represent the convolution of the three components.

From the analysis of the FTIR data. shown in Figure 2.9, it is possible to see that the contribution of the third peak, relative to the SiH_3 signal evolves with R. To better follow this evolution, we calculated the Integral associated with Si-H$_3$ vibration (I$_3$) and normalised it to the signal associated to Si-H(I$_1$). The result is showm in figure 2.10. In this graph it is possible to see that, by increasing R the percentage of SiH_3 bonded species increases monotonically. This result can also be correlated to the result found in Fig. 1, relative to the deposition rate, which was found to decrease with the hydrogen partial pressure in the deposition chamber. This leads, as said, to the formation of higher silicon hydride species (24) wich have lower sticking coefficients, which further increament of the etching probability. The vibration around 2140 cm^{-1}can be assigned to poly-hydride bonds on (100) and (111) surfaces in silicon crystallites [28, 35]. This indicate that hydrogen is preferentially bonded at the surfaces of the nanocrystalline grains; the SiH$_2$ is present also in the amorphous sample (R=2 $FSiH_4$=100 sccm). It should be noted that in the amorphous sample the SiH$_3$ is absent, while it appears in the Si layer that present NDs. For this reason we can consider the SiH3 bonding as a typical fingerprint of the transition. From the FTIR result we can conclude that the bonded hydrogen leaves the sample as R increase and the remaining hydrogen preferentially bonds at the surface of the nanograin, or leads to voids formation.

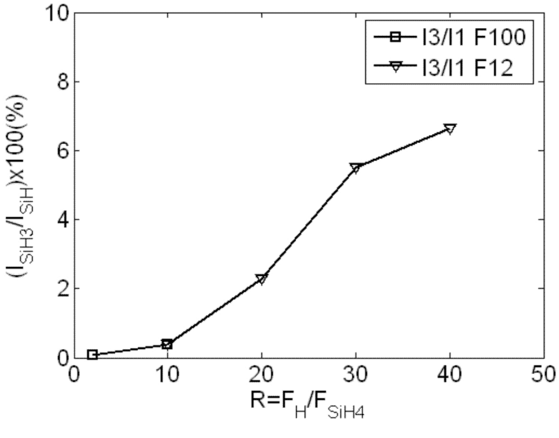

Figure 2.10: Si-H3 bonded species correlated with the SiH bonding, for several sample. The triangles represent the layer deposited with F_{SiH_4}=100 sccm, while the square represent the layer sequence deposited with F_{SiH_4}=12 sccm.

2.3.7 Dot Size correlation with hydrogen dilution

The argument depicted above, finds an experimental evidence from the structural analysis of one of the nanostructured samples. Figure 2.11(a) shows the TEM micrograph acquired in bright field condition of the sample with the R=20 deposited with F_{SiH4} = 12 sccm. From bottom to top we can see the silicon substrate (black zone), the SiO2 layer and the deposited layer. The deposited silicon layer shows a large fully nanocrystalline region at the surface, with a conical / columnar structure. In the region immediately adjacent to the interface with the SiO2 the crystallographic phase is not identified. Some authors showing the same conical structures, propose that onterface is a layer seeding region, made by a mixed phase, close to the interface.

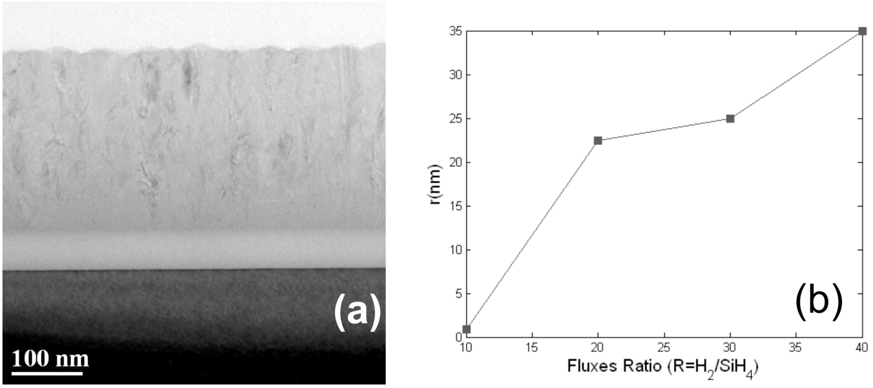

Figure 2.11: TEM Micrograph in bright field condition of R=20 sample, showing the Silicon substrate (dark grey region), the SiO_2 substrate (light grey region=) and the deposited Si:H layer, which shows a poly-columnar morphology in the upper part of the layer. (b) Mean size of nanostructure at various R for samples deposited withF_{SiH4} =12 sccm, obtained through plan view TEM analysis in Dark field condition. The data represent the mean radius of the dots present in the surfacial region of the Si:H layer.

By plan view analysis we are not able to detect if there is indeed an amorphous component in such interface layer, because for the TEM observation the specimen is thinned down to about 100 nm of thickness to be transparent to the electron beam, so the plan view analysis shows only the morphology of the upper part of the layer. The samples with R=20, R = 30 and R = 40, F_{SiH4} = 100 sccm, showed this columnar structure as well. In the case of the sample deposited at R = 10, F_{SiH4}= 100 sccm, no columnar structure has been evidenced by cross section TEM analysis. By taking into account that there are differences in the structural characteristics of the samples among the surface and the region at the interface with the substrate, we followed the dot structural characteristics observed by plan view TEM imaging, i.e. in the surface regions of the deposited layers, as a function of R. We measured the mean dot size by dark field TEM plan view imaging, obtained by selecting the <111> diffraction spot, and Figure 2.11b shows the evolution of mean radius of the dot for the sequence of layers deposited with F_{SiH4} = 12 sccm. As we can see the mean size increases R increases. This result may be related to the decrease of hydrogen content(C_H), because as the mean dimension of the nanostructures increases, the surface/volume ratio decreases,leading to a decrease of the Hydrogen bonding concentration. Further evidence that the hydrogen bonds at the grain boundaries is given by bright field TEM (figure 2.12). The micrograph shows the R=40 F_{SiH4}= 12 sccm sample. The different grey tones highlight the nanostructures. The micrograph also evidences some white scratches, two of these highlighted by the black arrows. Given the high concentration of Si hydrides in this sample, we speculate that the voids generally present in correspondence with grain boundaries are hydrogen rich regions.

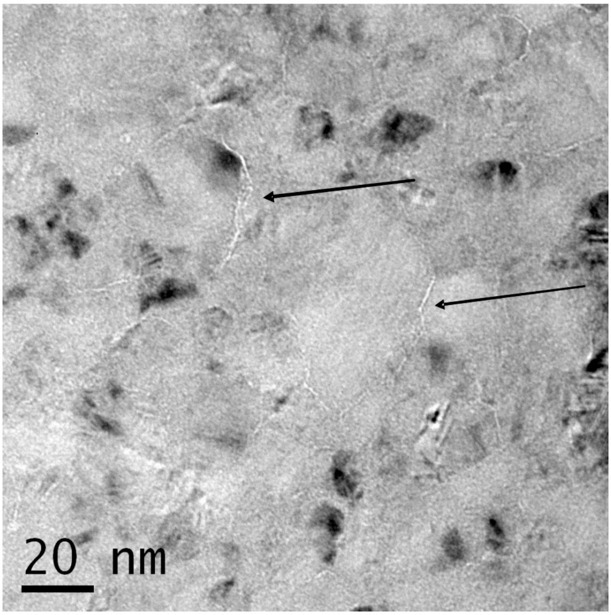

Figure 2.12: TEM Micrograph in bright field condition of R=40 sample, showing white regions, evidenced by the arrows, that represent the nanovoids created by hydrogen, and appear in correspondence of the grain boundaries.

2.4 Conclusion

In this chapter the structural properties of both hydrogenated amorphous and nanocrystalline Si thin films were investigated. The experimental data based on TEM and pair distribution function (PDF) analysis evidenced that the increasing hydrogen flow rate leads to disorder (a-Si:H) to order (nc-Si) transition. In the amorphous sample, using PDF from diffraction pattern we are able to detect the nearest neighbour contributeion of the Si-H bond. The FTIR and ERDA studies evidenced that during the crystallization process a part of hydrogen leaves the deposited layer. The FTIR studies also indicate that in a-Si:H films the hydrogen predominantly incorporated is in the mono-hydrogen bonding configuration, while in nc-Si:H films with increasing R the hydrogen bonding presents a significant contribution of SiH_3. This result correlated to the literature, which indicates that the hydrogen bonds as SiH_3 only at the surfaces and at the interfaces, indicates that hydrogen is preferentially bonded at the boundaries of the nanocrystalline grains. This finds an experimental evidence in the TEM that shows the presence of nanovoids surrounding the grain boundaries. The TEM study also shows that mean dimension of the Si nanostructures increases with H dilution.

References

[1] Staebler, D. L.; Wronski, C. R. Applied Physics Letters , vol.31, no.4, pp.292-294, Aug 1977 doi: 10.1063/1.89674

[2] Kondo et. al. Thin solid films 501 (2006) 243-264.

[3] Funde et al. Solar Energy Materials & Solar Cells 92 (2008) 1217– 1223.

[4] M.I. Hoffert, Ken Caldeira, A.K. Jain, Erik F. Haites, L.D. Danny Harvey, S.D. Potter, M.E. Schlesinger, S.H. Schneider, R.G.Watts, T.M.L.Wigley, D.J.Wuebbles, Nature 395 (1998) 881.

[5] E. Becquerel, La lumi_ere: ses causes et ses e_ets, tome second, Paris (1867).

[6] D.M. Chapin, C.S., Fuller, G.S. Pearson. J. Appl. Phys. 25 (1954).676.

[7] 7. J. Zhao, A. Wang, M.A. Green, F. Ferrazza, Appl. Phys. Lett. 73 (1998) 1991.

[8] W. Shockley, H.J. Queisser, J. Appl. Phys. 32 (1961) 510.

[9] M.J. Kerr, P. Campbetl, A. Cuevas, in: Proceedings of the 29th IEEE Photovoltaic Specialists Conference, New Orleans, (2002), p. 438.

[10] J. Singh, Electronics and Optoelectronic Properties of Nanostructures, Cambridge University Press, 2003.

[11] H.C. Cheng, C.Y. Huang, F.S. Wang, K.H. Lin, F.G. Tarntair, Thin-film transistors with polycrystalline silicon films prepared by two-step rapid thermal annealing, Jpn. J. Appl. Phys. 39 (2000) L19.

[12] T.E. Dyer, J.M. Marshall, W. Pickin, A.R. Hepburn, J.F. Davies, Polysilicon produced by excimer (ArF) laser crystallisation and low-temperature (600 1C) furnace crystallisation of hydrogenated amorphous silicon (a-Si:H), J. Non-Cryst. Solids 164–166 (1993) 1001.

[13] A.G. Aberle, N.P. Harden, S. Oelting, Formation of large-grained uniform poly-Si films on glass at low temperature, J. Cryst. Growth 226 (2001) 209.

[14] Y. Nasuno, M. Kondo, A. Matsuda, Key issue for the fabrication of high-efficiency microcrystalline silicon thin-film solar cells at low temperatures,Jpn. J. Appl. Phys. 41 (2002) 5912.

[15] A. Shah, J. Meier, E. Vallat-Sauvain, C. Droz, U. Kroll, N. Wyrsch, J. Guillet, U. Graf, Microcrystalline silicon and 'Micromorph' tandem solar cells, Thin Solid Films 403–404 (2002) 179.

[16] H.L. Hsiao, H.L. Hwang, A.B. Yang, L.W. Chen, T.R. Yew T.R, Study on low temperature facetting growth of polycrystalline silicon thin films by ECR downstream plasma CVD with different hydrogen dilution, Appl. Surf. Sci. 142 (1999) 316.

[17] B.A. Scott, R.M. Plecenik, E. Esimonyi, W. Reuter, Low defect density amorphous hydrogenated silicon prepared by homogeneous chemical vapour deposition, Appl. Phys. Lett. 40 (1982) 973.

[18] M. Fonrodonaa, D. Solera, J. Escarre ´a, F. Villara, J. Bertomeua, J. Andreua, A. Saboundjib, N. Coulonb, T. Mohammed-Brahimb, Low temperature amorphous and nanocrystalline silicon thin film transistors deposited by hot-wire CVD on glass substrate, Thin Solid Films 501 (2006) 303.

[19] Y.H. Wang, J. Lin, C.H.A. Huan, Structural and optical properties of a-Si:H/nc-Si:H thin films grown from Ar–H2–SiH4 mixture by plasma-enhanced chemical vapor deposition, Mater. Sci. Eng. B 104 (2003) 80.

[20] H. Sharai, Y. Fujimura, S. Jung, Formation of nanocrystalline silicon dots from chlorinated materials by RF plasma-enhanced chemical vapor deposition, Thin Solid Films 407 (2002) 12.

[21] Lanford NuclearInstruments and Methodsin Physics Research B66 (1992) 65-82

[22] S.C. Saha, S. Ray, Development of highly conductive n-type mc-Si:H films at low power for device applications, J. Appl. Phys. 78 (9) (1995) 5713.

[23] C.C. Tsai, G.B. Anderson, R. Thompson, B. Wacker, Control of silicon network structure in plasma deposition, J. Non-Cryst. Solids 114 (1989) 151.

[24] A. Achiq, R. Rizk, F. Gourbilleau, P. Voivenel, Effects of hydrogen partial pressure on the structure and properties of sputtered silicon layers, Thin Solid Films 348 (1999) 74.

[25] David J.H. Cockayne. Annu. Rev. Mater. Res. 2007. 37:159–87

[26] Debye P. 1925. The scattering of X-rays. J. Math. Phys. 4:133–4

[27] Fortner J, Lannin JS. 1989. Radial distribution functions of amorphous silicon. Phys. Rev. B 39:5527–30

[28] U. Kroll, J. Meier, A. Shah, S. Mikhailov, J. Waber, Hydrogen in amorphous and microcrystalline silicon films prepared by hydrogen dilution, J. Appl. Phys. 80 (1996) 4971.

[29] A. Achiq, R. Rizk, F. Gourbilleau, R. Madrante, B. Garrido, A. Perez Rodriguez, J.R. Madrante, Effects of prior hydrogenation on the structure and properties of thermally nanocrystallized silicon layers, J. Appl. Phys. 83 (1998) 5797.

[30] Saravanapriyan Sriraman, NATURE, Vol 418 (2002)

[31] G. Lucovsky, R. J. Nemanich, and J. C. Knights, Phys. Rev. B 19, 2064 (1979)

[32] A.A. Langford, et al Phys. Rev. B Vol 45 n 23 , 13367 (1992)

[33] M. H. Brodsky, M. Cardona, and J. J. Cuomo, Phys. Rev. B 16, 3556 (1977)

[34] . A. A. Langford, M. L. Fleed, and M. H. Mahan, Sol. Cells 27, 373 (1989).

[35] H. Wagner and W. Beyer, Solid State Commun. 48, 587 (1983).

Chapter 3

3rd generation solar cells: Ordered templates for nanowire synthesis

3.1 Introduction

Silicon nanowires have been recently proposed as basic building blocks for high efficiency PV cells, because they relax the constraints on the quality of the silicon material and on the amount of semiconductor required for efficient light absorption [2]. On the other hand, metallic dots grafted on the nanowire surface can produce localized plasmonic modes to enhance light absorption by the semiconductor and further boost PV efficiency [2, 3]. These two concepts can be integrated in PV production if low cost technologies for the Si nanowires and the metallic dots synthesis, among the large range of available approaches, are identified, with the target of reducing cost with maximum performances. Two of the most proposed approaches for the synthesis of the Si nanowires are based on the Vapor-Liquid-Solid (VLS) growth [4, 5, 6, 7, 8, 9, 10, 11] or on the Solid-Liquid-Solid (SLS) growth [12, 13]. In both these methods metallic nanoparticles are deposited randomly on a Si substrate and work as catalysist seeds for the nucleation of the Si phase from the vapor source, in the first case, and from the substrate source, in the second case. During the growth, in both cases however, some lateral diffusion of the metallic dots on the substrate can produce a coalescence of the metal nano-seeds, thus increasing the disorder level in the template substrate, and producing a final “forest-like” material. On the other hand the nanopatterning of semiconductor surfaces in a periodic fashion is also a topic of great interest for industrial applications. The term "nanopatterning" refers to approaches that provide periodic arrangements with feature sizes and pitches below 100 nm. The technological interest in the ongoing research for new nanopatterning techniques is based on the desire for inexpensive methods to pattern areas on the square-centimeter scale, and beyond. These methods should also be easier to realize than e-beam lithography. Most of the methods are still at the laboratory stage, however, the possibility of parallel sequenced writing based on such nanopatterning methods has already been predicted. The realization of patterned metal arrays as catalysts for the growth of semiconductor NWs is a new application of the nanopatterning techniques. In this respect, the metal-catalyst arrays function as a template for the subsequent growth of NWs via the VLS model, so that the NWs would have the same pattern as the metal dots and the diameters of the nanowires are correlated to the size of the catalyst dots. Therefore, when position control of spatially separated NWs is desired, nanopatterning techniques become essential. A number of patterning and templating methods can be applied for the controlled preparation of metal dots arrays on a substrate surface, including photo- or e- beam lithography, manipulation of single Au nanodots, arrangement of Au nanocrystals from suspensions, nanosphere lithography, gold deposition masks based on porous alumina templates, nanoimprint lithography. All of these above methods are distinguished by the effort required and their ability to pattern large areas, and for cost production[11]. There are several low-cost methods present in literature for producing ordered templates for the nanowire growth, but the final catalysts seed density is usually lower than $1x10^9cm^{-2}$, or not directly compatible with standard semiconductor processing techniques. Some recent approaches for the fabrication of solar cells based on Si wires utilize standard lithography [2], with demonstrated excellent optical absorption results. To try to improve the charge transport to the electrical contacts, also in presence of impurities which work as electronic traps, it seems to be feasible to deal with wires of sizes in the nanometer scale.

The choice of using these nano-structures is driven by numerous factors. The ability to move toward an almost direct gap with the ability to vary the energy by varying the diameter of the wires is one of the main factors. Nanowires are one-dimensional nanostructures with electrical carriers confined in the other two (perpendicular) directions. They exhibit interesting physical properties that are noticeably different from those of the bulk. Zhao et al [14] have demonstrated from first principles the structures of SiNWs oriented in the [110] and [111] directions and their electronic and optical properties as a function of diameter. They found an almost direct band gap for [110] and small [111] nanowires, the result of their work is that the Energy gap increases subquadratically as diameter shrinks. They found that for a nanowires oriented in [110] direction with diameter of about 6-8 nm the resulting energy gap is about 1.4 eV. This result is very close to the Shockley–Queisser limit [15] The theoretical maximum almost corresponds to the GaAs band gap(1.42 eV). However, due to high production costs GaAs is reserved for solar space applications, for this reason in very interesting the use of a technique that is able to achieve an Eg of 1.4 with low cost production. Furthermore the subwavelenght light-trapping effects in silicon nanowires arrays improve optial absorption properties respect to thin film [1]

In this chapter a facile route for the low-cost production of large – scale substrates templated with ordered nanometric patterns of metallic dots, specifically gold nanodots (NDs), is demonstrated. The method is based on the formation of a polymeric nanomask by diblock copolymer self-assembling [16, 17, 18] and successive dry etch to transfer the polymeric pattern on the oxide substrate [19, 20, 21, 22, 23]. The obtained substrate is made of a silicon dioxide layer with nanopores 20 nm wide and separated by a 40 nm distance, etched down to the Si substrate. Afterwards a single layer of NDs, with coverage 20%, is deposited by sputtering all over the template, and subjected to thermal annealing at temperatures ranging between 600 and 1000 °C, to diffuse the metallic NDs on the surface. In this chapter it is shown that the NDs deposited outside the pores, during the annealing diffuse and coalesce to the Au dots deposited inside the pores. The final result of this process is that most of the nanopores are saturated with the gold NDs, and the density of saturated nanopores can be tuned by changing the annealing temperature. The preferential diffusion of the gold NDs toward the nanopores is followed *in situ* by annealing the samples during TEM imaging, and ex-situ by annealing in furnace the samples and observing them by TEM and high-statistics SEM analysis.

3.2 Experimental

The self-assembled templates were realised on oxidized p type Si substrates with wet oxides of 15 nm of thickness. We used a commercially available PS–PMMA diblock copolymer with average molecular weight $M_n = 67000$ g/mol, polydispersity index of 1.11, and PMMA weight fraction of 30%. The polymer was dissolved 1% by weight in toluene. Sample preparation started with an initial surface pretreatment with a random copolymer, the Poly(styrene-co-methylmethacrylate) TEtraMethylPiperidinylOxy (TEMPO) terminated, necessary to neutralise the substrate to the two block copolymers and to promote the proper orientation of the hexagonal template. The polymer-coated substrates were then heated under vacuum at 140 °C for 48 hours, above the glass transition temperature of both PS and PMMA, to allow the terminal OH groups to diffuse to and react with the oxide substrate [24]. Unattached polymer chains were removed by rinsing in toluene for 30 min at room temperature. The thickness of the grafted layers as measured by ellipsometry was about 3 nm. A 30 nm thick film of diblock copolymer was spin coated on the pretreated substrate and annealed in vacuum at 190 °C for 1 hour, to promote the microphase separation of the blocks and self-organization into the hexagonal array. The template formation was completed by exposing the samples to ultraviolet light, which degraded the PMMA and cross linked the PS. The UV exposure was performed by using a low pressure mercury lamp, with a wavelength of 254 nm, and a power density of 12 mW/cm^2, and placing the samples under the tube at a distance of about 2 cm. The exposure was taken in air for 20 min. The copolymer was developed in acetic acid, which removed the PMMA cylinders and left a porous PS template. The developed samples presented a closepacked hexagonal array of pores, arranged in several macrodomains randomly oriented between each other [25]. The diameter of the nanopores was about 20 nm, while the distance between the centers of the pores was statistically measured to be about 40 nm. The polymeric template was then used as a lithographic mask to tranfer the pattern on the oxide underneath. The pattern transfer was obtained through a Reactive Ion Etching (RIE) based on a mixture of tetrafluoromethane (CF_4,) and nitrogen, with gas fluxes of 10 sccm for CF_4, and 10 sccm for N_2, by using a RF power of 440 mW/cm^2, a chamber pressure of 15 Pa, and an etching time of 600 sec. After the RIE etch all the samples were subjected to a cleaning through a plasma process based on O2 ashing, and to a brief HF dip. After cleaning the samples were introduced in the sputtering chamber for the gold deposition. The metallic dots were deposited by sputtering a gold target on the nanopatterned substrate at room temperature; by using an Emitech K550X sputter coater, at $2X10^{-1}$ mbar of partial pressure and 15 mA of gun current, for 10 sec. The sputtered samples were annealed in a horizontal furnace in argon ambient, for 1 hour at temperatures ranging between 600 °C and 1000°C. The temperature in the furnace has been raised by 10 °C/min, the gas flow was 2 l/min. Structural characterization was performed by Transmission Electron Microscopy (TEM) in cross section and plan view, by using a JEOL JEM 2010F microscope with field emission gun operating at 200 kV accelerating voltage, equipped with a system for Energy Filtered TEM (EFTEM). The characterization of the early stages of the gold diffusion was performed by *in situ* TEM analysis. The samples were loaded in a GATAN single tilt heating holder. The temperature is measured by a thermocouple and is accurate within a couple of degrees. The structural characterization of the samples was also performed by scanning electron microscopy (SEM), using a ZEISS SUPRA35 FE-SEM system with a field emission electron gun.

3.3 Results and discussion

Fig. 3.1 shows the patterned substrate after the copolymer nanomask formation and the successive RIE etching. The figure reports the SEM analysis in tilted view (30° along the y axis) acquired in the region of the sample close to the cleaved edge (Fig. 3.1 a), and the TEM in cross section acquired under bright field conditions (Fig. 3.1 b). As Fig. 3.1 a) illustrates, the etched oxide presented a uniform pattern of nanopores arranged in the hexagonal configuration typical of the polymeric nanomask, this confirming the fidelity of the pattern transfer by dry etch. The measured density of the nanopores was $d_p = 6x10^{10}cm^{-2}$,and their average center-to-center distance was 40 nm.

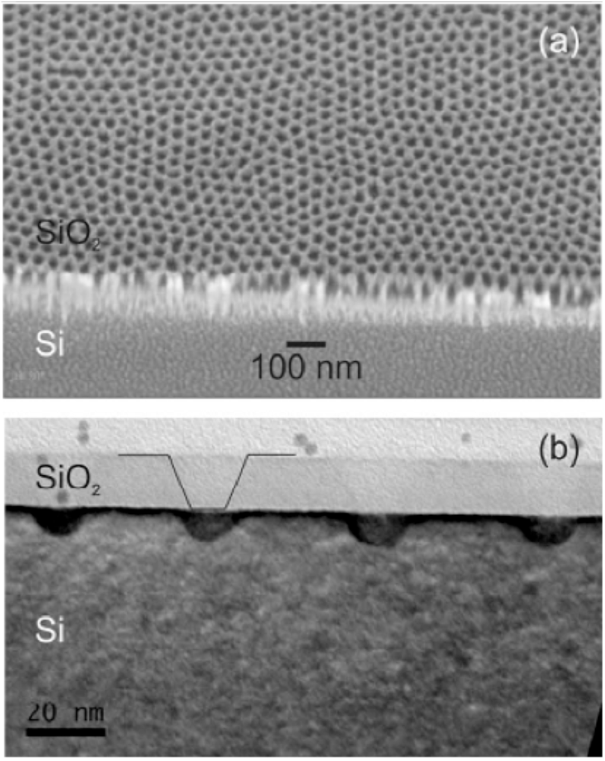

Figure 3.1: (a) SEM Micrograph in tilted view (30° along the y axis) of the nanoporous SiO_2 template realised by nanopatterning based on diblock copolymer self-assembly. The analysis was performed on the cleaved edge of the sample. It is possible to identify the Si substrate in the bottom and the etched oxide layer on top. (b) Cross-section TEM image of a sample: it is visible the 15 nm oxide layer etched down to the Si substrate for about 8 nm. The black line shows the typical etch profile in the oxide layer of the samples. The total pore depth is about 23 nm and the curvature radius at the bottom of the nanopores is about 6 nm.[26]

Fig. 3.1 b) presents the TEM cross section micrograph acquired in bright field conditions of the same sample as in a). From the micrograph it is possible to see that inside the pores the oxide layer was totally etched and the Si substrate was etched for a depth of about 8 nm. The total pore depth was about 23 nm, including the oxide etched thickness. The surface of the oxide between the nanopores is flat, indicating that the copolymer mask has protected the oxide during the dry etch. The bottom of the nanopores presented a circular profile with a curvature radius of about 6 nm. The average diameter of the pores resulted to be $< S_p >= 22$nm, so the total percentage area covered by the nanopores is $\vartheta_p = (< S_p > /2)^2 \times d_p = 20\%$.

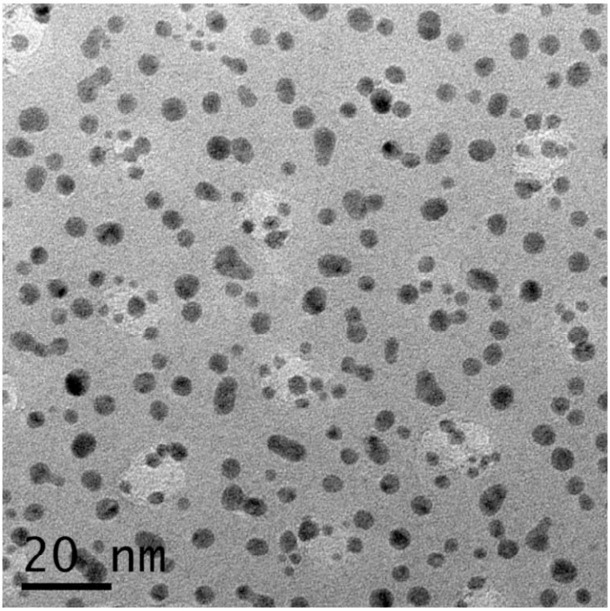

Figure 3.2: Bright field TEM micrograph of a templated oxide substrate after sputtering of gold nanodots. The white regions represents the nanopores in the SiO_2 substrate and the black dots represent the gold nanodots deposited randomically on the substrate.[26]

The sample after the gold sputtering step is shown in the TEM plan view micrograph of Fig. 3.2. It is possible to see the nanopores of the substrate, which correspond to the white circular regions, and the gold NDs, which correspond to the black spots. As the image indicates, the position of the NDs was randomic all over the substrate, presenting either dots on the planar part of the oxide and dots in correspondence of the nanopores. The TEM micrographs were digitally analysed and the Au NDs density, the average dot radius and surface coverage were calculated. The density of the Au NDs resulted $1.2 \times 10^{12} cm^{-2}$, the average dot radius 2 ± 0.7 nm, and the surface coverage 19%. The deposited equivalent thickness was calculated by assuming a spherical shape of the Au Ds, and was defined as $th_{eq} = \frac{\frac{4}{3}\pi \sum r_i^3}{A_{TEM}}$ where r_i is the radius of each dot imaged in the TEM micrographs and A_{TEM} is the total TEM analysed area, and the result was about $th_{eq} = 0.6$ nm. Fig. 3.3 reports the TEM micrograph in plan view of two samples subjected, after sputtering, to the furnace annealing for 1 h at 600 °C (a) and 800 °C (b). In a) it is possible to see the nanopores of the oxide substrate, which correspond to the white circles and form the typical hexagonal pattern described before, and the Au NDs over the patterned oxide, which correspond to the black circles. As it is clear from the image many dots are visible outside the nanopores, thus illustrating a situation similar to the as deposited sample, i.e. a random dispersion of the dots.

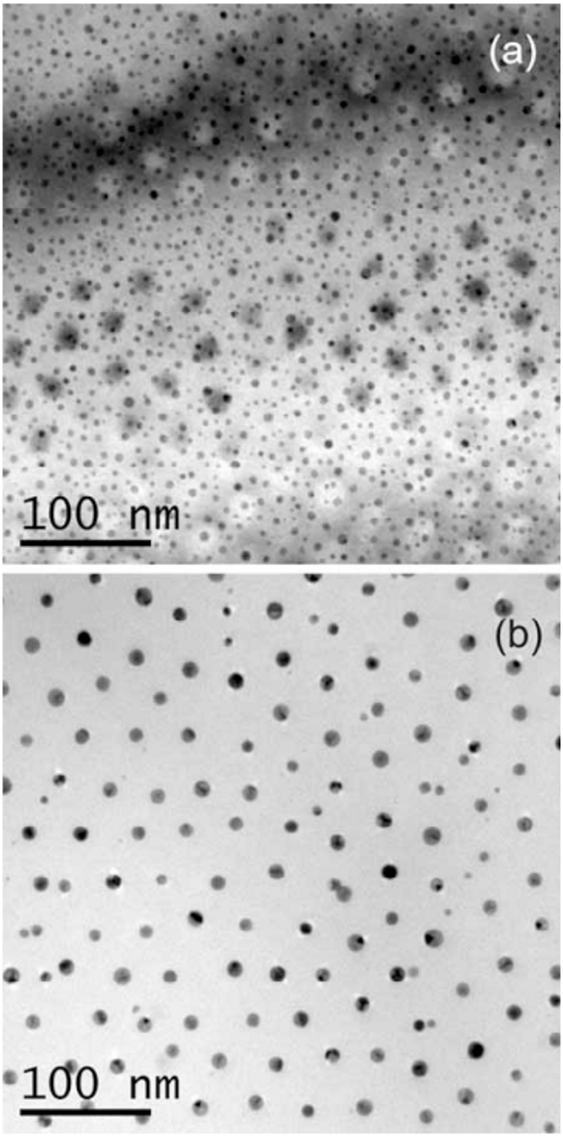

Figure 3.3: TEM micrographs in plan view of the nanopatterned oxide substrates of, after deposition of Au dots and annealing for 1 hour at 600 °C (a) and 800 °C (b). In a) it is possible to see the nanopores in the SiO2 substrate and the randomic Au nanodots (dark spots), while in b) the ordered Au dots saturating the nanopores together with few dots outside the nanopores.[26]

After 800 °C however, as shown in Fig. 3.3 b), the Au dots saturate all the nanopores and the final configuration is that typical of the polymeric mask illustrated in Fig. 3.1 a), i.e. a regular pattern of nanostructures in hexagonal configuration, spaced by 40 nm distance, with diameters of about 12 nm. From Fig. 3.1 b) the pore diameter at the top is measured to be about 20 nm, but due to the oblique etching profile, at the bottom, the pore size decreases to about 12 nm. From the geometrical characteristics of the pore in the initial substrate, and by considering the synthesis conditions of the annealed sample, i.e. 0.6 nm of Au initial equivalent thickness annealed at 800 °C for 1 h, one can conclude that in this case the pores are not completely filled, and the Au covers only the bottom part of the pores. The Au NDs present a grey/dark appearance, due to the presence of crystallographic defects inside them, which create a different contrast during bright field TEM imaging. Another result obtained from the TEM analysis is that few Au dots are still present outside the pores, and they are smaller than the dots in correspondence of the pores. The gold diffusion has been also followed at higher temperature than 800 °C, and by processing them at 1000 °C for 1 hour in furnace, the dot density decreased considerably, so to reach a sufficient statistics the results were acquired by SEM analysis, and the images will be illustrated and discussed in figure 3.6. The dot radius distribution was calculated on the above samples and the results are showed in Fig. 3.4. In particular, the results for the as deposited samples (circles), and for the samples annealed for 1 h at 600 °C (squares), 800 °C (diamonds) and 1000 °C (triangles) are reported.

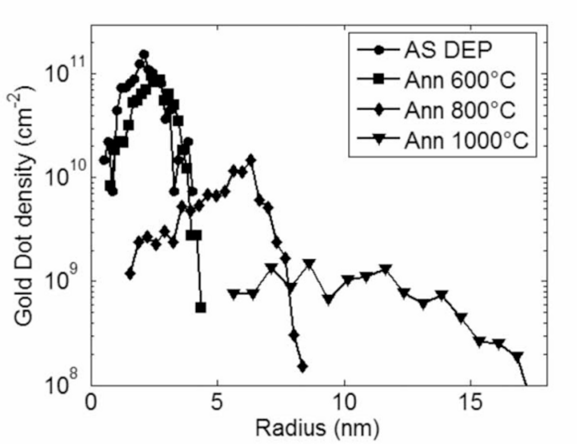

Figure 3.4: Gold dot radius distributions in the as deposited samples (circles) and for the samples annealed for 1 hour at 600 °C (squares), 800 °C (diamonds) and 1000 °C (triangles).[26]

As it is clear from the curves no large differences were evident between the as deposited distribution and after 600 °C, thus indicating that the thermal budget was not enough to diffuse an atoms over the surface, as expected from literature on Au NDs diffusion on planar substrates [28] although some coalescence took place as demonstrated by the shift of the curve at 600 °C toward large sizes. After 800 °C the distribution presents a considerable shift and a tail at small sizes due to the small dots remained outside the pores, together with a major component peaked at about 6 nm in radius, related to the dots saturating the pores. It is interesting to note that this distribution is asymmetric, the tail existing only for small sizes, and it decreases abruptly for size larger than the average size. At 1000°C the analysis of distribution shows the presence of dots with different size, the largest having size much larger than the pores, this suggesting that the growth of the large dots proceeded at expenses of the small ones. Most of these results were better quantified by calculating the dot density (a), the dot diameter (b) and the coverage (c) as illustrated in Fig. 3.5 for the as deposited case (circles), for the 600 °C (squares), the 800 °C (diamonds) and the 1000 °C (triangles) annealing. The dot density after annealing decreases monotonically, mainly due to the coarsening, and for the same process the average dot diameter increases from 4 nm up to ca. 20 nm, while the coverage decreased, reaching about 4 % for the sample annealed at the highest temperature. As previously described after 600 °C the dot characteristics are very similar to the as deposited case, while the major differences aree noticed for temperatures higher than 800 °C.

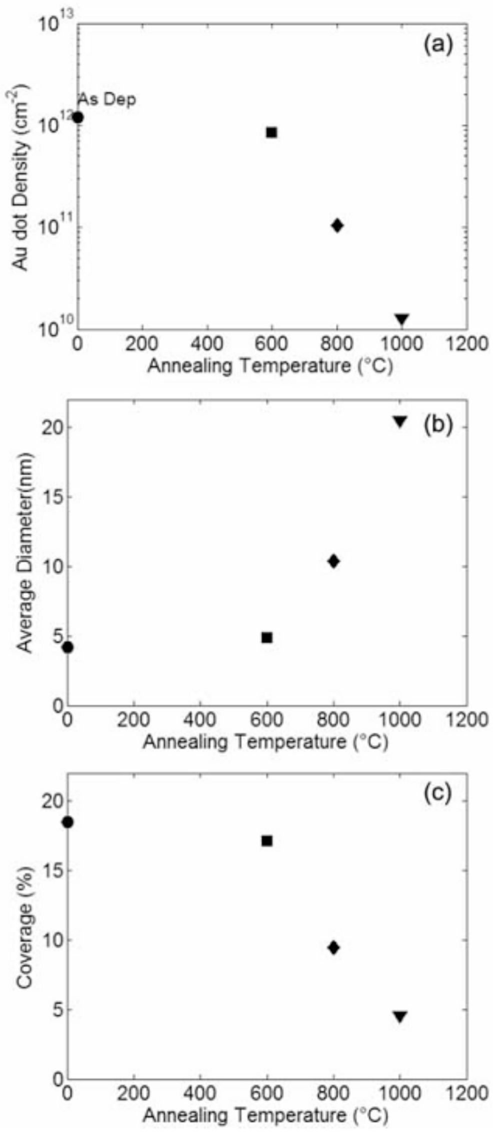

Figure 3.5: Au dot density (a), diameter (b) and coverage (c) for the as deposited samples (circles) and for the samples annealed for 1 hour at 600 ˚C (squares), 800 ˚C (diamonds) and 1000 ˚C (triangles).[26]

Although the 1000 °C case does not produce any order, it represents an interesting case, because as illustrated in Fig. 6 it provides many important insights.

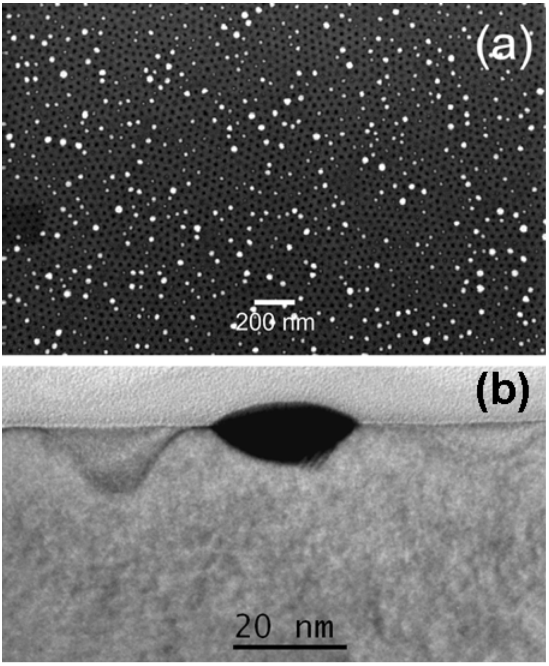

Figure 3.6: (a) SEM images in plan view of the nanopatterned oxide substrates after the deposition of Au dots and annealing at 1000 °C for 1h. It is possible to see the nanopores in the SiO_2 substrate (black circles) and the gold nanodots diffused in the nanopores (white spots).(b) Cross-section TEM micrograph of the sample show one nanopore completely filled with the gold and some empty pores close to it.[26]

The SEM micrograph shown in Fig.3.6 a) was acquired in plan view and the nanopores in the oxide substrate were imaged as black spots, while the white circles represented the Au nanodots. As the analysis showed, all the Au nanodots were positioned in correspondence of the nanopores underneath. No nanodots were imaged outside from the nanopores, i.e. on the planar regions of the oxide. Moreover, the analysis showed the presence of dots with different size, the largest having size much larger than the pores, this suggesting that the growth of the large dots proceeded at expenses of the small ones. Moreover the density of the Au dots was in this case $1.3 \times 10^{10} cm^{-2}$, which compared to the total density of the nanopores ($6 \times 10^{10} cm^{-2}$) indicates that the 20 % of nanopores was in this case saturated by the gold. Compared to the 800 °C case, where the totality of the nanopores were saturated, it suggests that some out-diffusion from the nanopores may have taken place. Fig. 3.6 b) is a cross–section TEM analysis of the same sample as in a) showing one nanopore completely filled with the gold. As it is possible to see the gold is in contact with the Si substrate, and fills the pore up to the surface. The micrograph also shows some pores close to first described, which are completely empty. Apparent etch-depth variations among the pores were an artifact of TEM sample preparation.

The experimental results of the samples after thermal annealing show that the gold dot density outside the nanopores was found to decrease, and at 800°C the total saturation of the nanopores is obtained, resulting in the creation of an ordered array of Au dots arranged in a hexagonal configuration, typical of the copolimeric mask.

The formation of the ordered array of Au dots can be attributed to two simultaneous processes: i) the surface diffusion of the Au adatoms and the ripening of the metal dots all over the oxide surface, and ii) to a preferential trapping of gold in correspondence of the pores.

The mechanism of the diffusion of Au on a flat surface of $SiO_2$is helpful to understand the first part of the mechanism of diffusion on the templated substrate. We will deal with the following parameters, i.e. the annealing temperature the mean characteristic size of the cluster, and the center-center distance, to calculate diffusion coefficient. In particular, it will be described the models of kinetic growth mechanism formulated by Kaganovskii–Beke,[29, 30], Lifshitz–Slyozov–Wagner (LSW)[31, 32], and Allmang–Feldman–Grabov[33].

The analytical description of the radial and time dependence of the cluster size distribution, f(r, t), giving the number of clusters in the radius interval (r, r + dr) per unit surface area is based on two main equations: i) The Gibbs Thompson effect, ii) Mass Transport.

The temperature dependence of the equilibrium cluster size is given below. The total Gibbs free energy of formation of a cluster of radius r, Fc (r) , describes the driving force for cluster nucleation and cluster growth. In the continuum thermodynamic limit this is given by

$$F_C(r) = (\mu_B - \mu_{free}) V_C(r) \left(\frac{1}{v_M^C} - \frac{1}{v_M^{free}} \right) + S_{CV}(r)\gamma_{CV} + S_{CS}(r)\gamma_{CS} + S_{SV}(r)\gamma_{SV}$$

where S_{SV},S_{CV},S_{CS} indicate respectively the total cluster surface/vacuum area, the total cluster/ substrate interfacial area and the total substrate surface area not covered by clusters indicate, γ the surface tensions, $\gamma_{SV} = \gamma_{CS} + \gamma_{CV} cos\vartheta$, as defined in fig. 3.7 b) and V_C the volume of the cluster, v_M^c the atomic volume in the cluster and thev_M^{free} volume per atom in the free adatom phase.

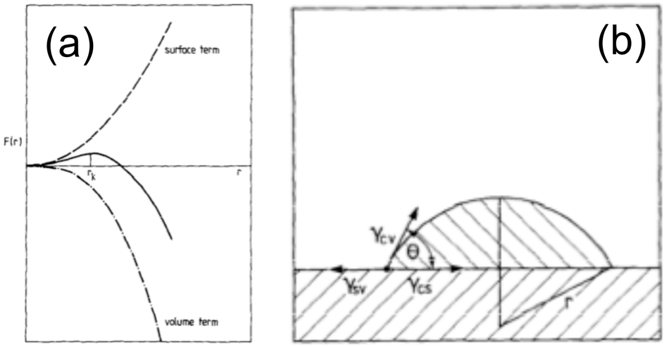

Figure 3.7: (a) The Gibbs free energy differential as a function of volume and surface term for a cluster on a surface, and (b) schematic illustrating the Young-Duprè equation for the surface and Interface tension terms for a cluster in its equilibrium shape with a contact angle[33]

By applying the condition $dF_C(r)/dr = 0$ we can calculate the cluster size r for which the increasing surface energy and the decreasing volume free energy are balanced (fig. 3.7b). The volume term corresponds to a decreasing total energy while the three surface terms correspond to an energy increase due to formation of new surfaces. Assuming the free adatom concentration to be an ideal solution on the substrate and the atomic volume in the cluster to be much smaller than in the free adatom phase, $v_M^{free} \gg v_M^C$ eq. the Gibbs free energy becomes:

$$\mu_B - \mu_{free} = \mu_B^0(T) - \mu_{free}^0(T) = KTln\left(\frac{c}{c_0}\right)$$

with index 0 for standard conditions. The standard conditions are chosen such that the surface and bulk terms of large clusters are balanced at temperature T, i.e., $c_0 = c_\infty(T)$, c ,c_0 and c_∞ represent respectively the free adatom concentration in equilibrium with a cluster of radius r, the initial adatom concentration on a surface, and the free adatom concentration in equilibrium with an infinitely large cluster. This eliminates the first two terms on the right-hand side of previous equation. Further we assume that the clusters resume their equilibrium shape allowing us to use the geometrical relations:

$$dS_{CS} = -dS_{SV},\ dS_{CS} = 1/2 < (1 + cos\vartheta)dS_{CV}$$

with ϑ the contact angle of the cluster and the Young Douprè equation $\gamma_{SV} = \gamma_{CS} + \gamma_{CV}cos\vartheta$ [31-35].

$$\frac{kT}{v_M^c} ln\left(\frac{c}{c_o}\right) = \frac{2}{r}\gamma_{cv}$$

from which, in the steady state we can obtain the critical size of the particle.

$$r_k = \frac{2\gamma_{CV} v_M^c}{kT}\left[ln\left(\frac{c}{c_\infty}\right)\right]^{-1}$$

r_k is the radius of the clusters with an equal probability to grow or decay. By adding one further atom to a cluster of critical radius the cluster becomes stable and does not decay.

Regarding the surface diffusion mechanism, adatoms diffuse over the surface layer through a process which is characterized by the surface diffusion coefficient Ds. The difference of actual concentration at the cluster surface c’(r) and c_{free}, i.e. the average free adatom concentration between the clusters, is the driving force for mass transport, and the process is described by the Fick second law:

$$\frac{\partial c}{\partial t} = \frac{1}{r'}\frac{\partial}{\partial r'}\left(r' D_s \frac{\partial c}{\partial r'}\right)$$

By applying the following bonduary conditions [41]:

$$c(r') = c_{free} \text{ at } r' = l_{sc} r sin\theta$$

$$c(r') = c'(r) \text{for } r' = r sin\theta$$

were l_{sc} represent the screening length factor usually is in range 2-3, and θ is the contact angle of the cluster with the substrate. We obtain;

$$c(r') = \left[c'(r) ln\left(\frac{r l_{sc} sin\theta}{r'}\right) + c_{free} ln\left(\frac{r'}{r sin\theta}\right)\right] / ln(l_{sc})$$

we find that the amount of material entering the cluster per unit time is:

$$\frac{dN_D}{dt} = S_D D_s \left(\frac{\partial c(r')}{\partial r'}\right)\Big|_{r'=r sin\theta} = -\frac{2\pi D_S}{ln(l_{sc})}\left[c'(r) - c_{free}\right]$$

with $S_D = 2\pi r sin\theta$, i.e., the contact line of the cluster to the substrate as the active surface in mass transport.

Figure 3.8(a) shows schematic model of the diffusion. At any stage there is a different rk which depends on the time.Basically the disgregation of the cluster with r<r_k is governed by the Gibbs-Thompson effect[39] . On the contrary the clusters with R>r_k are stable and does not decay. At any stage Fick’s law governs the surface diffusion rate, through the adatom concentration gradient. The result of the combination of these two processes is that cluster with R<r_k decays while the stable cluster (R>r_k) grows.[33] As we have just explained the motion of adatoms is characterized by the intrinsic surface diffusion coefficient Ds. On the other hand, the general theory of the ripening process based on the LSW[31, 32] ideas has the fundamental result that the mean particle radius (R) evolves as a function of time t (for time sufficiently great i.e in stationary state) according to

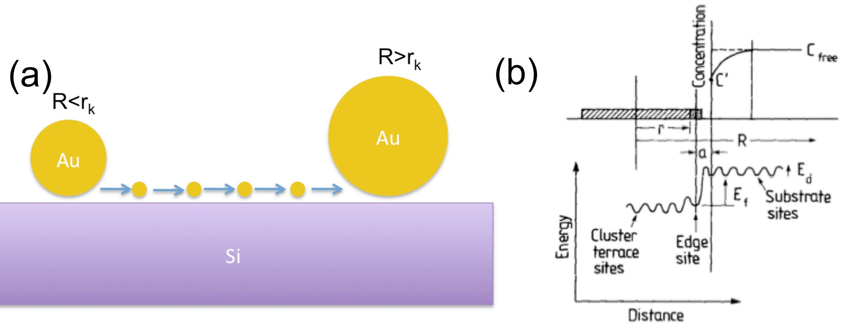

Figure 3.8: a) Sketch of the cluster's evolution, the red arrow indicate the adatoms that leave the cluster with size R<R* and adatoms that diffuse toward the cluster with R>R*due to the adatoms concentration gradient. b) Superposition of concentration distance and energy distance diagram for two dimensional cluster on a surface, showing the different energy levels involved in cluster growth[33]

$$\langle R(t)\rangle^n - \langle R_0\rangle^n = K^* t$$

where $\langle R_0\rangle$is the mean radius of the particle at time t=0 and K* is an appropriate constant depending on the diffusion coefficient D_S and on the annealing temperature.

The value of n is determined by the dimensionality of the system and the process limiting the mass transport. Ruffino et al.[28] studied the diffusion of gold nanodots, deposited in the same system used in this thesis, over a flat SiO_2 surface, and demonstrated that the experimental data on the diffusion coefficient fits well with the above equation (1), with n = 4 and

$$K* = \frac{8N_0 D_S \gamma_{CV} v_M^C}{45kTln(l_{sc})}$$

with D_s as the surface diffusion coefficient of the Au atoms, l_{sc}= 3 as characteristic length (in units of R), N_0 as the surface density of nucleation sites, v_M^c as the Au atomic volume, and γ_{CV} as the Au/air interface energy. This means that the diffusion process corresponds to the growth of 3-dimensional clusters with the mass transfer limited by surface diffusion, and interface transfer going both through the full cluster surface or through the cluster collar.

To compare the literature results about the diffusion coefficient value, at 800°C of 1730 nm^2/h, with our experimental results, we find that at this temperature the diffusion path of a gold adatom of about 25 nm, a length higher to the pores distance, and this allows the adatom to reach the pores. Figure 3.9shows the literature results, the inset is a scale picture which rapresents our pattern where

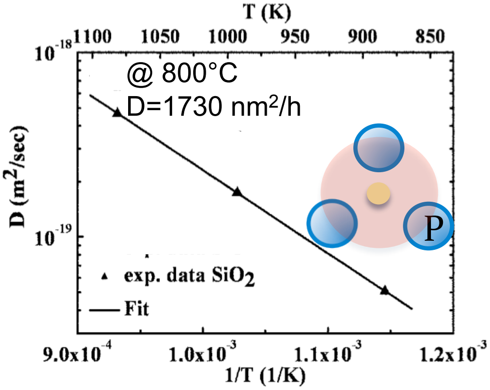

Figure 3.9: Experimental value of Ds for the SiO_2 substrate(triangles) as a function of $T^{-1}$with the relative Arrhenius fit (continuius line) [42]. The inset is a scale picture which rapresents our pattern where the blue circle are the pores and the gold sphere are the cluster, the pink shape represents the aspected diffusion area after 1 hour of annealing

the blue circle are the pores and the gold sphere are the cluster, the pink shape represents the aspected diffusion area after 1 hour of annealing,

Now we have to understand the trapping mechanism in correspondence of the pores. It should be highlighted that a trapping mechanism on nanopores has been observed already in literature by Ruffel et al. [27], which deposited Au NDs on Si with native oxide, and found that they diffused upon annealing, and first performed ripening processes, then concentrated at indented sites, realised by nanoindentation technique. In that case the trapping mechanism at the indented sites was attributed to the presence of surface defects inside them: Au NDs freely diffused over the surface outside of the indents, where the surface was defect-free, and concentrated at the indented sites, where surface and line defects such as steps and ledges, were present, and they are generally believed to act as preferred nucleation sites for metals on semiconductors [43]. The trapping mechanism in correspondence of the pores can be, also in the present case, similarly attributed to the presence of surfacial defects inside them: Au NDs freely diffuse over the surface outside of the indents, where the surface is defect-free, and concentrate at the indented sites, where surface and line defects such as steps and ledges, are present.

The early stage of the Au diffusion toward the nanopores and the trapping mechanism on the pore sides ware followed by *in situ* annealing during TEM analysis. The sample was heated up to 700 °C with a rate of 25 °C/min. Fig.

3.10 depicts bright field images acquired at various times after the temperature reached 700 °C. In the image of Fig. 3.10 a) the pores are evidenced by the white dashed circles, and identified as P_1,P_2 andP_3. In the image also several groups of dots which diffuse on the substrate and/or toward the pore, are highlighted by the black shapes. In particular, the group of Au dots marked with the numbers 1 to 7 diffuse and coalesce inside the pore P_1,. The Au dots present inside pores P_2 andP_3 remain immobile during the analysis. In the regions outside the pores many events of ripening are observed. For example, the groups of Au dots identified by α, β and γ undergo to ripening and form larger dots, as evidenced by the black arrows in the Fig.s3.10 b) and c). It is interesting to note that nucleation and growth does not occur at the same location in each pore, despite the structural characteristics are the same for every pore. Typically, during the early stages of annealing more than one particle forms in the pore and the particles are randomly positioned inside it. This suggests that there are a large number of surface defects at each pore, despite its small size.

During the whole preparation process of these type of templated substrates, atomic diffusion of Au into the Si is presumably taking place [7, 8, 44] and can represent a limiting factor for the performance of the silicon nanowire solar cells realised by Au mediated VLS, because it produces a high density of localized electronic states within the bandgap which act as generation-recombination centres. Regarding the introduction of mid-gap traps due to the gold diffusion, Perraud et al. found that the value of the reverse current in the p-n junction of their Si nanowire array solar cell, grown by Au mediated VLS, was of the order of 1 mA/cm^2, i.e. extremely high compared to that of a typical silicon wafer solar cell (1pA/cm^2). In our experiment we can estimate an upper limit for the concentration of gold toward the bulk for atomic diffusion and it is, for the highest temperature that we used, equal to $1.7 \times 10^{16} cm^{-3}$ [7], i.e. comparable to the thermodynamic bulk equilibrium concentration at 1000 °C [45]. If we consider 500 µm of thickness of bulk Silicon, and annealed it at 1000°C for 1 hour we aspect in it a Au density$8.5 \times 10^{14}\#/cm^2$ dissolved in the bulk. Comparing this result with the initial density of gold Atom $3x10^{15}\#/cm^2$ is expected that about 30% of initial Au was dissolved in Si bulk during the annealing To improve the carriers lifetime, and also to ensure compatibility with CMOS fabs, where Au may be questionable, also the catalytic properties of other metals (Al, Cu and Ni) might be investigated.

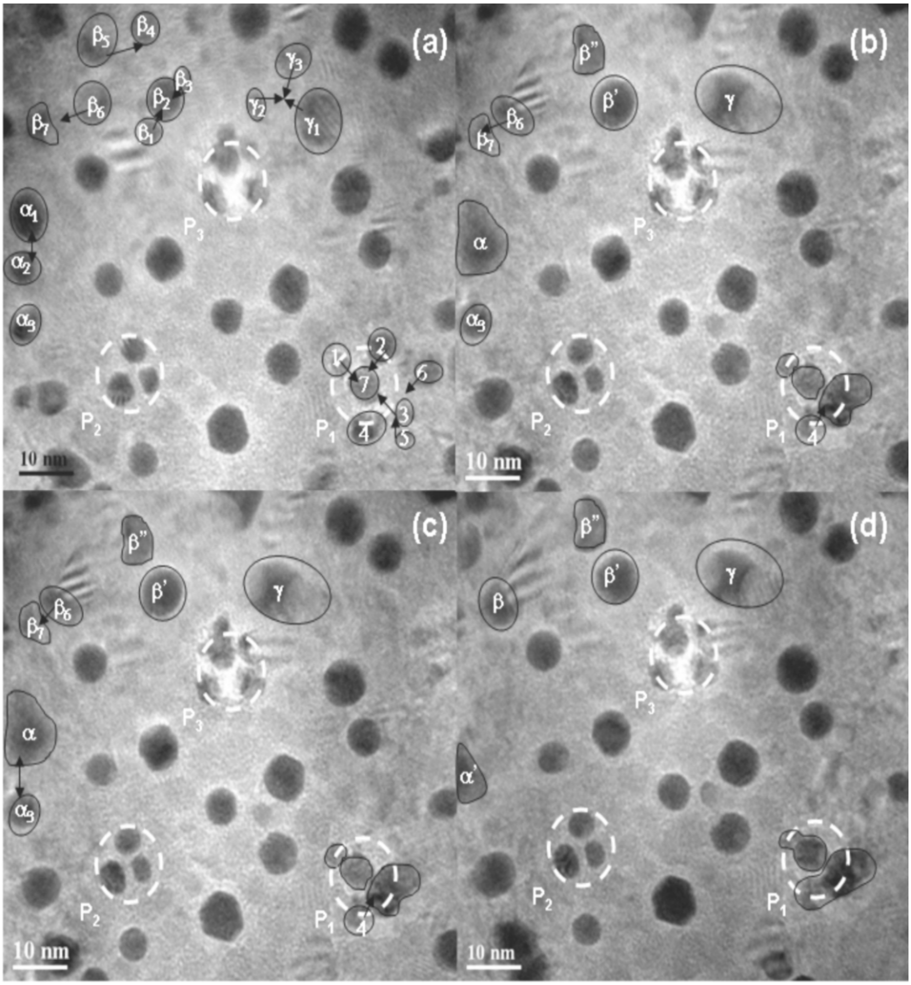
(a)
β5
β4
β3
β2
β1
β6
β7
γ3
γ2
γ1
α1
α2
α3
P3
P2
P1
1
2
3
4
5
6
7
10 nm
(b)
β"
β'
β6
β7
γ
α
α3
P3
P2
P1
4
10 nm
(c)
β"
β'
β6
β7
γ
α
α3
P3
P2
P1
4
10 nm
(d)
β"
β'
β
γ
α'
P3
P2
P1
10 nm

Figure 3.10: Bright field TEM micrographs acquired during the *in situ* thermal annealing at 700 °C for (a) 2s, (b) 58s, (c) 116 s, (d) 169 s. The pores are evidenced by the white dashed circles, and identified as P_1, P_2 and P_3. The black shapes highlight several groups of dots which diffuse on the substrate and/or toward the pore. A group of Au dots which diffuse toward one of the nanopores of the substrate are identified by number 1 to 7 . The ripening of some groups of Au dots identified by α, β and γ is evidenced by the black arrows (a), (b) and (c).

3.4 Conclusions

An easy and low-cost method to obtain ordered gold nanodots on Si substrates laterally isolated by SiO_2 was demonstrated. The method started with the formation of a hexagonal nanopattern through the self-assembling of diblock copolymer lithography. Then gold nanodots were randomically sputtered on the patterned substrate and subjected to thermal annealing at different temperatures. Their density outside the nanopores was found to decrease, and at proper temperature the total saturation of the nanopores is obtained as we can see in fig 3.11. This figure also shows the exagonal configuration of the Au NDs after the annealing typical of the copolimeric mask. The TEM analysis with in-situ annealing followed the early stages of the diffusion process.

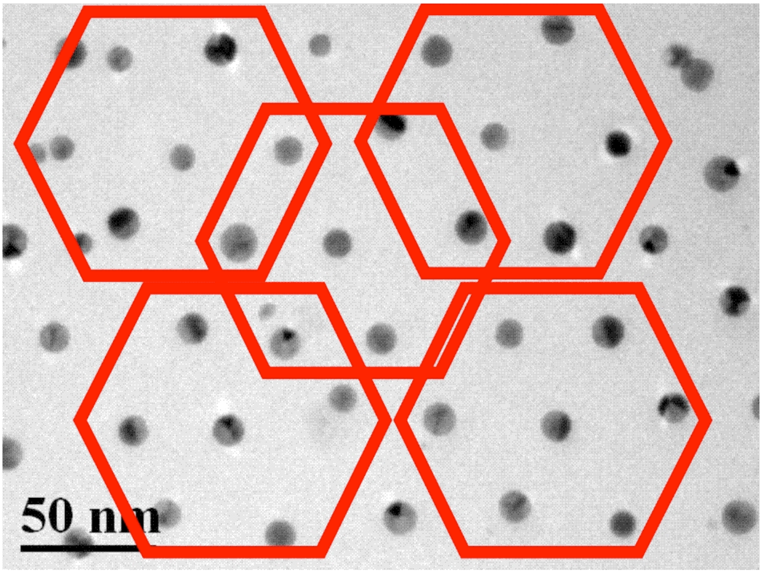

Figure 3.11: TEM micrograph in plan view of the nanopatterned oxide substrate after deposition of Au dots and annealing for 1 hour at and 800 °C. It is possible to see the Au NDs in correspondence of the nanopores underneath, arranged in the hexagonal configuration, as evidenced by the red hexagons.

References

[1] Kelzenberg, S.W. Boettcher, J.A. Petykiewicz, D.B.Turner-Evans, M.C. Putnam, E.L.Warren, J.M. Spurgeon, R.M. Briggs, N.S. Lewis and H.A. Atwater : Enhanced absorption and carrier collection in Si wire arrays for photovoltaic applications. NATURE MATERIALS. Vol. 9. (March 2010).

[2] K.R. Catchpole, A. Polman: Design principles for particle plasmon enhanced solar cells. Appl. Phys. Lett. 93, 191113 (2008).

[3] S.A. Maier: Plasmonics - Fundamentals and Applications. Springer (2007).

[4] R.S. Wagner, W.C.Ellis: Vapor- Liquid-Solid Mechanism of single crystal growth. Appl Phys Lett . 4, 89-90 (1964).

[5] E.I. Givargizov: Fundamental aspects of VLS Growth. Journal of Crystal Growth. 31, 20-30 (1975).

[6] K.W. Kolasinski: Catalytic growth of nanowires: Vapor–liquid–solid, vapor–solid–solid, solution–liquid–solid and solid–liquid–solid growth. Current Opinion in Solid State and Materials Science. 10.182-191. (2006).

[7] M.C. Putnam, M.A. Filler, B.M. Kayes, M.D. Kelzenberg, Y.Guan, N S. Lewis, J.M. Eiler, H.A. Atwater: Secondary Ion Mass Spectrometry of Vapor-Liquid-Solid Grown, Au-Catalyzed, Si Wires. Nano Lett. 8 3109–3113 (2008).

[8] S. Perraud, S. Poncet, S. Noël, M. Levis, P. Faucherand, E. Rouvière, P. Thony, C. Jaussaud, R. Delsol: Full process for integrating silicon nanowire arrays into solar cells. Solar Energy Materials & Solar Cells 93 1568–1571 (2009).

[9] L. Latu-Romain, C. Mouchet, C. Cayron, E. Rouvière, J.P. Simonato: Growth parameters and shape specific synthesis of silicon nanowires by the VLS method. J Nanopart Res 10:1287– 1291 (2008).

[10] A. Irrera, E.F. Pecora, F. Priolo: Control of growth mechanisms and orientation in epitaxial Si nanowires grown by electron beam evaporation. Nanotechnology 20 135601 (2009).

[11] H.J. Fan, P. Werner, M. Zacharias: Semiconductor Nanowires: From Self-Organization to Patterned Growth. Small. 2:700-17 (2006).

[12] H.F. Yan, Y.J. Xing, Q.L. Hang, D.P. Yu, Y.P. Wang, J.Xu, Z.H. Xi, S.Q. Feng: Growth of amorphous silicon nanowires via a solid–liquid–solid mechanism. Chemical Physics Letters 323 224–228 (2000).

[13] D.P. Yu, Y.J. Xing, Q.L. Hang, H.F. Yan, J. Xu, Z.H. Xi, S.Q. Feng: Controlled growth of oriented amorphous silicon nanowires via a solid-liquid-solid (SLS)mechanism. Physica E 9 305-309 (2001).

[14] Xinyuan Zhao, C. M. Wei, L. Yang, and M. Y. Chou. PHYSICAL REVIEW LETTERS 92(23),236805 (2004)

[15] W. Shockley, H.J. Queisser, J. Appl. Phys. 32 (1961) 510.

[16] K.W. Guarini, C.T. Black, S.H.I. Yeung: Optimization of Diblock Copolymer Thin Film Self Assembly. Adv. Mater. 14 (18), 1290 (2002).

[17] T. Thurn-Albrecht, J. Schotter, G.A. Kastle, N. Emley, T. Shibauchi, L. Krusin-Elbaum, K. Guarini, C.T. Black, M. T. Tuominen, T. P. Russell: Ultrahigh-Density Nanowire Arrays Grown in Self-Assembled Diblock Copolymer. Templates.Science. 290, 2126 (2000)

[18] I.A.Zucchi, E.Poliani and M.Perego: Microdomain orientation dependence on thickness in thin films of cylinder-forming PS-b-PMMA. Nanotechnology 21 (2010) 185304

[19] S.J. Kim, W.J. Maeng, S.K. Lee, D.H. Park, S.H. Bang, H.Kima, B.H. Sohn: Hybrid nanofabrication processes utilizing diblock copolymer nanotemplate prepared by self-assembled monolayer based surface neutralization. J. Vac. Sci. Technol. B 26(1), 189-194 (Jan/Feb 2008).

[20] K.W. Guarini, C.T. Black, Y. Zhang, H. Kim, E.M. Sikorski, I.V. Babich: Process integration of self-assembled polymer templates into silicon nanofabrication. J. Vac. Sci. Technol. B, 20(6), 2788-2792 (2002).

[21] K.W. Guarini, C.T. Black, K.R. Milkove, R.L. Sandstrom: Nanoscale patterning using self-assembled polymers for semiconductor applications. J. Vac. Sci. Technol. B.19(6), 2784-2788 (2001).

[22] P. La Fata, R. Puglisi, S. Lombardo, C. Bongiorno: Nano-patterning with Block Copolymers. Superlattices and Microstructures. 44 693–698 (2008).

[23] R.A. Puglisi, A. Scandurra, C. Bongiorno, P. La Fata and S. Lombardo: Pattern transfer of nanomasks based on diblock copolymers through Reactive Ion Etching (to be submitted).

[24] P. Mansky, Y. Liu, E. Huang, T.P. Russell, and C. Hawker: Controlling Polymer-Surface Interactions with Random Copolymer Brushes. Science. 275, 1458 (1997).

[25] R.A. Puglisi, P. La Fata, S. Lombardo: Tailoring the long range order of block copolymer based nanomasks on flat substrates. Appl. Phys. Lett. 91, 053104 (2007).

[26] C. Garozzo, R. A. Puglisi, C. Bongiorno, S. Scalese, E. Rimini, S. Lombardo. “SELECTIVE DIFFUSION OF GOLD NANODOTS ON NANOPATTERNED SUBSTATES REALISED BY DIBLOCK COPOLYMERS SELF-ASSEMBLING”. C. To be published on Journal of Materials Research (JMR), Focus Issue on Self-Assembly and Directed Assembly of Advanced Materials(2010).

[27] S. Ruffell, D.K. Venkatachalam, A. Shalav, R.G. Elliman: Formation of ordered arrays of gold particles on silicon and silicon-dioxide by nanoindentation patterning.Mater. Res. Soc. Symp. Proc. Vol. 1228 (2010).

[28] F. Ruffino, M.G. Grimaldi, C. Bongiorno, F. Giannazzo, F. Roccaforte, V. Raineri: Microstructure of Au nanoclusters formed in and on SiO2. Superlattices and Microstructures. 44 588–598 (2008).

[29] Y. S. Kaganovskii, D. L. Beke, and S. P. Yurchenko, Surf. Sci. 319, 207 (1994).

[30] D. L. Beke and Y. S. Kaganovskii, Mater. Sci. Eng., B 32, 185 (1995).

[31] I. M. Lifshitz and V. V. Slyozov, J. Phys. Chem. Solids 19,35 (1961).

[32] C. Wagner, Z. Elektrochem. 65, 581 (1961).

[33] M. Zinke-Allmang, L. C. Feldman, and M. H. Grabov, Surf. Sci. Rep. 16, 377(1992).

[34] C.H.P. Lupis, in: Chemical Thermodynamics of Materials (Elsevier, New York, 1983) chs. l-3 and 13

[35] H.-J. Gossmann and G.J. Fisanick, Scanning Microsc. 4 (1990) 543.

[36] H.-J. Gossmann and G.J. Fisanick, Surf. Sci. 244 (1991) L117.

[37] K. Binder and D. Stauffer, Adv. Phys. 25 (1976) 343.

[38] L.E. Murr, in: Interfacial Phenomena in Metals and Alloys (Addison-Wesley, Reading, PA, 1975) p. 101 ff.

[39] .J.W. Gibbs, Trans. Connect. Acad. 3 (1876) 108 (m: Scientific Papers, Vol. 1 (Longmans and Green, New York, 1906) p. 315).

[40] W. Thomson, Phil. Mag. 43 (1871) 448; Proc. R. Sot. (Edingburgh) 7 (1870) 63.

[41] T.M. Rogers and R.C. Desai, Phys. Rev. B 39 (1989) 11956.

[42] F.Ruffino, A.Canino, M. Grimaldi. Journal of applied physics 101, 064306 (2007)

[43] J.A. Venables: Atomic processes in crystal growth. Surface Science. 299/300 798 (1994).

[44] J.E. Allen, E.R. Hemesath, D.E. Perea, J.L. Lensch-Falk,Z.Y. Li, F. Yin, M.H. Gass, P. Wang, A.L. Bleloch, R.E. Palmer,L.J. Lauhon: High-resolution detection of Au catalyst atoms in Si nanowires. J. Nat. Nanotechol. 3, 168–173 (2008).

[45] W.M. Bullis: Properties of Gold in Silicon. Solid-State Electron. 1966, 9 (2),

Summary

Amorphous and nanocrystalline silicon prepared by PECVD have been investigated as active materials for Si thin film solar cells. The realization of a pin solar cell was shown, including the investigation of the key physical properties necessary to design the solar cell (sheet resistance, activation energies for conductivity, light absorption). The electrical characterizations of the solar cells in dark condition and under standard illumination were shown. Results in terms of electical performance are close to the modeling estimates. As important result the deposition conditions near the transition from amorphous to nanocrystalline Si growth have been found to be most beneficial to the solar cell properties. A further decrease of Hydrogen dilution, R, results in some decrease of short-circuit currentI_{sc} and Fill factor FF, probably caused by amorphous growth and D-center de-passivation. On the other hand, an increase of R also reduces FF and J_{sc} and results in lower V_{sc} values likely attributed to the transition to nanocrystalline Si, which decreases band-gap and light absorption. There is, therefore, a condition, the one corresponding to the transition from amorphous to nanocrystalline Si, where there is a maximum of J_{sc} ad FF which results in the best performances. These, however are roughly about 20% and 45% lower compared to the model estimates for J_{sc} and power conversion efficiency respectively. We attribute this to a too high concentration of D centers, estimated to be of the order of $1 \times 10^{18}/cm^3$ and also to the presence of non perfectly ohmic contacts, contrarily to the assumption of the simulation.

In the second part of the work we have studied the intrinsic layers to understand how the transition between amorphous and nanocrystalline silicon takes place and to understand how the structural features of the sample influence the electrical features. The experimental data based on TEM and pair distribution function (PDF) analysis evidenced that the increasing hydrogen flow rate leads to disorder (a-Si:H) to order (nc-Si) transition. In the amorphous sample, using PDF from diffraction patterns, we are able to detect the nearest neighbour contribution of the Si-H bond. The FTIR and ERDA studies evidenced that during the crystallization process a part of hydrogen leaves the deposited layer. The FTIR studies also indicate that in a-Si:H films the hydrogen predominantly incorporated is in the

mono-hydrogen bonding configuration, while in nc-Si:H films with increasing R the hydrogen bonding presents a significant contribution of SiH_3. This indicates that hydrogen is preferentially bonded at the boundaries of the nanocrystalline grains, as also confirmed by the observation in TEM of nanovoids surrounding the grain boundaries. The TEM study also shows that mean dimension of the Si nanostructures increases with H dilution.

In the third part of the thesis we have studied a methodology to obtain ordered planar arrays of gold nanodots on Si substrates laterally isolated by SiO_2. Such template can be an excellent candidate to realize the growth of ordered arrays of Si nanowires through the VLS technique, to realize III generation Si-based solar cells. The method to obtain the ordered gold nanodots on Si substrates, potentially low cost, is based on the formation of a hexagonal nanopattern through the self-assembling of diblock copolymers, followed by development and etching, similarly to a lithography process. Then gold nanodots were randomly sputtered on the patterned substrate and subjected to thermal annealing at different temperatures. Their density outside the nanopores was found to decrease, and at proper temperature the total saturation of the nanopores is obtained. In-situ TEM analysis allowed to follow the early stages of the gold surface diffusion process.

The evolution of this work will be the synthesis by using the template of ordered gold dots of the Si nanowires through the VLS technique, up to the realization of complete Si nanowire solar cells.

Curriculum Vitae

Cristina Annamaria Garozzo

November 29, 1981 Born in Catania, Italy.

1995-2000 Secondary school in Liceo Scientifico "M.Amari" , Linguaglossa(Catania (Italy)).

2000-2007 Academic degree in Physics, University of Catania (Italy). Dissertation: Effetti di geometria nelle caratteristiche di programmazione e cancellazione di memorie non volatili con architettura FinFeT. Project: FinFlash. Supervisor: Dr. Salvatore Lombardo, Prof. Emanuele Rimini.

2007-2010 Ph.D research at XXIII Materials Science at the University of Catania under supervision of Prof. E. Rimini, Dr. Rosaria Puglisi and Dr. Salvatore Lombardo. Subject: Si Based nanostructures for solar cells.

List of publications

- C. Gerardi, S. Lombardo, G. Cina, E. Tripiciano , D. Corso ,V. Ancarani , G. Iacono , C. Bongiorno, *C. Garozzo*, P. Barbera, G. A. Costa, C. Coccorese, M. Vecchio , E. Rimini and M. Melanotte: “Highly manufacturable/low aspect ratio Si Nano Floating Gate FinFET memories: high speed performances and improved reliability”. 23 IEEE Int Electron Dev Meet (IEDM 2007)

- S.Lombardo, C.Gerardi, L.Breuil, C.Jahan, L.Perniola, G.Cina, D.Corso, E.Tripiciano, V.Ancarani, G.lanacone, G.Iacono, C.Bongiorno, J.Razafindramora, *C.Garozzo*, P.Barbera, E.Nowak, R.Puglisi, G.A.Costa, C.Coccorese, M. Vecchio, E.Rimini, J.Van Houdt, B.De Salvo, M. Melanotte: “Advantages of the FinFET architecture in SONOS and Nanocrystal memory devices”

- C. Gerardi, E. Tripiciano, G. Cinà, S. Lombardo, *C. Garozzo*, D. Corso, G. Betrò, C. Pace, F. Crupi, “Multiple gate NVM cells with improved Fowler-Nordheim tunneling program and erase performances”, Solid-State Electronics, vol. 54, pp. 1319-1325, 2010

- *C. Garozzo*, R. A. Puglisi, C. Bongiorno, S. Scalese, E. Rimini, S. Lombardo. “SELECTIVE DIFFUSION OF GOLD NANODOTS ON NANO-PATTERNED SUBSTATES REALISED BY DIBLOCK COPOLYMERS SELF-ASSEMBLING”. C. To be published on Journal of Materials Research (JMR), Focus Issue on Self-Assembly and Directed Assembly of Advanced Materials(2010).

- *C. Garozzo,* R.A. Puglisi, C. Bongiorno, C. Spinella, S. Mirabella, R. Reitano, E. Rimini, A. Grasso, S. Di Marco, M. Foti, S. Ravesi, S. Lombardo.HYDROGEN ROLE IN THE PHASE TRANSITION FROM AMORPHOUS TO NANOCRYSTALLINE SILICON FILMS. *to be submitted.*

- G. Cannella, F. Principato, M. Foti, *C. Garozzo,* S. Lombardo. “Capacitance study of thin film SnO2:F/p-type a-Si:H heterojunctions” Energy Procedia. *In press*

- G. Cannella, , F. Principato, M. Foti, *C. Garozzo*, S. Di Marco, A. Grasso, S. Lombardo: “Characterization of the SnO2 :F / p-type a-Si:H / Mo structures for thin-film a-Si:H solar cell applications”, *to be submitted.*

Acknowledgements

Il periodo del dottorato è stato davvero importante per la mia vita, ritengo una fortuna in questo periodo storico riuscire a fare ricerca per tre anni. Quando finalmente è ora di "consegnare" il tuo lavoro ti vengono in mette tutte le persone a cui devi dire "grazie" e senza le quali non saresti riuscita a finire questo percorso. In questi tre anni mi sono state a fianco tantissime persone che vorrei ringraziare nel giusto modo, per questo uso l'italiano. Per prima cosa vorrei ringraziare il mio Tutor di dottorato, il professore Rimini, grazie di cuore per avermi seguito in questi tre anni. Inoltre vorrei ringraziare la Dott.ssa Rosaria Puglisi per avermi insegnato tanto, sia nel modo di fare ricerca sia nel modo di esporre le mie idee, grazie anche per la pazienza e per la continua rilettura della tesi. Desidero ringraziare anche il dott. Lombardo per avermi seguito a partire dalla tesi di laurea e per l'aiuto in questi tre anni, grazie per i consigli e i suggerimenti. Grazie anche per la pazienza degli ultimi periodi ad entrambi. Volevo inoltre ringraziare il professore Licciardello per l'ottima organizzazione del dottorato e per avermi dato la possibilità di andare a due ottime summer school.

Menzione a parte merita Corrado Bongiorno, per avermi supportato e sopportato in questi tre anni, per avermi dato consigli sulla vita, la ricerca e i migliori film da vedere. Grazie Corrado sei addirittura riuscito ad aumentare la mia curiosità, e a indirizzarla verso la sfera scientifica!

Vorrei ringraziare il direttore del CNR-IMM Corrado Spinella per avermi permesso di lavorare nei suoi laboratori e per l'aiuto fornitomi per l'interpretazione dei dati RDF. Vorrei ringraziare inoltre altre persone che hanno reso possibile questo lavoro di tesi. Il gruppo R&D dell' ST Microelectronics ed in particolare S. Ravesi, S. Di Marco, A.Grasso e S. Coffa, per la realizzazione dei layer di a-Si:H e nc-Si:H, e dei diodi pin. Inoltre vorrei ringraziare Marina Foti dell' ST Microelectronics per avermi fornito le misure elettriche dei pin, e per essere la migliore compagna di stanza di sempre!!! Vorrei ringraziare Domenico corso per l'aiuto nelle misure elettriche, e Salvo Di Franco per l'aiuto in clean room, dimenticavo scusa per l'insistenza!!! Un ringraziamento anche alla Dott.ssa S.Scalese per le analisi SEM. Un grazie va anche al dott. S. Mirabella del MATIS per avermi fornito le misure

ERDA, inoltre anche al Prof. Reitano per la disponibilità e la gentilezza mostrata nell'aiuto con l'analisi dei dati FTIR. Grazie a S. Pannitteri per la pazienza e per aver inventato i "migliori" metodi di preparazione campioni, oltre ad avermi fatto ridere a crepapelle a pranzo. Grazie anche a G. Cannella per la disponibilità e i dati della simulazione.

Grazie anche a tutti i ragazzi del CNR, in particolare a Rosa e Gabriella per i nostri divertenti viaggi di ritorno e per essere diventate delle mie ottime amiche, ma grazie anche ad Alessia, Peppe, Carmelo e Roberto, ragazzi in bocca al lupo per il vostro dottorato.

Un grazie speciale anche a Salvo Bagiante, per avermi aiutato con il LyX e per l'aiuto in tutta la mia carriera universitaria, Salvo è finalmente finita, ora non abbiamo più materie, tesi e tesine varie da consegnare!!!!

Un enorme grazie va ai miei genitori che mi sostengono da tutta la vita, grazie per essermi stati sempre vicino incoraggiandomi in ogni mia scelta. Sandro, grazie per essere il mio amore e il migliore amico, grazie dell'incoraggiamento e dello straordinario "supporto psicologico", è ufficiale da oggi non ti stresserò più con la frase: devo finire la tesi!

E' stato un periodo intenso e a volte difficile, ma come direbbe Ed Bloom (Big Fish): *Tanto più una cosa è difficile tanto più grande è il premio finale.* ....Grazie a tutti